

Diss. ETH No. 13250

# Rotational Aspects of Atmospheric Flow past Alpine-scale Orography

A dissertation submitted to the  
SWISS FEDERAL INSTITUTE OF TECHNOLOGY (ETH)  
ZÜRICH

for the degree of  
DOCTOR OF NATURAL SCIENCES

presented by  
MICHAEL SPRENGER  
Dipl. Phys. ETH  
born 16 April 1970  
citizen of Triesen, Liechtenstein

accepted on the recommendation of  
Prof. Dr. C. Schär, ETH Zürich, co-examiner  
Prof. Dr. H. C. Davies, ETH Zürich, co-examiner  
Dr. G. Mayr, University of Innsbruck, co-examiner

1999



# Contents

Abstract	V
Zusammenfassung	VII

## PART A

<b>1</b>	<b>Introduction</b>	<b>3</b>
<b>2</b>	<b>Underlying Theoretical Concepts</b>	<b>4</b>
	2.1 Gravity Waves, Wave Breaking and Pressure Drag	4
	2.2 Flow Splitting and Blocking	10
	2.3 Downslope Windstorms	14
	2.4 Gap Winds	18
	2.5 Vortex Streets and Wakes	19
<b>3</b>	<b>Contents of the Papers</b>	<b>22</b>

## PART B

### *Rotational Aspects of Stratified Gap Flows and Shallow Foehn*

	<b>Summary</b>	<b>27</b>
<b>1</b>	<b>Introduction</b>	<b>28</b>
<b>2</b>	<b>Definition of model problem</b>	<b>32</b>
<b>3</b>	<b>Linear regime</b>	<b>34</b>
<b>4</b>	<b>Nonlinear regime</b>	<b>36</b>
<b>5</b>	<b>Sensitivity experiments</b>	<b>37</b>
	5.1 Sensitivity to the topography's shape and size	38
	5.2 Sensitivity to upstream flow speed	40
<b>6</b>	<b>Multiple flow solutions for <math>f=0</math></b>	<b>41</b>
	6.1 Sensitivity of standard nonlinear solution for $f \rightarrow 0$	41
	6.2 Existence and stability of multiple solutions for $f = 0$	42
	6.3 Externally induced transitions between multiple flow solutions	44
<b>7</b>	<b>More realistic foehn-like settings</b>	<b>45</b>
	7.1 Impact of deep valleys leading up to the gap-like pass	45
	7.2 Impact of surface friction	46
	7.3 Impact of an inversion	49
<b>8</b>	<b>Concluding remarks</b>	<b>51</b>

## PART C

### *Linearized Flow over Isolated Orography: The Influence of Rotation*

	<b>Summary</b>	<b>55</b>
<b>1</b>	<b>Introduction</b>	<b>56</b>

<b>2</b>	<b>Problem Description, Linear Theory and Numerical Model</b>	<b>57</b>
2.1	Problem Description	57
2.2	Linear Theory	58
2.3	Nonlinear Simulations	59
<b>3</b>	<b>Axisymmetric Mountain</b>	<b>60</b>
3.1	Upstream Stagnation	61
3.2	Downstream Stagnation	63
3.3	Upper-level Flow Reversal and Wave Breaking	65
3.4	Intersection of Isentropes with Lower Boundary	66
<b>4</b>	<b>Elliptical Mountains</b>	<b>67</b>
4.1	Upstream Stagnation	68
4.2	Downstream Stagnation	70
4.3	Upstream Flow Reversal and Wave Breaking	71
4.4	Intersection of Isentropes with Lower Boundary	71
4.5	Angle of Attack	72
<b>5</b>	<b>Conclusions and Further Remarks</b>	<b>74</b>

## PART D

### *The Modification of a Front by the Alps: A Case Study Using the ALPEX Reanalysis Data Set*

	<b>Summary</b>	<b>79</b>
<b>1</b>	<b>Introduction</b>	<b>80</b>
<b>2</b>	<b>Numerical Model, and Initial and Lateral Boundary Conditions</b>	<b>82</b>
2.1	Modelling System	82
2.2	The ALPEX-IIIb Analysis from DWD	84
<b>3</b>	<b>Comparison of ALPEX versus ECMWF reanalysis</b>	<b>85</b>
<b>4</b>	<b>Synoptic and Mesoscale Weather Development</b>	<b>86</b>
4.1	Approaching Cold Front and Flow Splitting	86
4.2	Cold-Air Outbreak and Mistral	89
4.3	North Foehn	89
4.4	Cyclogenesis in the Lee of the Alps	92
4.5	Anticyclone and Bora	94
<b>5</b>	<b>Sensitivity Study</b>	<b>95</b>
5.1	Effects of Orographic Height	95
5.2	Effects of Surface Friction	96
5.3	Effects of Diabatic Processes	97
<b>6</b>	<b>Conclusions and Outlook</b>	<b>98</b>

## PART E

	References	103
	Curriculum Vitae	111
	Acknowledgments / Dank	113

## Abstract

Mountains exert a pronounced influence on weather and climate. At the heart of the underlying processes is the orographically induced dynamical modification of atmospheric flow past topography. The present thesis focus on a particular theme in this context, namely on *three-dimensional* aspects of stratified rotating flows past topography, with particular consideration of the influence of the Earth's rotation.

In a first part shallow foehn flows in the Alps are studied. They are often affected by gap-like features in elongated ridge-like topography. To assess the dynamics of these flows, idealized numerical experiments are conducted. The topography is taken to be a two-dimensional ridge oriented in the west/east direction with a valley transect across it and the upstream flow is assigned a westerly direction, constant wind speed, and constant Brunt-Väisälä frequency. It is shown that southerly across gap winds are possible and that the dynamics of this flow problem includes many linear and nonlinear phenomena, such as flow splitting, flow separation, hydraulic jumps, hydrostatic gravity waves and vertically trapped surface waves. Most interesting is the existence of multiple stationary solutions for the nonrotating case (two with northerly and southerly flow across the gap, respectively, and one with north/south symmetry). The relationship of the idealized setting to Alpine shallow Foehn is discussed, and additional experiments are conducted to assess the effects of surface friction and of an inversion present to the south of the ridge.

The second part considers the atmospheric flow past idealized isolated mountains on an  $f$ -plane in the framework of linear theory. The mountain shape is described by its horizontal extensions in streamwise and spanwise directions and by its height, the upstream flow is assumed to be of uniform velocity and uniform stratification. The critical mountain heights for near-surface stagnation on the windward side and in the lee of the mountain, for stagnation aloft and for intersection of streamlines with the lower boundary are determined. This results in a regime diagram which separates the regions where linear theory applies from the regions where nonlinear phenomena certainly dominate the flow. The curves separating the different regimes show a complex behaviour with respect to the horizontal extensions and the shape of the mountain, as well as to the angle of attack of the impinging flow. The most restrictive phenomenon for the applicability of the linear theory is the intersection of the streamlines with the ground. With the exception of the quasigeostrophic limit, the dimensionless critical mountain heights remain smaller than 1. Some nonlinear simulations are conducted to examine the validity of the estimates of the linear theory.

Finally, a real-case numerical simulation of the interaction of a cold front with the Alps is conducted, where the ALPEX-IIIb reanalysis data set of the German Weather Service (DWD) is used as initial and lateral boundary fields. After showing the superiority of this reanalysis data set over the corresponding ECMWF reanalysis data set for the studied case, the temporal development of the Mediterranean weather is discussed. This development includes flow splitting to the north of the Alps, a cold-air outbreak and Mistral between the Alps and the Pyrenees, lee cyclogenesis in the Gulf of Genoa, north Foehn and Bora. Special focus is given to the low-level tropospheric flow, which is studied by means of trajectory calculations, timeseries analysis and within the framework of potential vorticity (PV). Elongated banners of PV are observed south of the Gotthard pass during the north foehn. Furthermore, a PV anomaly at the western edge of the Alps separates and finally matures into a

lee cyclone. In a sensitivity study it is, finally, examined why the flow does not separate from the topography at the eastern edge of the Alps. It is shown that neither increased orography, nor increased surface friction, nor the neglect of all moisture processes considerably enhances the tendency for separation.

## Zusammenfassung

Gebirge beeinflussen das Wetter und Klima massgeblich. Verantwortlich hierfür ist deren Einfluss auf die Bewegung der Luftmassen. Die vorliegende Arbeit diskutiert einen Teilbereich dieser Dynamik. Es wird die geschichtete Strömung über Gebirge betrachtet, wobei insbesondere auf Einflüsse der dreidimensionalen Struktur der Gebirge und der Erdrotation eingegangen wird.

Der erste Teil der Arbeit hat seichte Föhnströmungen im Alpenraum zum Inhalt. Oft werden die Föhnwinde massgeblich durch die Anwesenheit von tiefen Einschnitten in Bergrücken mitbestimmt. Die Dynamik solcher Strömungen soll mittels stark idealisierter numerischer Simulationen betrachtet werden. Dazu wird die Topographie als ein Bergrücken angenommen, der in West/Ost-Richtung orientiert ist, und durch den ein in Nord/Süd-Richtung orientierter Einschnitt verläuft. Die Strömung sei weit stromaufwärts vom Einschnitt entlang dem Rücken mit konstanter Geschwindigkeit und mit höhenunabhängiger Schichtung. Die numerischen Simulationen zeigen, dass unter dieser Strömungssituation südliche Winde durch den Einschnitt auftreten können, und dass sie mit vielen dynamischen Besonderheiten ausgezeichnet sind. Lineare und nichtlineare Phänomene treten auf: Aufspaltung von Stromlinien, Ablösen der Strömung von der Topographie, hydraulische Sprünge, hydrostatische Schwerewellen und Oberflächenwellen. Von ganz besonderem Interesse ist die Tatsache, dass das geschilderte Strömungsproblem mehrere voneinander verschiedene Strömungsantworten zulässt, wenn man die Erdrotation ausschaltet. Neben einem symmetrischen Zustand, gibt es zwei weitere asymmetrische, wobei der eine einen Südwind, der andere einen Nordwind durch den Einschnitt aufweist. Schlussendlich wird auch die Beziehung des idealisierten Problems zum seichten Südföhn in den Alpen diskutiert. Dazu werden realistischere Prozesse, wie Bodenreibung und Inversionen, betrachtet.

Im zweiten Teil wird wiederum ein stark idealisiertes Problem untersucht, nämlich die linearisierte Anströmung auf einen isolierten Berg. Dabei wird zudem die f-Ebenen Approximation gemacht. Der Berg selbst wird durch drei Parameter beschrieben: durch seine horizontalen Ausdehnungen in Strömungsrichtung und senkrecht dazu und durch seine Höhe. Die Anströmung ist wiederum mit konstanter Geschwindigkeit und mit konstanter Schichtung. Mehrere Prozesse werden untersucht: Stagnation der Strömung auf der Oberfläche im Luv und im Lee des Berges, Stagnation in der freien Atmosphäre über dem Berg und das Eintauchen der Stromlinien in den Boden. Für all diese Prozesse liefert die lineare Theorie kritische Gebirgshöhen, oberhalb derer die Prozesse auftreten. Insgesamt resultiert damit ein Regimediagramm, das die Bereiche, in denen die lineare Theorie gültig ist, von den Bereichen abtrennt, in denen sich die Strömung massgeblich nichtlinear verhält. Die kritischen Gebirgshöhen in diesem Diagramm, die die einzelnen Prozesse abgrenzen, zeigen hierbei eine komplizierte Abhängigkeit von der horizontalen Ausdehnung des Gebirges, von dessen Form und auch von der Anströmungsrichtung. Insgesamt beschränkt das Eintauchen der Isentropen in den Boden die Anwendbarkeit der linearen Theorie am meisten. Mit Ausnahme des quasigeostrophischen Falles überschreiten die dazugehörigen kritischen dimensionlosen Gebirgshöhen den Wert 1 nicht. Um diese Resultate der linearen Theorie mit der Wirklichkeit zu vergleichen, werden ebenfalls einige nichtlineare numerische Simulationen durchgeführt.

Schlussendlich wird im dritten Teil ein realer Fall diskutiert, bei dem sich eine Kaltfront auf die Alpen zubewegt und modifiziert wird. Dazu werden numerische Simula-

tionen durchgeführt. Die benötigten Anfangs- und seitlichen Randfelder entstammen der ALPEX-IIIb Reanalyse des Deutschen Wetterdienstes (DWD). Diese Reanalyse erweist sich für den betrachteten Fall den entsprechenden ECMWF Reanalysen überlegen. Die Wechselwirkung der Front mit den Alpen führt zu vielen atmosphärendynamische Phänomene: eine Aufspaltung der Strömung im Norden der Alpen, ein Kaltluftausbruch zwischen den Alpen und den Pyrenäen, Mistral, Lee-Zyklogenese im Golf von Genua, Nordföhn und Bora. Besonderes Gewicht wird bei der Auswertung auf Strömungsphänomene in der unteren Troposphäre gelegt. Dazu werden Trajektorienrechnungen und Zeitreihen betrachtet. Ausserdem wird die Strömung im Hinblick auf die potentielle Wirbelstärke (PV) untersucht. Es zeigt sich unter anderem, dass lange PV Bänder südlich des Gotthard Pass' während Nordföhn auftreten. Zudem löst sich eine weitere PV-Anomalie vom Westrand der Alpen und entwickelt sich schlussendlich in eine Lee-Zyklone.



# PART A



## 1 Introduction

The Earth's surface is covered by numerous mountain chains. The Alps, the Rocky Mountains, the Himalaya, the Skandinavien Alps, the New Zealand Alps, just to name some of them. It is well known that they strongly influence atmospheric dynamics (for a concise review see e.g. Smith 1979b, Smith 1989a, Durran 1990). This is not astounding since the Alps, for instance, reach a crest height of approximately  $3000m$ , while the typical height of the midlatitude tropopause is  $12km$ . Therefore, the air masses impinging on the Alps from any direction either move around this obstacle sideways or are lifted over it, resulting in large vertical displacement. Such vertical displacement might then lead to a considerable qualitative change of the overall flow pattern, inducing the condensation of ambient water vapour, the release of latent heat, deep convection and precipitation. This is just one possible scenario of the extremely manifold and complicated interaction of the atmosphere with the Alps.

Precipitation climatologies of the European Alpine region reveal the importance of such scenarios. Frei and Schär (1998) present a precipitation climatology which exhibits a horizontal resolution of about  $25km$ . Their analysis shows that the most prominent Alpine effects include the enhancement of precipitation along the Alpine foothills, and the shielding of the inner-Alpine valleys. Furthermore, a simple precipitation-height relationship does not exist on the Alpine scale, because much of the topographic effect is associated with slope and shielding rather than height effects. A better understanding of the processes leading to orographically induced precipitation is also essential for estimating regional effects of climate variations (IPCC 1990), as revealed by regional climate simulations (Frei et al. 1998 and Lüthi et al. 1996).

Since the current and future Alpine climate is strongly influenced by the orographically induced atmospheric flows (see e.g. Schär et al. 1998), such airflows have been in the focus of atmospheric research for a long time. Nevertheless, many open questions remain. Some of them are addressed in recent international atmospheric research programmes, such as the Mesoscale Alpine Programme MAP (Binder and Schär 1995) or the previous Alpine Experiment ALPEX (Kuettner 1980). Many of the questions relate to the processes leading to strong precipitation and the associated flooding events. The moist dynamics of such flows is intimately related to the nature of stratified airflows, and many of the associated dry processes are still poorly understood. Some of these are addressed in this thesis:

*How are small-scale topographic features related to local wind systems? The so-called shallow south Foehn, for instance, depends on the presence of north/south valley transects through the main Alpine ridge (mean height around  $3000m$ ), such as the Gotthard pass ( $2100m$ ) in the Swiss or the Brenner pass ( $1500m$ ) in the Austrian Alps. How is the southerly flow through these gaps decoupled from the westerly or even north-westerly flow above the Alpine crest during shallow south Foehn? Which processes lead to such strong gusty winds in the northern valleys connected to these pass regions?*

*When will the low-level air impinging on a mountain surmount it and when will it move sideways around it? If the flow is blocked upstream of the mountain and directed sideways around it, the vertical displacements of air parcels and the associated precipitation effects are considerably diminished. Many studies tried to shed light on*

*this issue, yet the influence of the Coriolis force or the planetary boundary layer are still poorly understood.*

*Where and when do gravity waves, which are forced by the atmospheric flow over a mountain, break? Or still more basic, how do they propagate vertically? The basic theory of gravity waves is well known. But as soon as the linear regime is left, challenging problems arise. The question of breaking is of great importance not only for atmospheric science, but also for air traffic, since breaking is a source of strong turbulence. Furthermore, the associated drag force represents a major player in determining the phase and amplitude of the planetary-scale waves and the climate zones on the northern hemisphere (see e.g. Broccoli and Manabe 1992).*

*What is the inherent dynamics of potential vorticity (PV) banners and what is their impact on the larger-scale flow? Idealized and real-case numerical simulations suggest that the flow of air past three dimensional topography is often accompanied by elongated PV filaments. The research on these filaments is just at its beginning. Therefore basic questions, such as their high-resolution structure or their stability or even their generating processes remain at least partly unanswered.*

To answer these and related questions, theoretical, numerical, laboratory and observational investigations are necessary. The present thesis tries to enlighten some of the atmospheric features from the viewpoint of idealized numerical and theoretical considerations. The motivation for idealized studies comes from the mere fact that it is impossible to simulate atmospheric flow in a “perfect” way, i.e. with all its features. Nonlinearity and the interaction on all temporal and spatial scales, as well as 3-dimensionality and non-stationarity make atmospheric dynamics extremely complicated, and interesting! Even if a perfect simulation of atmospheric dynamics were possible, it would be difficult to extract the relevant physical processes at work from this “mess” of intricate processes. Idealized studies, on the other hand, are exceptionally well suited to obtain physical insight into the relevant processes at work. These models have to be complicated enough, in order to capture all the phenomena of interest, but simple enough to allow a clear insight into the underlying physical processes.

## 2 Review of Underlying Theoretical Concepts

In this subsection simplified conceptual and theoretical, as well as important meteorological phenomena are presented. We discuss (1) gravity waves, (2) flow splitting and blocking, (3) downslope windstorms, (4) gap winds, and (5) vortex streets and wakes. Special emphasis is given to the influence of rotation.

### 2.1 Gravity Waves, Wave Breaking and Pressure Drag

The dynamics of atmospheric motions is governed by a highly nonlinear set of equations, the derivation of which from first principles can be found in many introductory text books on atmospheric dynamics (Holton 1992, Gill 1982, Pichler 1997) and on geophysical fluid dynamics (Pedlosky 1987). In many cases this nonlinear set can be considerably simplified. Often the flow can be assumed to be steady, incompressible,

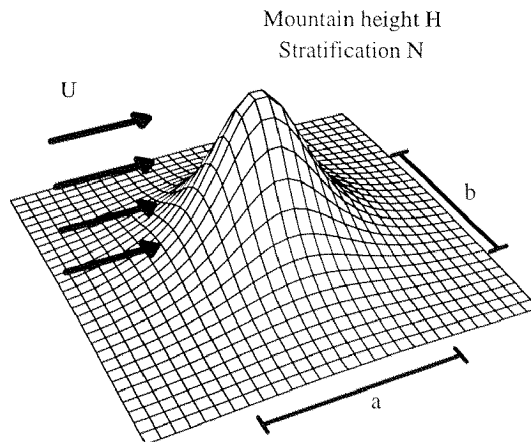


Figure 1. Idealized flow problem: isolated orography of height  $H$  and horizontal half-widths  $a$  and  $b$ , uniform upstream flow with velocity  $U$  and stratification  $N$ .

dry, inviscid and adiabatic (see e.g. Pedlosky 1987). Furthermore, often the flow can be linearized, i.e. decomposed into two parts: a basic state flow and a small deviation from this state. As an example assume that the basic state flow is characterized by uniform velocity  $\vec{v}_0 = (U, 0, 0)$  and a uniform vertical stratification as expressed by the squared Brunt Väisällä frequency  $N^2 = g/\bar{\Theta} \cdot \partial\Theta_0/\partial z$ , where  $\bar{\Theta}$  denotes a constant background potential temperature (Fig.1). Furthermore, we assume that the basic state flow is in geostrophic balance, such that the zonal wind velocity  $U$  is related to the basic state pressure  $p_0$  by

$$f \cdot U = -\frac{1}{\rho} \cdot \frac{\partial p_0}{\partial y} \quad (1)$$

where  $f$  denotes the Coriolis parameter. Within the Boussinesq framework the density in the horizontal equations of motions is taken to be constant at value  $\rho_0$ . In the vertical momentum equation density fluctuations are allowed in order to include buoyancy forces. The linearized set of equations for the wind  $(u', v', w')$ , pressure  $p'$  and buoyancy  $b'$  perturbations then becomes, with the advection operator  $L = \partial/\partial t + U \cdot \partial/\partial x$ :

$$\begin{aligned} L(u') - f \cdot v' &= -(p'/\rho_0)_x \\ L(v') + f \cdot u' &= -(p'/\rho_0)_y \\ L(w') &= -(p'/\rho_0)_z + b' \quad \text{with buoyancy} \quad b' = g \cdot \Theta'/\Theta_0 \\ u'_x + v'_y + w'_z &= 0 \\ L(b') + N^2 \cdot w' &= 0 \end{aligned} \quad (2)$$

This set of equations contains waves, so-called internal gravity waves. A detailed description of gravity waves can be found in many basic texts (see e.g. Pichler 1997). Gill (1982) devotes a whole chapter to gravity waves in a *rotating* fluid. Therefore, we do not present a detailed discussion here. Some main results might nevertheless be appropriate. The following discussion follows Lüthi (1994). If a Fourier decomposition

according to

$$\Phi' = \Phi^* \cdot \exp\{i \cdot (kx + ly + nz)\} \quad (3)$$

with  $\Phi'$  denoting any of the perturbation quantities ( $u'$ ,  $v'$ ,  $w'$ ,  $p'$ ,  $b'$ ) is assumed, it can be shown that – at steady state  $\partial/\partial t = 0$  – the vertical wave number  $n$  can be expressed by the horizontal wave numbers  $k, l$ :

$$n^2 = n^2(k, l) = \left(\frac{N}{f}\right)^2 \cdot \frac{1 - S^2}{Ro^2 - 1} \cdot K^2 \quad K^2 = k^2 + l^2 \quad (4)$$

Here,  $Ro = U \cdot k/f$  is a measure for rotational effects and  $S = U \cdot k/N = f/N \cdot Ro$  is a measure for non-hydrostatic effects. The most important fact which can be inferred from this equation is that waves can propagate vertically only if the zonal wavenumber  $k$  satisfies  $f/U < k < N/U$ . This defines the wave region. For  $k > N/U$  or  $k < f/U$ ,  $n^2$  is negative and the disturbances decay vertically.

One important source for gravity waves are mountains. If air flows over a periodic mountainous landscape of the form

$$\eta(x, y) = H \cdot \exp\{i \cdot (kx + ly)\} \quad (5)$$

internal gravity waves which satisfy the previous dispersion relation  $n = n(k, l)$  are excited. Thereby the amplitude  $\Phi^*$  and thus the whole solution is completely determined by the lower boundary condition.

The solution for an *isolated* mountain can be obtained from a superposition of the above solutions for periodic mountainous landscapes. If the mountain is decomposed into its Fourier components according to

$$\eta(x, y) = \int \eta(k, l) \cdot \exp[i \cdot (kx + ly)] dk dl \quad (6)$$

the solutions for the topographic components  $\eta(k, l) \cdot \exp[i \cdot (kx + ly)]$  under the integral are determined in the same manner. Hence, due to the linearity of the model, one can sum (integrate) over all these partial solutions to obtain the solution for the isolated mountain.

For a mountain ridge of along-flow half-width  $L$ , the predominant contribution to the complete flow solution will come from the terms with  $k \approx 2\pi/L$  since these components will have the largest Fourier amplitudes  $\eta(k, l)$ . Hence, if  $U/Lf \ll 1$  ( $U/LN \gg 1$ ) the  $k$ 's with  $Ro = Uk/f \ll 1$  ( $S = Uk/N \gg 1$ ) are important and the flow perturbations decay with height. On the other hand, if  $1 \ll U/Lf \ll N/f$  the  $k$ 's in the wave region prevail and vertically propagating gravity waves occur. Therefore, an overall Rossby number

$$Ro = U/Lf \quad (7)$$

is attributed to a mountain with half-width  $L$ , allowing a rough estimate of the flow characteristics. This Rossby number is an important dimensionless parameter which measures the overall influence of the Coriolis force. It can be interpreted as the ratio of two time scales:  $L/U$  defining the advective time scale, and  $1/f$  the Coriolis time scale.

If waves emanate from the mountain, energy is radiated away. The direction of the energy propagation depends on the value of  $k$ . The diagram taken from Gill (1982)

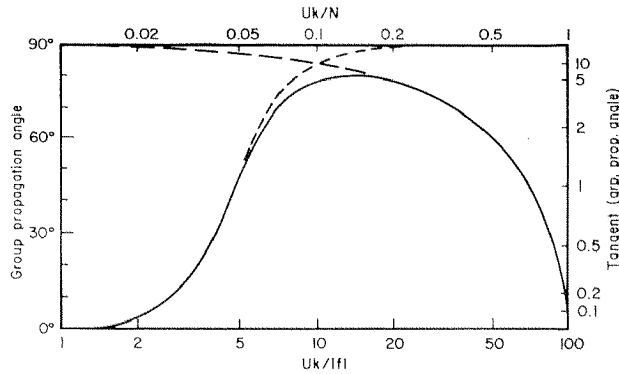


Figure 2. Angle made with the horizontal by the group velocity relative to the ground, shown (solid line) as a function of the horizontal wavenumber  $k$  of the topography for the case  $N/f = 100$ . If earth rotation is ignored ( $f = 0$ ), the curve is modified at low wavenumbers to the one shown by large dashes. If the hydrostatic approximation is made, the curve is modified at high wavenumbers to the one shown by small dashes. If rotation is ignored *and* the hydrostatic approximation is made, the angle is  $90^\circ$  for all  $k$  (from Gill 1982).

shows the details for a two-dimensional ridge (Fig.2). For  $k \rightarrow f/U$  and  $k \rightarrow N/U$  the energy propagation is horizontal, whereas in between it becomes nearly vertical (about  $80^\circ$  for  $N/f = 100$ ). If rotation is neglected (i.e. if the Coriolis parameter  $f$  is set to 0), the angle becomes  $90^\circ$  for small wave numbers  $k$ . If the hydrostatic approximation is made, the angle becomes  $90^\circ$  as  $k$  becomes large. If both approximations are made, the non-rotating and hydrostatic limit, the angle is  $90^\circ$  for *all* values of  $k$ . Following the discussion above, we associate  $k$  in the above discussion with the half-width  $L$  of a two-dimensional ridge by means of the relation  $k = 2\pi/L$ . Therefore, depending on the half-width  $L$  of a mountain, the energy emanates either horizontally, vertically or at an intermediate angle. Trüb and Davies (1994) investigated this issue in dimensionless notation. Instead of describing the width of the mountain by its half-width  $L$ , they chose the Rossby number  $Ro = U/Lf$ . In the same way as the mountain with half-width  $L$  is characterized by a spectral band of width  $\Delta k$  around  $k = 2\pi/L$ , the mountain described by  $Ro = U/Lf$  is characterised by a spectral band of width  $\Delta Ro$  around  $Ro$ . They stressed that two criteria are necessary for a strong atmospheric response: both the amplitudes of the dominant modes near  $Ro$  and their coherence across the band  $[Ro - \Delta Ro, Ro + \Delta Ro]$  have to be large. Quasi-inertial horizontally-propagating wave packets ( $Ro \rightarrow 1$ ), for instance, are linked with large amplitude, rapid amplitude decrease across the band and weak coherence. On the other hand, for a wave packet of essentially vertically propagating, hydrostatic buoyancy modes ( $Ro \approx 10$ ), the waves are of almost uniform amplitude and high coherence. Furthermore, for a broader ridge of the same height the orographic forcing of these latter modes is reduced. Changes from  $Ro \approx 10$  to  $Ro \approx 1$ , for instance, are associated with an order of magnitude weaker waves.

In the previous discussion vertically uniform upstream conditions with respect to the velocity and the stratification were assumed. Of course, these assumptions are too restrictive for real-case applications. A short review on the effects of flow variation with height can be found in the book of Gill (1982). For suitably inhomogeneous upstream profiles, waves with certain values of  $k$  can be reflected downward and thus reinforce or weaken the disturbance in the lower atmosphere, depending on the phase coherence, or they might be absorbed at critical levels. Assume for instance, that the

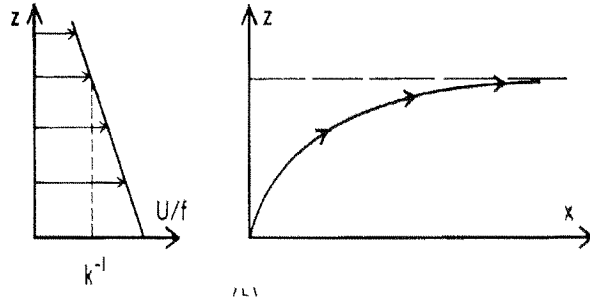


Figure 3. Special type of ray path for a medium whose properties vary slowly with vertical coordinate  $z$ . The paths are those that would be followed by a hypothetical particle travelling at the local group velocity  $\vec{c}_g$ , this being calculated as a function of  $U$  and  $N$ , using the formula for a uniform medium. The horizontal component  $k$  of the wavenumber and frequency  $\omega$  are fixed for each ray. The shown case exhibits absorption. This occurs for hydrostatic waves with wavenumbers such that rotation effects are important when  $U$  decreases with height and drops to a value equal to  $|f|/k$ . Upward-propagating waves approach this level asymptotically. The vertical component of the wavenumber continually decreases, so friction effects cause the wave to dissipate (taken from Gill 1982).

velocity  $U(z)$  decreases with height (Fig.3). A hydrostatic gravity wave packet with mean wave number  $k$  that satisfies  $U(0)k/f \gg 1$  near the ground, will propagate nearly vertically, as discussed before. But if  $U$  decreases with height, the direction of propagation becomes more and more horizontal, until it becomes strictly horizontal at the level  $z$  where  $U(z)k/f = 1$ . In this case the wave is absorbed at this level. Other effects of varying properties with height include partial absorptions and reflections and resonance effects (see e.g. Gill 1982).

The direction of energy transport is of great theoretical and practical interest, since gravity waves are able to “communicate” the presence of the mountain to far-away regions. Especially the very steep propagating waves can reach as far up as to the stratosphere, where they recently even were associated with increased stratospheric ozone depletion (Carslaw et al. 1998). They decrease the local temperature which is important for the ozone-depleting heterogenous chemical processes in polar stratospheric clouds. From a dynamical perspective the momentum transport by gravity waves is more important. The upward propagation of energy by gravity waves is associated with a downward flux of momentum (Bretherton 1969). The Eliassen-Palm theorem (Eliassen and Palm 1961) states that the Reynolds stress for each Fourier component, which in a nonrotating system measures the momentum flux, is independent of height, as long as no critical layers or dissipation occurs. The gravity wave amplitude can intensify as they propagate to heights with lower density. This amplification finally leads to strong amplitudes that result in unstable stratification or dynamical instability, which in turn induce “wave breaking”. The regions where this occurs are characterized by strong turbulence and act as a sink for the vertical momentum flux. Palmer et al. (1986) showed that neglecting this process leads to a systematic westerly bias in a general circulation model. In subsequent studies gravity wave propagation schemes were developed, among them those of Bacmeister (1993) and Bacmeister et al. (1994) who used automatic algorithms to search mountain ridges which might be strong sources of gravity waves.

Smith (1989) studied the uniform hydrostatic nonrotating flow imping on an isolated mountain, and deduced the critical mountain height above which wave breaking oc-



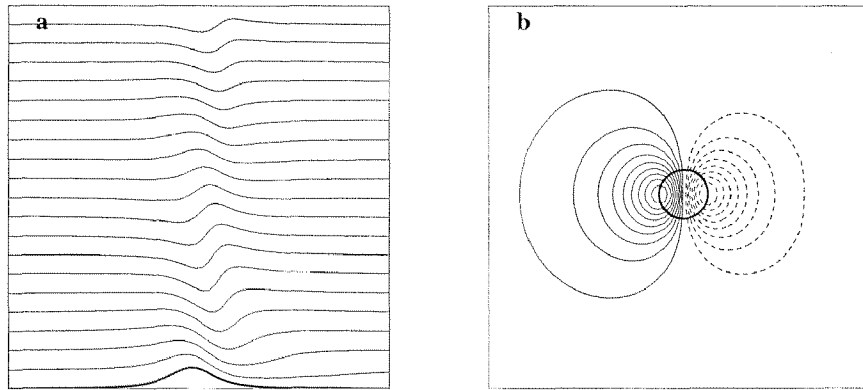


Figure 4. Schematic linear results for the flow problem depicted in Fig.1. (a) Streamlines in an along-flow vertical section through the mountain illustrating the upstream/downstream asymmetry if gravity waves emanate from the mountain. (b) Perturbation pressure field at the surface with a high pressure anomaly (solid lines) on the windward side and a low pressure anomaly on the lee (dashed lines).

curs. His findings, which rely on *linear* theory, indicate that ridge like mountains favour wave breaking, whereas narrow elongated mountains are much less susceptible to wave breaking (see later in Fig.7) This can, at least partly, be understood by the reduced meridional dispersion of “wave energy” for ridge-like mountains. Olafsson and Bougeault (1996) extended the studies by Smith to the nonlinear regime. The major finding of their study concerns wave breaking. Smith (1989a) suggested that gravity wave breaking will no longer occur if the mountain height surpasses a critical value. But Olafsson and Bougeault found wave breaking even for large values of dimensionless mountain height  $NH/U$ , although the breaking does no longer occur on the axis of symmetry, but is limited to narrow regions on either side of the mountain.

The drag exerted by vertically propagating gravity waves is also evident near the surface. The vertical propagation of gravity waves is associated with an upstream/downstream asymmetry, with acceleration to the lee and deceleration on the windward side of the mountain (Fig.4). Associated with this asymmetry a non-vanishing pressure force acting on the mountain occurs, with a local high pressure anomaly on the windward side and correspondingly a local low pressure anomaly to the lee. The large pressure gradients prevailing over the Alps during strong Foehn periods can partly be attributed to the existence of gravity waves. In addition to the gravity-wave drag, a form drag contributes to the overall pressure drag acting on the mountain. Both contributions are related to an energy transport away from the terrain (Davies 1986). Whereas this transport is accomplished by the transmission of energy through the mean flow in a *coherent wave-like* form for the gravity-wave drag, it is accomplished by the advection of *turbulent* eddy energy within the mean flow for the form drag.

Studies on the drag during Foehn were conducted by Hoinka and Clark (1991). Their numerical simulations of the Foehn at 8 november 1982 yields that net force exerted on the atmosphere by the Alps is  $-4.72 \times 10^{11} N$  due to the surface pressure drag. The corresponding wave momentum flux at a height of  $3.5 km$  above mean sea level is  $-2.58 \times 10^{11} N$ , i.e. 50% of the net force. But – as they stress in their study – comparisons with observations indicate that this might be too large by a factor of about 6. Davies and Phillips (1985) used microbarograph measurements along the

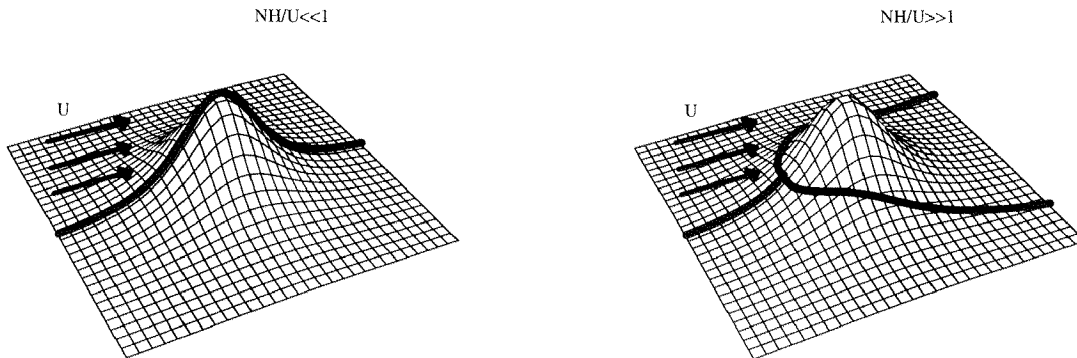


Figure 5. Trajectory of an upstream centerline air parcel for small dimensionless mountain height (left) and large dimensionless mountain height (right). In the latter case the flow splits on the upstream side of the mountain and moves sideways around it (redrawn after Smith 1989a).

St. Gotthard section of the Alps to estimate the variation of the pressure drag during the special observational period of the ALPEX project. They showed that the time-trace of the drag is directly related to the synoptic-scale weather development, but that it is also substantially influenced by mesoscale effects.

Smith (1979a) showed that the mountain wave flux due to gravity waves decreases with decreasing Rossby number  $Ro = U/af$ . For instance, the momentum fluxes reduce to about 60% of those to be expected in the nonrotating case for a ridge with half-width of  $100\text{km}$  and a impinging flow speed of  $20\text{m/s}$ . The influence of rotation and surface friction on orographic drag was further studied by Olafsson and Bougeault (1997). They compared the pressure drag acting on mountains of various heights and aspect ratios in flows characterised by uniform upstream velocity and stratification. For small dimensionless mountain heights their findings agree with linear theory, i.e. the pressure drag is reduced by the effect of rotation. But for larger dimensionless mountain heights,  $NH/U > \approx 1.4$ , the effect reverses, the pressure drag increases with the rotation rate. They propose as explanation that in the small-mountain limit the acceleration above the mountain is the dominant feature and this acceleration is diminished by the presence of rotation. Hence the pressure drag is reduced by the effect of rotation. On the other hand, for large mountain heights the upstream air becomes strongly slowed down and blocked. In this flow regime the Coriolis force additionally accelerates the low-level flow around the mountain, and thereby enforces an increase in the resulting pressure drag.

## 2.2 Flow Splitting and Blocking

From basic fluid dynamical arguments it can be expected that air parcels in stratified flows will move sideways around a mountain instead of over it if the mountain height surpasses a critical value (Fig.5). Laboratory experiments (Baines 1979, Hunt and Snyder 1980) suggest that the air will split on the windward side of the mountain and then move sideways around it, if the dimensionless mountain height  $NH/U$  surpasses the value 1 ( $N$  the Brunt-Väisällä frequency,  $H$  the dimensional mountain height and  $U$  the upstream velocity). Observational studies (see e.g. Binder et al. 1989, Chen and Smith 1987), as well as numerical real-case studies (Kljun 1999) provide clear

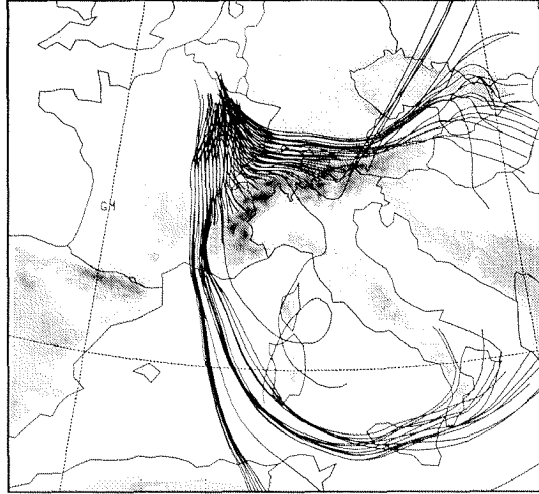


Figure 6. Simulation of trajectories starting in the north of the Alps at 870 to 850 hPa. The left part of the trajectories sinks after 6 hours of simulation down to 960 hPa and rises again over the Mediterranean to 670 hPa. The right part ends at 740 hPa on average.

evidence that flow splitting occurs (Fig.6).

But the physical mechanisms leading to flow splitting are still not completely clear. Smith used a linear model (1980, 1988, 1989a) to address this problem. His studies suggest that the transition from the flow over to the flow around regime cannot be purely understood by means of the simple energy argument of Sheppard (1956). He essentially assumed that the kinetic energy of a dense low-level air parcel has to be large enough in order to be raised over the potential energy barrier of the mountain. This argument leads to the above mentioned dimensionless critical mountain height  $NH/U = 1$ . But such a model makes obviously no distinction between different shapes of mountains. Furthermore, it assumes that the centerline air parcel is not influenced by the local pressure field which is also determined by nearby air parcels and motions. In his linear model Smith avoids these obvious deficiencies. Although the *linear* model cannot correctly predict the critical height for the highly *nonlinear* flow splitting either, it can nevertheless predict qualitative behaviour which is not included in the energy argument (Fig.7). A narrow ridge aligned with the flow, for instance, can lift a centerline air parcel to much greater heights than a ridge aligned perpendicular to the flow. Note also how the critical mountain heights for near-surface flow splitting and the free-atmosphere wave breaking intersect. Narrow elongated mountains favour flow splitting, whereas broad ridge-like mountains favour wave breaking. Since any of these two processes considerably modifies the *whole* flow solution, the predictions for the other process might be invalidated, as Smith indicates by dashing and dotting in his diagram.

Smith's diagram neglects the Earth's rotation. Scale analysis, on the other hand, demonstrates that rotation becomes important for mesoscale mountains, such as the Alps. In fact, Smith (1982) shows that even in the weakly rotating limit the flow changes considerably. By means of a perturbation expansion technique he deduced that the pressure, vertical velocity and hence vertical displacement fields remain unchanged in first order, but that the horizontal wind changes. The air parcels are deflected towards the left, when looking downstream. The predictions of the nonro-

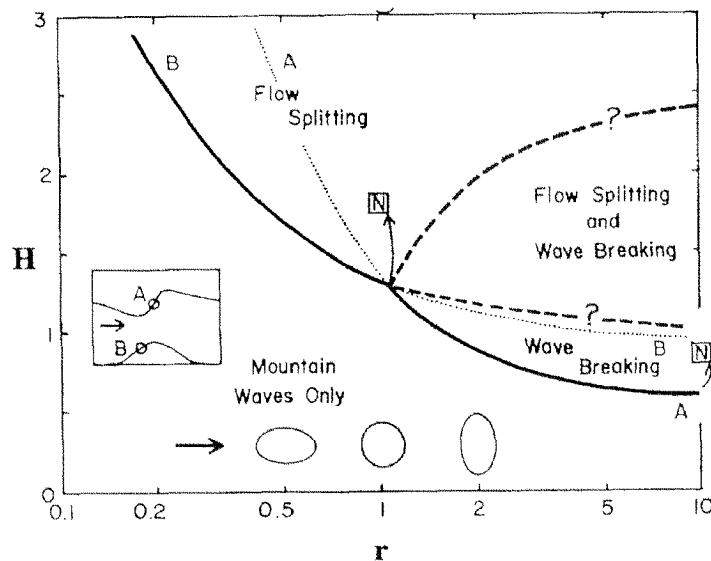


Figure 7. Regime diagram for hydrostatic flow over a mountain. The diagram axes describe the mountain shape  $r$  (horizontal aspect ratio) and size  $H$  (dimensionless mountain height). Solid curves: linear theory estimates of flow stagnation aloft (curve A) and at the windward slope (curve B). (from Smith 1989a)

tating linear model become completely unrealistic, if the Coriolis force dominates the inertial term in the equations of motion. In this quasigeostrophic limit, the stagnation of the flow sometimes corresponds to flow splitting and air moving around the mountain, and sometimes to Taylor cap like features, i.e. regions which are decoupled from the surrounding flow (Schär and Davies 1988). Peng et al. (1995) performed idealized numerical simulations to assess the importance of the Coriolis force on three-dimensional flow past a mountain. They showed that for high mountains, for which the flow is strongly deflected sideways due to blocking, the Coriolis effect cannot be neglected even though the associated Rossby number is large. Even for mountains which have only a half-width of about  $25\text{km}$ , the flow becomes asymmetrical, with stronger deflection towards the left (when looking downstream).

Trüb (1993) determined a regime diagram for flow over and flow around a circular mountain if *rotation is taken into account*. This study used an isentropic model and showed that the critical mountain height *decreases* with *increasing* Rossby number (Fig.8).

The blocking of air on the windward side of the mountain is directly related to flow splitting, since splitting implies the presence of a stagnation point. From Sheppard's (1956) energy argument, the same estimate  $NH/U > \approx 1$  for upstream blocking can be derived, with the same limitations. Approaches towards a better understanding of blocking for two-dimensional geometry were undertaken, the most important ones being theoretical studies based on linear theory and hydraulic analogs. Although upstream blocking is an inherently nonlinear phenomenon, some important insights were gained by application of linear theory. Pierrehumbert (1984) showed that the deceleration of the flow upstream of a mountain depends not only on the dimensionless

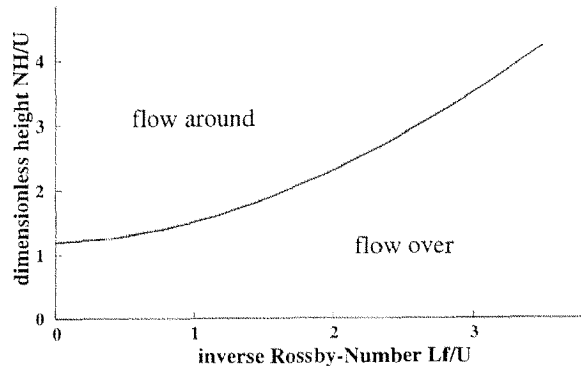


Figure 8. Regime diagram for circular topography with earth rotation (according to Trüb 1993, figure from Schär 1995).

mountain height  $\hat{H} = NH/U$ , but also essentially on the Rossby number  $Ro = U/Lf$  associated with the flow. In fact, for large Rossby numbers, the relative deceleration of upstream flow is of order  $o(\hat{H})$ , whereas it becomes of order  $o(Ro \cdot \hat{H})$  for small Rossby numbers. The transition occurs near the value  $Ro = 1$  for a roughly symmetric mountain. Since  $Ro \cdot \hat{H} = N/f \cdot H/L$  and  $\hat{H} = N/U \cdot H$ , this result can be stated in an easy to remember form: for broad mountains, it is the slope  $H/L$  which determines the barrier effect; for small mountains, it is the height  $H$ . Pierrehumbert argued that the representation of mountains in large-scale numerical models by conserving their volume instead of their height might affect their ability to accurately block the air, which in turn might reduce the numerical model's capability to simulate lee cyclones.

One further important distinction between the rotating and the nonrotating case was studied by Pierrehumbert and Wyman (1985) in a subsequent paper. They compared the barrier effect of a two-dimensional ridge with and without rotation. For the latter they found that the upstream influence can – in principle – spread infinitely far upstream provided the ridge height surpasses a critical height, which is of order  $NH/U \approx 1$ . In contrast, for the rotating case the upstream influence is limited to length scales of order  $L_R = NH/f$ , the Rossby radius of deformation. Therefore, the Coriolis force emerges as the main factor limiting the strength and the extension of the upstream deceleration and blocking.

Pierrehumbert and Wyman (1985) did not study the blocking of air impinging on a *three-dimensional* mountain. But they give a hint on the expected behaviour (Fig.9). In the nonrotating limit the upstream extension of the blocked region can be expected to be of order  $L_y$ , where  $L_y$  denotes the normal-to-flow extension of the mountain. If rotation is taken into account this length scale has to be compared with the radius of deformation  $L_R$ . If  $L_y$  is much larger than  $L_R$ , the upstream flow perturbations show some of the characteristics of “barrier winds”, i.e. strong winds which are confined in their upstream extent and flow predominantly parallel to the mountain ridge. An example for such a flow is the Tramontana wind north of the Pyrenees (see e.g. Georgelin et al. 1994, Georgelin and Richard 1994), which might at least partly be

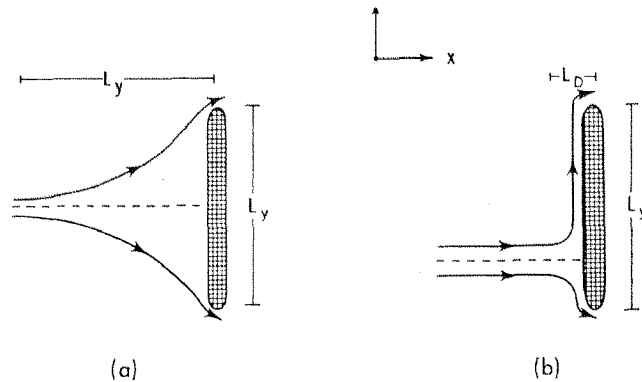


Figure 9. Schematic three-dimensional flow pattern for  $L_y \ll L_D$  (a) (potential flow in horizontal planes) and for  $L_y \gg L_D$  (b). The radius of deformation is defined by  $L_d = NH/f$ , where  $N$  is the Brunt-Väisälä frequency,  $H$  the maximum mountain height and  $f$  the Coriolis parameter (from Pierrehumbert 1985).

induced by Coriolis effects. The northerly flow impinging on the Pyrenees is deflected towards the left and feeds the Tramontana, which intensifies further by channeling effects between the southern edge of the Massif Central and the eastern side of the Pyrenees. A similar effect occurs during south Foehn in the Po valley (Fig.10). There the low-level air is often decoupled from the cross-Alpine flow aloft by an inversion, and is from east to west (see e.g Kljun 1996, Hoinka 1985, Schneidereit and Schär 1999).

Upstream blocking was one further topic where hydraulic theory was applied extensively. A concise discussion is given by Baines (1987). He looks at the mechanisms which determine the development upstream of a mountain. He starts from a single-layer hydraulic model, extends this results to multi-layer models and finally discusses the continuously stratified case. Figure 11 illustrates how complicated the regime diagram can become, even when only one single layer is present. Depending on the height and the upstream velocity quite distinct flow regimes occur, from super- and subcritical flows to completely and partially blocked flows with and without lee jumps. In multilayer flows this regime diagram becomes even more complicated.

### 2.3 Downslope Windstorms

Downslope windstorms are known all over the world, for instance, the Chinook with in Rocky Mountains and the Foehn in the Alps (for a comparison of Foehn and Chinook see e.g. Hoinka 1990; many aspects of Foehn flows are discussed in Kuhn 1989). Other downslope winds occur in Japan, at the coast of Greenland and the Norwegian coastal range. The most prominent feature of these winds are their strong, gusty winds on the lee of the mountain. Many observational and theoretical studies suggest that these winds can be understood by a common underlying physical process. The main emphasis in this research was directed towards two-dimensional mountain ridges, and three leading theories concerning the origin of the winds emerged.

As mentioned in subsection 2.1 the vertical propagation of gravity waves entails an upstream/downstream asymmetry. The air upstream is decelerated whereas the air downstream is accelerated. This fact was the initialisation for the downslope theory

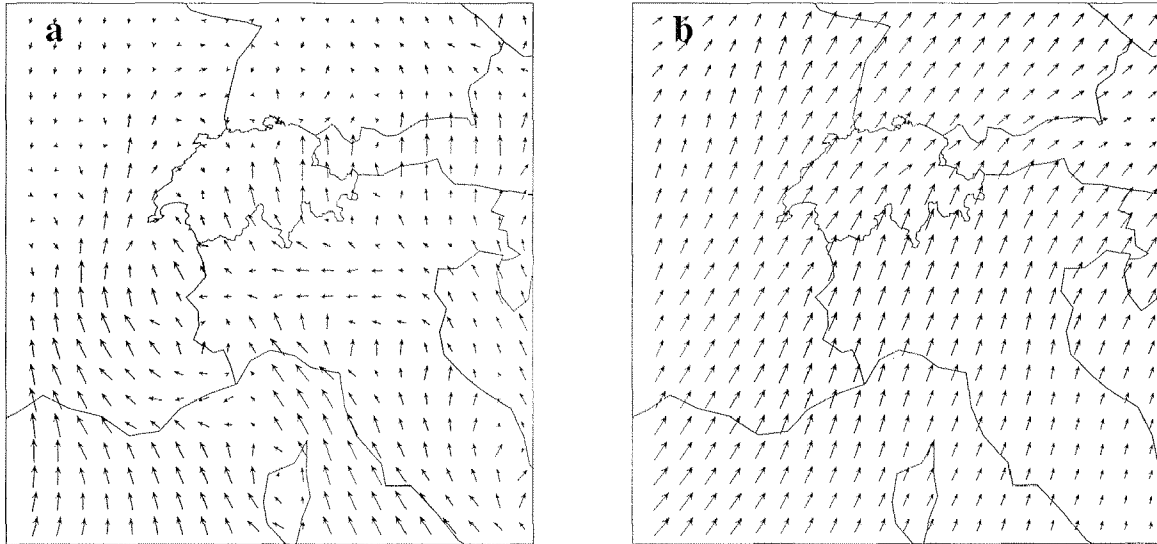


Figure 10. (a) Surface winds and (b) winds at  $500hPa$  during a strong south Foehn event (12 november 1996 00 UTC). Note the easterly Po-valley jet in the surface wind field (from Kljun 1996)

developed by Klemp and Lilly (1975, 1978). A vertically propagating gravity wave is (partially) back-reflected if it encounters a region where the Scorer parameter changes rapidly (Eliassen and Palm 1961). Klemp and Lilly found that in a multilayered atmosphere the back-reflected gravity waves can constructively interfere and hence lead to the strong winds. They demonstrated that the most important “tuning” parameter for the occurrence of a downslope windstorm in their idealised model is the tropopause height. Optimal amplification is obtained when it is located one-half vertical wavelength above ground.

Peltier and Clark (1979, 1983) and Clark and Peltier (1984) argued that it is not the tropopause height which “tunes” the atmosphere for downslope winds, but “wave-induced critical layers”. According to their theory, the gravity waves, which emanate from the mountain, intensify and finally break, hence inducing a layer with strong turbulence and local flow-reversal. The gravity waves are back-reflected at this critical layer, not by the tropopause as stated by Klemp and Lilly.

The two theories have in common that gravity waves play a crucial role. Internal gravity waves rely on the vertical stratification of the atmosphere, which itself has its predominant origin in the Earth’s gravity. The stratification manifests itself in a nearly exponential decrease of density with height. The decrease in density from ground to tropopause amounts to about 60%. Often the stratification is “concentrated” in a vertically narrow region. These inversions might then separate two “weakly” stratified regions, in which the effects of stratification might be neglected at first order. Hence, in first approximation it might be reasonable to assume that stratification is concentrated in a discontinuous inversion. Two flavours of this theory were proposed. Durran (1990) uses a shallow-water model, whereas Smith (1985) uses the concept of a dividing streamline. In the following both models are shortly discussed.

A very detailed discussion of the shallow-water model can be found, for instance, in Pedlosky (1987). In the most simple setting of a one-dimensional flow problem, the

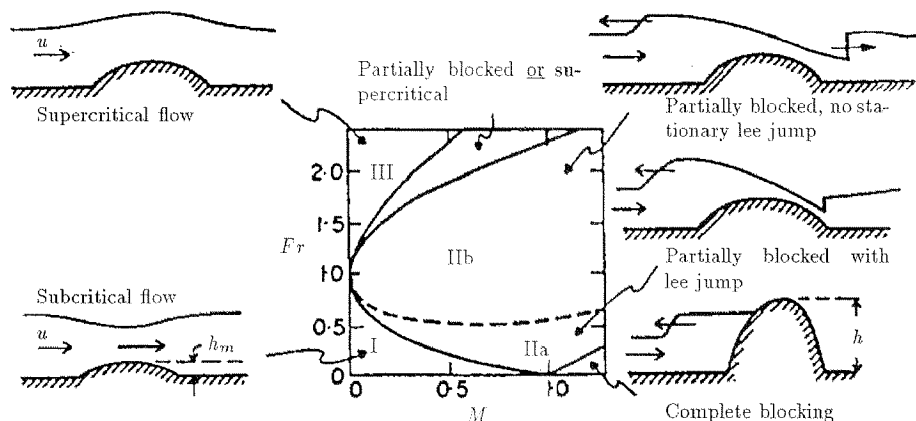


Figure 11. Hydrostatic single-layer flow over an obstacle: The flow regimes are obtained after an impulsive start from rest for various values of  $Fr = u_0/\sqrt{gd_0}$  and  $M = h/d_0$ , where  $h$  is the maximum obstacle height and  $u_0$  the speed of the obstacle relative to the initial undisturbed stream, which has depth  $d_0$  (from Houghton and Kasahara 1968).

equations of motion (conservation of momentum and mass) take the form

$$\frac{Du}{Dt} + g' \cdot \frac{\partial(h+H)}{\partial x} = 0 \quad (8)$$

$$\frac{\partial H}{\partial t} + \frac{\partial(uH)}{\partial x} = 0 \quad (9)$$

where  $g'$  denotes reduced gravity,  $u$  is the horizontal velocity, which is assumed to be independent of height, and  $H$  and  $h$  refer to the depth of the fluid layer and to the elevation of the bottom topography, respectively. It is straightforward to recast these two equations into the following form

$$(1 - Fr^{-2}) \cdot \frac{\partial(H+h)}{\partial x} = \frac{\partial h}{\partial x} \quad (10)$$

where the Froude number  $Fr$ , defined as  $Fr^2 = u^2/g'H$  is the ratio of the fluid velocity to the speed of propagation of linear shallow-water gravity waves. This dimensionless parameter plays an important role in the classification of the flow. A flow with  $Fr < 1$  is called *subcritical*. The presence of an obstacle or any disturbance can be “communicated” upstream by means of linear shallow-water gravity waves. In contrast, in the *supercritical* state ( $Fr > 1$ ) the advective velocity  $u$  is larger than the gravity wave velocity. No waves can “communicate” information upstream. The distinction between sub- and supercritical flow is closely related to the distinction between sub- and supersonic flow in engineering fluid dynamics. There, the speed of sound plays the role of the gravity wave’s velocity.

Durran (1986, 1990) gives a concise review of the three predominant theories for downslope winds. In his article he stresses the analogy between downslope windstorms and hydraulic jumps, which was also already suggested by Schweitzer (1953). Durran suggests that the upstream *subcritical* flow transforms into a *supercritical* flow over the mountain (Fig.12). Due to this transition, the flow further accelerates to the lee



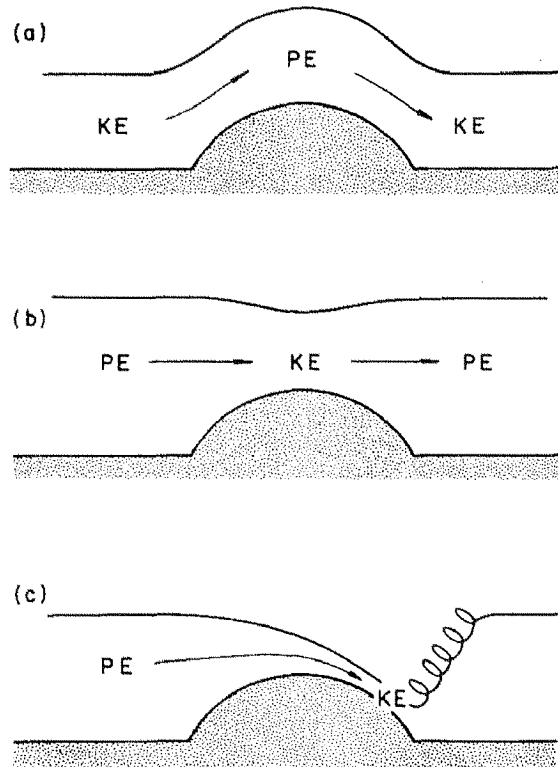


Figure 12. Behavior of water flowing over an obstacle: (a) everywhere-supercritical flow, (b) everywhere-subcritical flow, (c) hydraulic jump (from Durran 1986).

of the mountain instead of decelerating, as it would be the case for a subcritical flow. Finally, further downstream, the supercritical flow again “relaxes” into a subcritical one, the transition being marked by a pronounced change in fluid depth and being accompanied by strong turbulence. In spite of the restriction that this model does not allow vertical transport of energy by gravity waves, it captures many features of downslope winds. For instance, Miller and Durran (1991) looked at the influence of the mountain asymmetry on the development of downslope winds. More specifically, they looked at three basic free-slip atmospheric configurations: the flow beneath a mean-state critical layer, the flow in the presence of breaking waves and the flow in a two-layer atmosphere without wave breaking or a mean-state critical layer. In all three cases they found either only very weak or not dominating sensitivity to the terrain asymmetry. This gives further support for hydraulic theory as downslope theory with respect to the gravity wave mechanisms, which are expected to react more sensitive to terrain asymmetry due to varied gravity wave forcing.

The hydraulic analog proposed by Smith (1985) states that a dividing streamline separates the turbulent air mass on the lee of the mountain from the strong near-surface downslope winds (Fig.13). His theory is able to predict certain aspects of the severe wind structure, but cannot be used for forecasts. The problem arises because, although his theory is able to give the critical upstream heights of the dividing streamlines, it cannot *predict* the occurrence of such critical layers, turbulent regions or flow reversal regions which are necessary for the dividing streamline. Smith’s model assumes constant stratification. In a subsequent paper Smith and Sun (1987) dis-

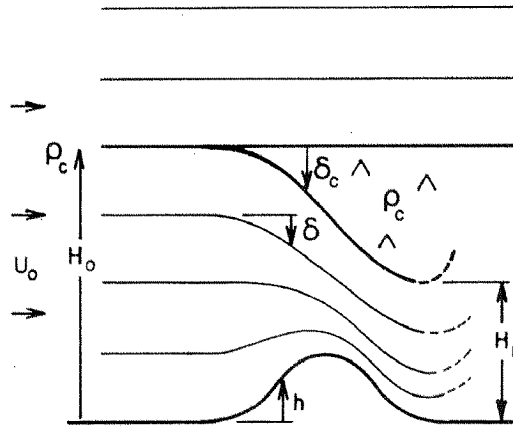


Figure 13. Dividing streamline concept from Smith (1985) for a severe wind configuration. The streamlines originating at some level  $H_0$  splits over the mountain with the lower branch descending rapidly. Above  $H_0$  only weak waves are present. The air between the split streamlines is well mixed and has little mean motion.

cussed the stratified two-layer flow over a ridge, which allowed an easier comparison with laboratory experiments. Further support for a hydraulic downslope wind theory comes from the study on high-drag states by Bacmeister and Pierrehumbert (1988). They state that “the character of the high-drag states conform well to the predictions of the internal hydraulic analysis of Smith, and cannot be explained in terms of linear resonance”.

The downslope-wind theories described above essentially address the flow over two-dimensional mountain ridges. However, many downslope windstorms are observed near complex three-dimensional topographic features. For instance, the so-called *shallow* south Foehn is restricted to narrow valley transects across the main Alpine ridge, whereas the flow above the Alpine crest is decoupled from this low-level air (see e.g. Seibert 1985). Such shallow Foehn windstorms have recently become amenable to non-hydrostatic numerical simulations (Zängl 1999). But whether the basic two-dimensional theories apply is still unclear.

## 2.4 Gap Winds

Somewhat related to the downslope windstorms are the sometimes remarkably strong gap winds. These winds occur, for example, if the low-level air is constrained horizontally by valley or fjord walls and sometimes vertically by an inversion. A look at a high-resolution map of the Alps ( $\Delta x = \Delta y = 2km$ ) shows many valleys which might be at least partly related to local windstorms (Fig.14).

This decoupling of the low-level air from the above air and wind can lead to quite unexpected behaviour. Kalthoff and Vogel (1992) show that especially under stable stratification near the surface, the air in the Rhine valley near Karlsruhe can be decoupled from the wind above. Through the pressure gradient imposed by the geostrophic wind balance, the air might then be “channeled” along the Rhine valley, down the pressure gradient. The deviation angle of the wind direction 200m and 40m above ground can exceed  $100^\circ$ , provided the wind speed is not too large. The deviation angle decreases with increasing wind speed. Wipperman (1984) gave an extended

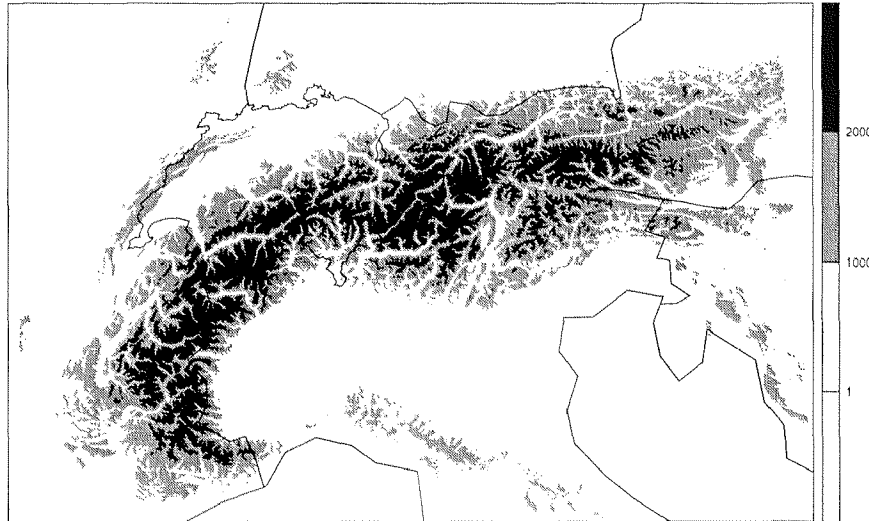


Figure 14. Alps in a  $2km$  horizontal resolution ( $1000m$  and  $2000m$  height contours, see scale bar)

theoretical explanation of channelling and counter-current using a linearised model for neutral conditions.

Scorer (1952) was one of the first to study the flow through a horizontal contraction. Subsequent studies were performed by Pettre (1982), Jackson and Steyn (1994a, 1994b), and Armi and Williams (1993). They examined especially the relationship to hydraulic theories (a more detailed review is presented in part B of the thesis).

Pan and Smith (1998), finally, used a shallow-water model to study the jet and wake behind an idealized pair of bell-shaped hills with a gap in between. They found that the flow in a level gap, i.e. with no rising terrain, can turn from its upstream subcritical state into a supercritical state by confluence alone, although the confluence has to be quite strong. In their simulations critical conditions always occurred first at the *peaks of the hills*, despite the confluence in the gap. Hence, the rising of the terrain dominates the horizontal confluence for the development of critical states. Interestingly, they could explain the jets to the lee of the gaps by the reduced supercriticality at the gap. The strong supercritical flow over the peaks leads to strong jumps and Bernoulli loss, and hence weak flow in the wake region of the hills. But the subcritical or only weakly supercritical flow in the the gap experiences only little Bernoulli loss. Therefore, a jet emerges to the lee of the gap.

## 2.5 Vortex Streets and Wakes

If the dimensionless mountain height is raised past some critical value, there is an abrupt transition to a regime where the impinging airstream experiences flow splitting and lateral deflection around the flanks of the obstacle, rather than being lifted over it (see subsection b). This transition is often accompanied by the formation of vortices to the lee of the mountain, and sometimes with the shedding of the vortices downstream. Smith and Grubisic (1993) studied in detail the structure of Hawaii's wake, which is schematically depicted in Fig.15. Most striking are the elongated counter-rotating quasi-steady eddies which enforce a strong reverse flow along the wakes axes.

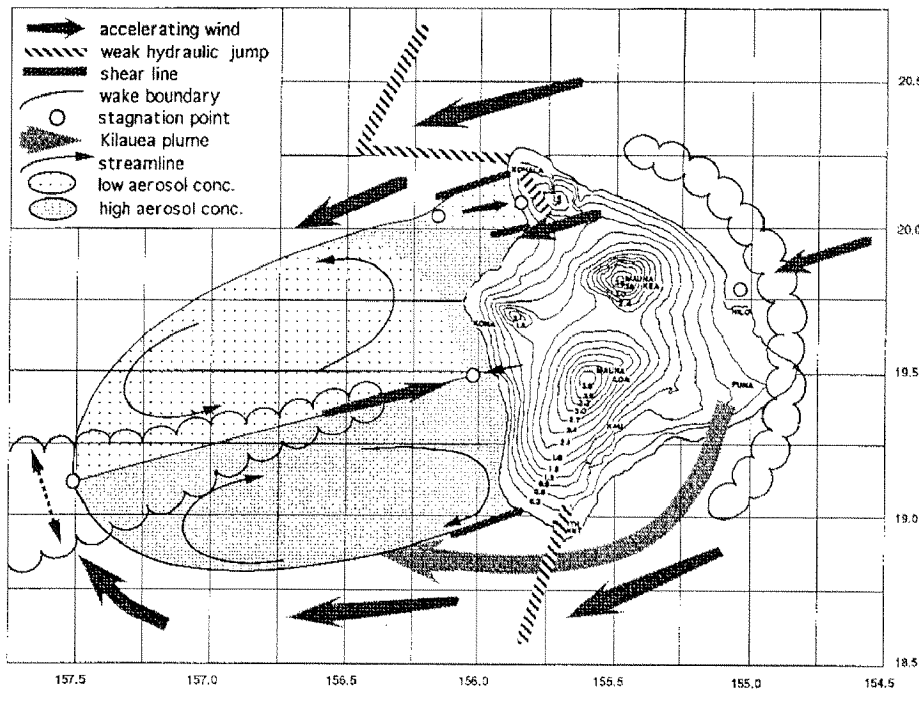


Figure 15. Summary diagram depicting features observed in Hawaii's wake. Dashed two-way arrow at the downstream end of the wake is suggesting the existence of a north to south drift. The upstream rainband and the "centerline" cloud are also outlined (from Smith and Grubisic 1993).

It is instructive to look at these lee vortices from the potential vorticity (PV) perspective. PV plays an analogous role in stratified flows as vorticity in "classical" fluid mechanics, the discussion of which can be found in many introductory texts on fluid dynamics (see e.g. Acheson 1992). Potential vorticity is defined as

$$PV = \frac{1}{\rho} \cdot \vec{\xi} \cdot \nabla \Theta \quad \text{with} \quad \vec{\xi} = \text{rot}(\vec{u}) + f \cdot \vec{k} \quad (11)$$

where  $\rho$  denotes density,  $f$  the Coriolis parameter,  $\vec{k}$  a unit vector directing towards the vertical and  $\Theta$  the potential temperature. Theoretical as well as real-case studies suggest that the vortices to the lee of a mountain are associated with PV anomalies (see e.g. Aebischer and Schär 1998). This in turn is of some dynamical importance since PV is conserved if the flow is adiabatic and inviscid,

$$\frac{D}{Dt}(PV) = 0 \quad (12)$$

Therefore, any PV anomaly which is advected downstream can persist for a long time, provided it is not destroyed by diabatic or diffusive processes (Fig.16). Aebischer (1996) found that the PV banners which emanate from isolated peaks in the Alps can reach length of up to 400km.

It was originally assumed that the individual vortices were generated by surface friction, in analogy to the processes leading to the well-known von Karman vortex streets behind cylinders in "classical" fluid dynamics (see e.g. Batchelor 1967). But Smolarkiewicz and Rotunno (1989a) showed that vertical vorticity to the lee of a mountain

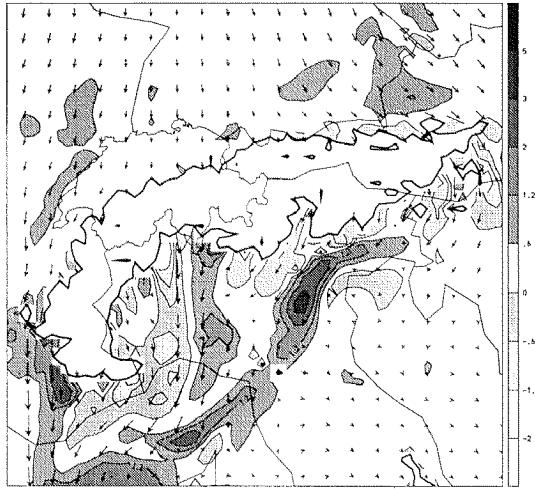


Figure 16. Potential vorticity (PV) banners south of the Gotthard pass during a north Foehn case. PV and wind vectors at 850hPa are shown.

can be generated even in absence of surface friction, by the tilting of baroclinically generated horizontal vorticity into the vertical. This process can explain the vertical vorticity to the lee of the mountain, but it still conserves PV. In recent studies it has been hypothesized that PV anomalies may develop as a result of *internal dissipation* in free slip flow over an isolated obstacle (Smith 1989a,b and Smolarkiewicz and Rotunno 1989b). Schär (1993) derived a generalization of Bernoulli's theorem which he used to confirm that dissipation can result in the creation of PV anomalies, even if the flow is initially characterized by zero potential vorticity. In a subsequent study, Schär and Smith (1993a) applied a variant of the theorem to the shallow-water flow past an isolated mountain. They state that the production of vorticity, which in the shallow water model is directly related to the presence of PV, involves either a hydraulic jump or the formation of a contact discontinuity. Both mechanisms are related to one another since both rely on the generation of variations in the Bernoulli function, which are associated with dissipation. Schär and Durran (1997) extended this shallow-water study to the stratified case. They found that the free-slip flow past a mountain can be separated into two phases. The first phase, which occurs over a dimensionless time of  $O(1)$ , is essentially inviscid and adiabatic, and hence conserving potential vorticity. It is in the second phase, which occurs over a dimensionless time  $O(10)$  to  $O(100)$ , that the flow is controlled by dissipative processes and hence potential vorticity is no longer conserved. In a first experiment, they considered a mountain flow dominated by wave breaking. The strong dissipation within the localized breaking region leads to a drop in the Bernoulli function behind the jump, thus forming a wake with decreased values of the Bernoulli function with respect to its upstream value. In a second experiment they increased the mountain height such that the flow splits on the windward side. This reduces the gravity wave activity considerably, hence suppressing the gravity wave breaking, and leads to flow separation to the lee of the mountain. The pair of counter-rotating vortices which occur in the lee and the associated recirculation leads to dissipation and a decrease of the Bernoulli function in the wake. In both cases, hydraulic jump and flow separation, the PV is generated by dissipative processes.

Schär and Smith (1993b) and Schär and Durran (1997) studied the transition from “attached” vortices to vortex shedding for the shallow-water model and the stratified case, respectively. They showed that, in both cases, the transition into the vortex shedding regime is associated with an absolute instability of the symmetrical wake (analogous to the instability found for the vortex shedding in “classical” fluid dynamics, see e.g. Hannemann and Oertel 1989). This instability feeds upon the shear which is present at the edges of the wake. In the stratified case, the individual vortices in the fully developed vortex street are associated with both PV and surface potential temperature anomalies.

These results contradict an earlier study of Sun and Chern (1994). Their numerical simulations remained symmetrical without vortex shedding until permanent asymmetries were introduced. But with the specification of asymmetric terrain or by the inclusion of the Coriolis force, the lee eddies are shed downstream, thus forming a von Karman vortex street. Sun and Chern especially stress that the Reynolds number is no good indicator of whether a vortex will stay at or be shed away from a mountain *in the atmosphere*, in contrast to the von Karman vortex streets in the lee of blunt cylinders. However, it is likely that numerical model of Sun and Chern suppressed vortex shedding due to the low Reynolds numbers considered.

### 3 Contents of the Papers

The core of this thesis consists of three papers which have recently been, or will soon be, submitted. Each of the three parts is accompanied by its own introduction where the specific problem under consideration will be addressed. The three papers relate to:

#### 3.1 Part B

Foehn flows in the Alps are often affected by gap-like features in elongated ridge-like topography. To assess the dynamics of these flows, idealized numerical experiments are conducted. The topography is taken to be a two-dimensional ridge oriented in the west/east direction with a valley transect across it and the upstream flow is assigned a westerly direction, constant wind speed, and constant Brunt-Väisällä frequency. It is shown that southerly across gap winds are possible and that the dynamics of this flow problem includes many linear and nonlinear phenomena, such as flow splitting, flow separation, hydraulic jumps, hydrostatic gravity waves and vertically trapped surface waves. Most interesting is the existence of multiple stationary solutions for the nonrotating case (two with northerly and southerly flow across the gap, respectively, and one with north/south symmetry). The relationship of the idealized setting to Alpine shallow Foehn is discussed, and additional experiments are conducted to assess the effects of surface friction and of an inversion present to the south of the ridge.

#### 3.2 Part C

The atmospheric flow past idealized isolated mountains on an f-plane is studied in the framework of linear theory. The mountain shape is described by its horizontal extensions in stream and spanwise directions and by its height. The upstream flow is assumed to be of uniform velocity and uniform stratification. The linear theory predictions for the critical mountain heights associated with near-surface stagnation

on the windward side and in the lee of the mountain, with stagnation aloft, and with intersection of streamlines with the lower boundary are determined. This results in a regime diagram which separates the regions where linear theory approximately applies from the regions where nonlinear phenomena prevail. The curves separating the different regimes show a complex behaviour with respect to the horizontal extensions and the shape of the mountain, as well as to the angle of attack of the impinging flow. The most restrictive phenomenon for the applicability of the linear theory is the intersection of the streamlines with the ground. With the exception of the quasi-geostrophic limit the dimensionless critical mountain heights are smaller than 1. Some nonlinear simulations are conducted to examine the validity of the estimates of the linear theory.

### 3.3 Part D

A real-case numerical simulation of a cold frontal interaction with the Alps is conducted, where the ALPEX-IIIb reanalysis data set of the German Weather Service (DWD) is used as initial and lateral boundary fields. After showing the superiority of this reanalysis data set over the corresponding ECMWF reanalysis data set for the case studied, the temporal development of the Mediterranean weather is discussed. This development includes flow splitting to the north of the Alps, a cold-air outbreak and Mistral between the Alps and the Pyrenees, lee cyclogenesis in the gulf of Genoa, north Foehn and Bora. Special focus is given to the low-level tropospheric flow, which is studied by means of trajectory calculations, timeseries analysis and within the framework of potential vorticity (PV). Elongated banners of PV are observed south of the Gotthard pass during the north Foehn. Furthermore, a PV anomaly at the western edge of the Alps separates and finally matures into a lee cyclone.





# PART B



# ROTATIONAL ASPECTS OF STRATIFIED GAP FLOWS AND SHALLOW FOEHN <sup>1</sup>

MICHAEL SPRENGER<sup>2</sup> and CHRISTOPH SCHÄR

## Summary

Observations of Foehn in the Alps and other mountainous regions suggest that the underlying dynamics is often affected by gap-like features in elongated ridge-like topography. To assess the dynamics of these flows, idealized numerical experiments are conducted with a hydrostatic numerical model, using  $f$ -plane geometry and a free-slip lower boundary condition. The topography is taken to be a two-dimensional ridge oriented in the west/east direction with a valley transect of depth  $\Delta H$  across it. The upstream flow is assigned a westerly direction, constant wind speed  $U$ , and constant Brunt-Väisällä frequency  $N$ . The control parameters defined by this setting are a dimensionless gap depth  $N\Delta H/U$ , the ratio between ridge height and gap depth  $H/\Delta H$ , a Rossby number describing the south-north width of the ridge, and additional parameters associated with the shape of the gap. With intermediate Rossby numbers ( $Ro \approx 1$ ) the setting resembles that of shallow Alpine south Foehn cases which are characterized by a cross-Alpine flow essentially confined to valley transects. For small dimensionless gap depths and large Rossby numbers, the flow follows the predictions of linear theory and takes on an approximately symmetric pattern with respect to the ridge line. For  $N\Delta H/U > \approx 1$ , flow separation and splitting takes place upstream and downstream of the gap, respectively. The flow within the gap decouples from the flow aloft and is driven by the geostrophic south-north pressure gradient to yield a Foehn-like flow. It is demonstrated that the limit  $f \rightarrow 0$  is singular (i.e. the flow solution does not converge towards the symmetric  $f = 0$  solution), and that there exist multiple stationary solutions for  $f = 0$  (two with northerly and southerly flow across the gap, respectively, and one with north/south symmetry). The existence of these multiple steady states is related to a wake instability, yet vortex shedding is suppressed by the presence of the ridge downstream of the gap. Additional simulations are presented which demonstrate that a transient external forcing can induce transitions between the multiple flow solutions. The relationship of the idealized setting to Alpine shallow Foehn is discussed, and additional experiments are conducted to assess the effects of surface friction and of an inversion present to the south of the ridge.

---

<sup>1</sup>submitted to *Quart. J. Roy. Met. Soc.*

<sup>2</sup>Corresponding author: Swiss Federal Institute of Technology, GI-ETH, Winterthurerstr. 190, CH-8057 Zürich, Switzerland, e-mail: sprenger@geo.umnw.ethz.ch

## 1 Introduction

There is an extensive body of literature on the two-dimensional dynamics of downslope windstorms. This research has served to shed light upon the basic properties of gravity-wave generation and propagation (see the reviews of Smith 1979; Durran 1990), the role of nonlinear effects (Long 1955), the interaction of gravity waves with the vertical stratification profile (Klemp and Lilly 1975) and critical levels induced by breaking waves (Peltier and Clark 1979), the relationship between continuously stratified and hydraulic flows (Smith 1989; Durran 1990), and many more additional features of this fascinating flow problem. However, many of the observed cases of downslope windstorms cannot be explained by the classical two-dimensional theories of downslope windstorms. In the Alps for instance, about 12% of the observed Foehn cases are classified as "shallow" (Seibert 1985). In contrast to the deep Foehn, the cross-Alpine southerly flow is then essentially confined to the valley transects whereas the mid-tropospheric flow can have a westerly or even a north-westerly direction. An impressive case of this type is the so-called Gueller Foehn which occurred on February 13, 1976 (Gueller 1979). The upper level synoptic chart for this case shows a north-westerly flow (see Fig.1), yet surface observations in the upper Rhine valley (along the border between Austria and Switzerland) showed the occurrence of southerly Foehn with its typical features (warm and dry conditions with relative humidity as low as 30%, strong southerly flow with peak gusts up to 20 m/s), yet the southerly flow did not extend past the Alpine ridge line but was confined to valleys. In the mid troposphere, north-westerly flow prevailed associated with an approaching cold front which ultimately terminated the Foehn storm. Despite some similarity with other downslope windstorms such as the Bora, which is often associated with reversed flow at upper levels and concomitant critical levels (Smith 1987), shallow Foehn and other gap flows cannot be idealized by two-dimensional geometry.

Three-dimensional gap flows are very common in many mountainous regions. One of the early detailed accounts is that of Scorer (1952) who studied the flow past the Straits of Gibraltar. Scorer noted that a great stability below mountain-top level and a pronounced pressure gradient along the gap are conducive to strong winds. He stressed the importance of a cold-air pool underneath an inversion, and interpreted the pressure fall to the lee of the gap as being maintained by the descent of the inversion as the wind blows across the gap. Scorer also noted that "the air converging towards the narrows follows fairly smooth streamlines" but when it emerges from the gap it "does not readily fan out up a pressure gradient to a lower velocity but rather tends to emerge as a jet with large standing eddies which can be observed in the surface isobars, or smaller moving ones which are observed by aircraft as regions of very changeable wind, on the side of the jet." Several subsequent studies attempted to interpret gap winds as a hydraulic phenomenon. Pettre (1982) studied the Mistral along the Rhône valley and compared it with results from a simple shallow water model. He suggested that a lateral valley constriction near Valence was playing the role of a hydraulic control and promoting a transition to supercritical conditions, and he also detected a hydraulic jump-like feature further downstream. Jackson and Steyn (1994a) carried out a detailed field investigation of the gap flow in Howe Sound, British Columbia, and present nonhydrostatic high-resolution integrations. In a companion paper (Jackson and Steyn 1994b) they subsequently employed a simple quasi-two-dimensional hydraulic model to interpret their observations. The model did include an external pressure gradient, surface friction, and accounted for

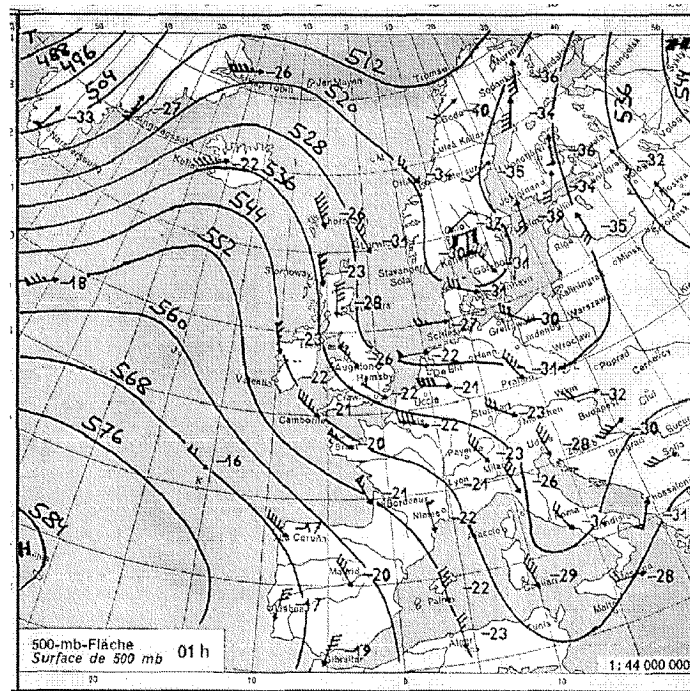


Figure 1. 500hPa geopotential demonstrating the shallow south Foehn on 13 february 1976, 01 h (SMA 1976)

the variable cross-section of the valley along the gap axes. Jackson and Steyn concluded that the prime force balance for supercritical flow was between the external pressure gradient and surface friction, while for subcritical flow it was between the external and the height pressure gradients.

In all of the aforementioned studies consideration was given to events characterized by a pronounced inversion. However, even for continuously stratified upstream flow profiles, gap-induced transitions to supercritical flow were detected. Armi and Williams (1993) studied the steady hydraulics of a continuously stratified fluid flowing from a stagnant reservoir through a horizontal contraction with laboratory experiments and theoretical methods. Their analysis reveals a succession of transitions (with respect to individual wave modes) from subcritical to supercritical conditions as the flow accelerates through the constriction. This flow problem is related to the hydraulic theory of downslope windstorms, where similar transitions are induced by a topographic ridge (cf. Smith 1989; Durran 1990).

Most of the recent research on channeling and deflection of continuously stratified flows restricts attention to flow past three-dimensional isolated topographic obstacles with circular or elliptic shapes. Idealized numerical simulations have in particular demonstrated that the transition from the quasi-linear "flow-over" to the non-linear "flow-around" regime shows some of the characteristics of a bifurcation (Smith and Gronas 1993), in which the dimensionless mountain height  $\hat{H} = NH/U$  acts as the control parameter. If the dimensionless mountain height is raised past some critical value, there is an abrupt transition to a regime where the impinging airstream experiences flow splitting and lateral deflection around the flanks of the obstacle, rather than being lifted over it. Such flows possess a wake with vortices and sometimes vortex shedding (Hunt and Snyder, 1980; Smolarkiewicz and Rotunno 1989; Schär and

Durran 1997).

More complex topography has also been considered. For instance, Saito (1993, 1994), Clark et al. (1994) and Zängl (1999) conducted numerical experiments of flow over a two-dimensional or isolated mountain ridge transected by a pass-like feature, which was taken to represent the topography of the island of Shikoku, the front range, and the Inn valley in the Alps, respectively. All these studies detected an intensification of the Foehn flow along the gap transecting the ridge, but attention was restricted to configurations with the incident flow approximately perpendicular to the ridge, thus not addressing cases of shallow Foehn as the one alluded to above.

Beside the aforementioned effects, rotation may play some role as well. Theoretical studies suggests that rotational flow past obstacles should be balanced (i.e. qualitatively amenable to quasi-geostrophic dynamics) as long as  $Ro \cdot \hat{H} < \approx 0.5$  for three-dimensional circular topography (Schär and Davies 1988; Trüb 1994), and  $Ro \cdot \hat{H} < \approx 1$  for two-dimensional topography (Trüb and Davies 1995). Here  $Ro = U/Lf$  is the Rossby number defined by the horizontal scale of the obstacle. Introducing typical Alpine values puts  $Ro \cdot \hat{H}$  in the range between 0.2 and 2, thus the flow belongs to the intermediate regime where rotational and gravity wave effects are both important, but neither of the two dominates. According to recent studies the critical mountain height is increased by rotational effects, and thereby makes flow-splitting less likely as compared to the flow past a smaller-scale obstacle of the same height (Trüb 1993; Olafsson and Bougeault 1997; Bauer 1997). In relation to the Alps, there is thus a tendency for the flow to be over the Alps on the scale of the obstacle, but around individual massifs and peaks (see Aebischer and Schär 1998).

In the present study consideration will be given to an idealized Alpine shallow Foehn setting. A schematics of this is shown in Fig.2. The idealized Alps are shown as an elongated two-dimensional ridge which is intersected by a gap across it, representing a major Alpine pass such as the Gotthard or Brenner section in Switzerland and Austria, respectively. The "upstream" flow is taken to be a westerly flow along the ridge line. The implied role played by rotation and flow-splitting effects is suggested by the balance of forces as indicated in the figure. Upstream of the gap the flow is in geostrophic balance, i.e. the pressure gradient force acting towards north is balanced by an equally large Coriolis force acting towards south. This large-scale balance cannot be maintained within the gap provided it is deep enough to suppress east-west motion of air parcels. If the flow is channelled, the Coriolis force in the direction of the valley axes disappears and there is a net acceleration of the flow towards north.

The schematics in Fig.2 is closely related to the existence of counter currents in deep valleys such as the Rhine valley near Karlsruhe (Wippermann 1984; Kalthoff and Vogel 1992). Similar as in our schematics, the geostrophic balance is disrupted by the decoupling of the flow within the valley from aloft, while the synoptic pressure gradient is hydrostatically transmitted into the valley and thereby induces accelerations perpendicular or even opposite to the upper-level flow. However, in the aforementioned studies, the valley bottom is quasi-horizontal, and thus there are major differences to the shallow Foehn schematics in Fig.2: First, as a result of the vertical deflection of air parcels which transit along the gap over the ridge, gravity wave generation and propagation will interact with the basic currents. Second, the complex three-dimensional structure of our setting can give rise to flow separation and splitting in the vicinity of the gap, and these may induce anomalies of potential vorticity, which are not present

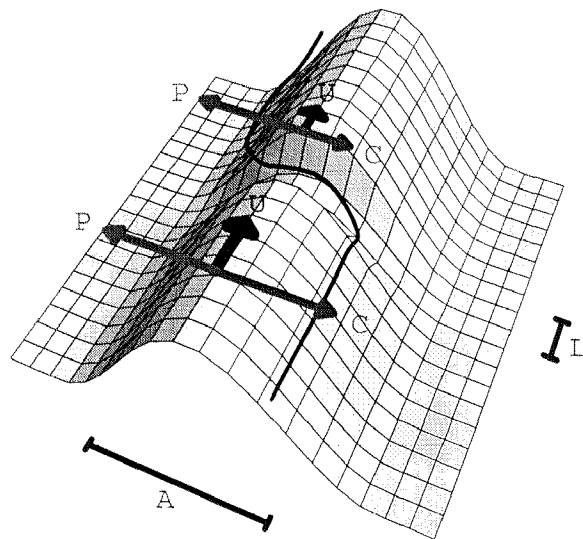


Figure 2. Schematics of idealized model problem with flow along a ridge of north/south half width  $A$  transected by a gap of west/east half width  $L$ . The bold line shows a trajectory of an air parcel. The arrows show the balance of forces on the centerline. Upstream of the gap the flow is in geostrophic balance, while within the gap there is an imbalance between pressure ( $P$ ) and Coriolis ( $C$ ) force.

in the essentially two-dimensional setting alluded to by Wippermann. The separation and splitting will induce wake features to the lee of the gap. Such configurations have been investigated for instance by Pan and Smith (1998). They utilized nonrotating shallow-water dynamics and compared their results with Synthetic Aperture Radar data taken near Unimak Island in the Aleutian Chain.

The aforementioned hypothesis emphasizes the role of external pressure gradients. It is indeed interesting to note that the relevance of the south/north pressure gradient for Alpine Foehn has for long been recognized in the operational forecasting practice. Most Alpine weather services use a Foehn forecasting rule which gives ample weight to the pressure contrast between surface stations on either side of the main Alpine ridge. In Switzerland for instance, a variant of the Widmer Foehn test is used (Widmer 1966; Courvoisier and Gutermann 1971). The underlying rule implies that a south/north pressure contrast of  $> 18.3\text{hPa}$  between Venice and Tours is a fairly reliable precursor for the onset of southerly Foehn within the next 36h. In this context, it is worth noting that the classical two-dimensional downslope windstorms theories would not yield a north-south pressure gradient unless the Foehn flow is already established.

The specific goal of our study is to assess the mechanism and associated processes that result from the hypothesized schematics in Fig.2. To this end highly idealized simulations are conducted using a hydrostatic numerical model with free-slip lower boundary conditions on a rotating  $f$ -plane. Particular objectives are to assess the nature of the flow response, estimate the strength of the induced southerly cross-ridge flow, study its sensitivity with respect to external control parameters, and explore the role played by gravity waves and flow separation/splitting effects.

The paper is organized as follows: Section 2 describes the utilized numerical model and its configuration for the current study. Section 3 contains an analysis of the quasi-

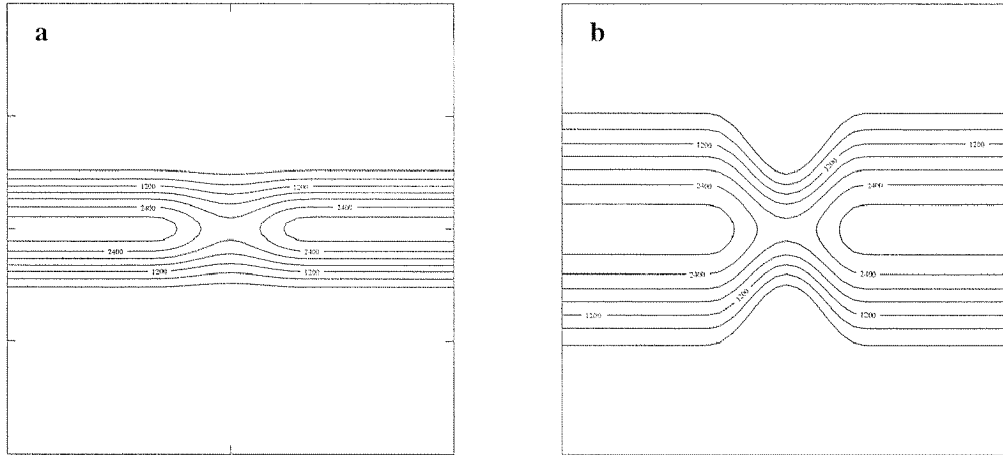


Figure 3. Idealized orography as in the (a) standard setting ( $A = 150\text{km}$ ,  $H = 3000\text{m}$ ,  $\Delta H = 900\text{m}$ ,  $L = 75\text{km}$ ,  $\beta = 0$ ) and (b) with valleys to the north and south of the gap ( $A = 300\text{km}$ ,  $H = 3000\text{m}$ ,  $\Delta H = 900\text{m}$ ,  $L = 75\text{km}$ ,  $\beta = 0.5$ ).

linear regime, which is associated with gap depths that are too small to induce the proper channelling of the flow. In section 4 the nonlinear regime is assessed to test the basic hypothesis of the study. The sensitivity of the flow response and the existence of multiple flow solutions will then be addressed in section 5 and 6, respectively. Additional factors which make the flow problem more realistic – such as the presence of a pre-existing inversion to the south of the ridge and effects of surface friction – are taken into consideration in section 7. Some concluding comments follow in section 8.

## 2 Definition of model problem

Consideration is given to the flow of a stratified stream of air along a two-dimensional mountain ridge of height  $H$ . To mimic a mountain pass the ridge is transected by a gap-like feature (Fig.3). Both the ridge profile (in the  $y$  direction), and the gap profiles (in the  $x$  direction) are assigned a cosine shape with halfwidth  $l$  given by

$$s(\chi, l) := \begin{cases} \cos^2(\pi\chi/2l) & : |\chi| < l \\ 0 & : \text{else} \end{cases} \quad (1)$$

Here  $\chi$  stands for either  $x$  or  $y$ , and  $l$  denotes a scale parameter. The topography is specified as

$$h(x, y) := h_0(x) \cdot s(y, a_0(x)) \quad (2)$$

where the width  $a_0(x)$  and height  $h_0(x)$  of the ridge are specified as functions of the along-ridge coordinate according to

$$h_0(x) := H - \Delta H \cdot s(x, L) \quad (3)$$

$$a_0(x) := A \cdot \{1 - \beta \cdot s(x, L)\} \quad (4)$$

Here the parameters  $H$  and  $A$  denote the height and width of the ridge away from the gap. The gap itself has depth  $\Delta H$  and an along-stream width  $L$ . The parameter



$\beta$  allows to reduce the width of the ridge in the vicinity of the gap (cf. Fig.3b). In the standard setting, the parameters are assigned the dimensional values of  $A = 150km$ ,  $H = 3000m$ ,  $L = 75km$ ,  $\Delta H = 900m$  and  $\beta = 0$ . The associated orography is shown in Fig.3a. After assigning the so-defined orography to the numerical grid, a simple filter is applied in order to eliminate 2-grid waves.

The topography parameters as given above are chosen such as to roughly represent the Alpine setting. Realistic passes across the Alps (such as the Gotthard or the Brenner section) are characterized by narrow valleys with scales down to a few kilometers. However, these passes are embedded in larger scale dips in the Alpine ridge line, with horizontal scales not unlike to the ones used above. Nevertheless, the poor representation of the narrow inner part of these cross-Alpine valleys is a limitation to our study and restricts direct applicability.

The upstream flow is of uniform stratification (Brunt-Väisälä frequency  $N$ ) and wind speed  $U$ , with the standard values of  $N = 10^{-2}s^{-1}$  and  $U = 10m/s$ .

Consideration will be given to hydrostatic dynamics on an  $f$ -plane with a free slip lower boundary condition. As a result of the hydrostatic scaling (Smith 1989; Smith and Gronas 1993) the model problem is then determined by four dimensionless parameters. These may be chosen to be a dimensionless measure of the gap depth

$$\hat{\Delta H} = N \cdot \Delta H / U, \quad (5)$$

the ratio between ridge height and gap depth

$$\delta = H / \Delta H, \quad (6)$$

a zonal Rossby number based upon the gap width

$$Ro^x = U / (L \cdot f), \quad (7)$$

and the aspect ratio

$$\epsilon = L / A \quad (8)$$

which measures the ratio between the widths of the ridge and the gap. For the standard setting listed above and a mid-latitude Coriolis parameter of  $f_0 = 10^{-4}s^{-1}$ , the dimensionless parameters take the values  $\hat{\Delta H} = 0.9$ ,  $\delta = 3.33$ ,  $Ro^x = 1.33$ , and  $\epsilon = 0.5$ . Theoretical considerations suggest that the flow along the ridge is in good geostrophic equilibrium, while the flow across the gap is both affected by the background rotation and gravity wave propagation ( $Ro^x = 1.33$ ). The dimensionless depth of the gap ( $\hat{\Delta H} = 0.9$ ) is close to the critical dimensionless mountain height for flow past isolated bell-shaped topography (Smolarkiewicz and Rotunno, 1989; Smith and Gronas, 1993), and thus we expect substantial nonlinear effects. In addition, as a result of choosing a fairly broad gap, we expect the hydrostatic approximation to well apply ( $U / (NL) = 0.013$ ).

Numerical solutions are obtained using a hydrostatic model which is derived from the meso-scale numerical weather prediction model of the German Weather Service (DWD) and the Swiss Meteorological Institute (SMI). A detailed description of the model is given by Majewski (1991), and information about its operational use can be found in quarterly DWD reports (Majewski and Schrodin 1999). The model is very flexible and was used in research mode for case studies of Alpine flows (Aebischer and

Schär 1998), predictability studies (Fehlmann and Davies 1997), and as a regional climate model (e.g. Frei et al. 1998). The present simulations will use an  $f$ -plane option and most of the parameterizations are switched off. The prognostic variables of the model are surface pressure, the horizontal wind components, and temperature. At the upper boundary a KDB-type gravity-wave absorber (Klemp and Durran 1983; Bougeault 1983) is used. Its implementation in pressure coordinates is due to Herzog (1995). The only parameterization package employed is a turbulence formulation with a second-order closure scheme of hierarchy level 2 (Mellor and Yamada 1974; see also Müller 1981). Most of the simulations (except for some simulations in section 7) will be performed using a free-slip lower boundary conditions. Consistent with the free-slip lower boundary condition, the vertical turbulent fluxes of heat and momentum are set to zero at the lower boundary, while they may take on nonzero values throughout the model atmosphere. At the lateral boundaries, the model is driven by an analytical background flow along the two-dimensional ridge using relaxation boundary conditions (Davies 1976).

The standard experiments are conducted using  $\Delta x = \Delta y = 5.6km$  and  $121 \times 81$  gridpoints in the horizontal. Most diagrams shown in this paper restrict attention to the inner part of the computational domain with  $60 \times 40$  gridpoints. In the vertical 34 levels are used. Their density near the surface is somewhat increased in order to better resolve the dynamics near the surface. The lowermost level is approximately 50m above ground. In the experiments with surface friction we used a one-way nesting technique. Details will be presented in the relevant section.

To validate the model for our configuration, some initial tests were performed based upon the hydrostatic scaling laws. In a first test, we halved the values of  $f$ ,  $U$  and  $N$  with respect to the standard setting. With these changes all the dimensionless parameters are unaffected. In a second test the scaling laws in the absence of rotation ( $f = 0$ ) were tested by doubling  $A$  and  $L$ . In this experiment, the horizontal grid spacing  $\Delta x$ ,  $\Delta y$  was doubled as well such that the gap is equally resolved. In both tests, the experiments did yield very similar results as in the standard setting, except for some minor differences which presumably originate from the turbulence scheme (which does not satisfy the hydrostatic scaling laws).

### 3 Linear regime

In this section we show that the shallow south Foehn to be discussed later is a predominantly nonlinear phenomenon. This is checked by performing a simulation where the linear approximation applies, i.e. where all perturbation fields scale linearly with the gap depth  $\Delta H$ . Here we choose a quasi-linear value of  $\Delta H = 300m$ , yielding a dimensionless gap depth  $\hat{\Delta H}$  of 0.3.

The numerical integration is carried out to  $t=80h$ , which is well sufficient to approach steady state. Results are shown in Fig.4. The pattern of vertical wind and the potential temperature in the east/west cross-section running along the ridge crest and cutting across the gap (Fig.4a) shows the typical signature of vertically propagating hydrostatic gravity waves. The angle of ascent of the wave-train is in accord with the dispersion relation for gravity waves and is essentially determined by the zonal width of the gap. The vertical displacement of the potential temperature contours tilt upstream with height, indicating an upward transport of energy and a downward transport of momentum. The low-level  $\Theta$ -contours follow the topography and there is

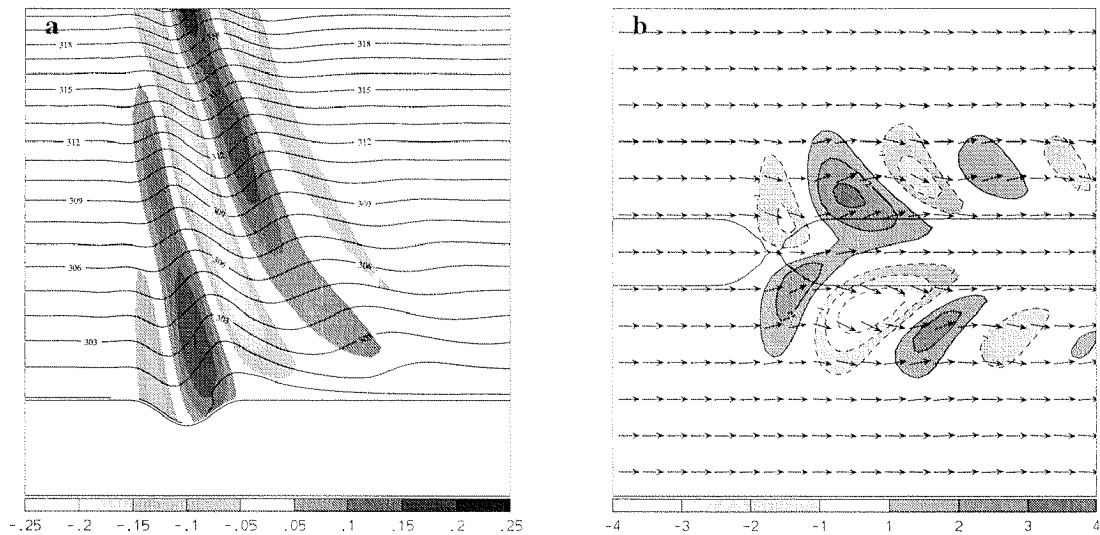


Figure 4. Linear flow regime with a gap depth of  $300m$ . (a) Vertical velocity  $w$  (shaded, scale bar) and potential temperature  $\Theta$  (solid lines) in a west/east-section along the ridge and (b) surface wind vectors and contours of meridional wind  $v$ . The flow is from left to right.

neither indication of flow separation nor flow splitting. The top-view of surface wind speed and wind vectors (Fig.4b) reveals almost perfect south-north symmetry.

The most prominent feature in Fig.4b is the wave train which appears downstream of the gap both on the northern and southern flank of the ridge. These waves have a vertical extension of  $\approx 500m$ , a horizontal wave length of  $\approx 100km$ , and they do not depend on the Coriolis parameter as is revealed by further simulations with different values of  $f$  (not shown). The existence and properties of these waves can be explained by a simple parcel argument. Assuming an approximately undisturbed stratification  $N$  along the mountain's slopes, and a small meridional displacement  $\delta s$  from the upstream position, the equation of motion for an air parcel located directly on the topography is obtained from combining the vertical and meridional momentum equation to

$$\frac{D^2}{Dt^2}\{\delta s\} = -(N \cdot \sin \alpha) \cdot \delta s \quad (9)$$

where  $\alpha$  denotes the slope angle of the northern or southern flank of the ridge. This is an oscillation equation with the oscillation period given by  $\sin \alpha \cdot 2\pi/N$ . Multiplication with the undisturbed upstream velocity  $U$  yields the wavelength  $\lambda = \sin \alpha \cdot 2\pi U/N$ . If the angle  $\alpha$  is small,  $\sin \alpha$  may be replaced by the slope  $a$  to yield

$$\lambda = a \cdot 2\pi \cdot U/N \quad (10)$$

Inserting the appropriate values for our simulation yields the observed order of magnitude for the wavelength ( $\lambda \approx 100km$ ). The scaling exhibited by (10) was validated using additional numerical experiments with modified slope and stability parameters.

The waves can thus be interpreted as a trapped gravity mode, where the terrain modifies the buoyancy force such as to yield a reduced oscillation frequency. These

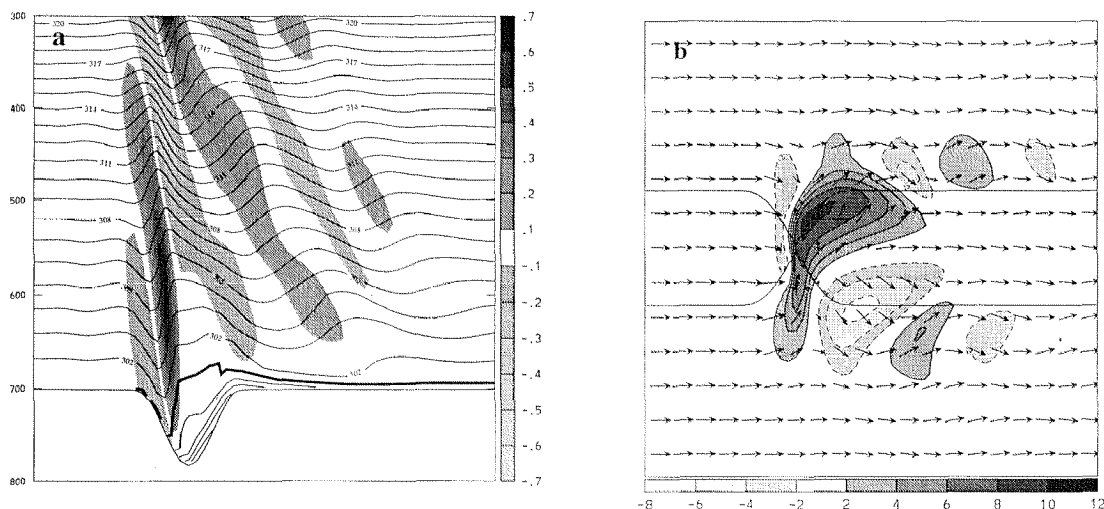


Figure 5. As Fig.4, but for nonlinear standard case with a gap depth of  $900m$

waves are distinct from topographic Rossby waves (cf. Pedlosky, 1987) since they do not rely on background rotation. However, since the mode is shallow, one expects that boundary layer processes (which are neglected in the current simulation and above analysis) would be able to effectively damp the mode. This will be confirmed in section 7. Similarly, we do not expect that these modes play a significant role in the Alpine setting, where complex small-scale topography inhibits the meridional displacement of air parcels on the mountain slopes.

#### 4 Nonlinear regime

In the present and the subsequent sections we turn attention to the nonlinear regime. We choose a gap depth of  $900m$ , yielding a pass height of  $2100m$ . The dimensionless gap depth, which is a measure for the nonlinearity of the flow, takes on the value  $\Delta\hat{H} = 0.9$ . Results are shown in Fig.5.

In contrast to the linear regime (Fig.4), a strong southerly wind through the gap can now be identified (Fig.5b), and its maximum is attained on the northern downhill slope of the gap. The maximum wind speed has a remarkable amplitude of  $16m/s$ , which is not unlike the values obtained by two-dimensional downslope wind theories. On the eastern flank of the gap the southerly flow extends up to the crest of the mountain ridge. A closer inspection of the winds within the gap (Fig.6) also reveals flow splitting to the south-east and flow separation to the west of the gap, including a cyclonic vortex feature to the south, which results in a strong redirection of the low-level winds, which includes a weak easterly component in the gap. Thus, the picture emerges that the strong southerly flow across the gap is closely related to flow separation and flow splitting processes induced by the presence of the gap.

The flow separation to the south-west of the gap results in a well-defined vortex-like flow feature, while the corresponding vortex to the north takes on the form of a pronounced shear line which extends away from the topography and which confines

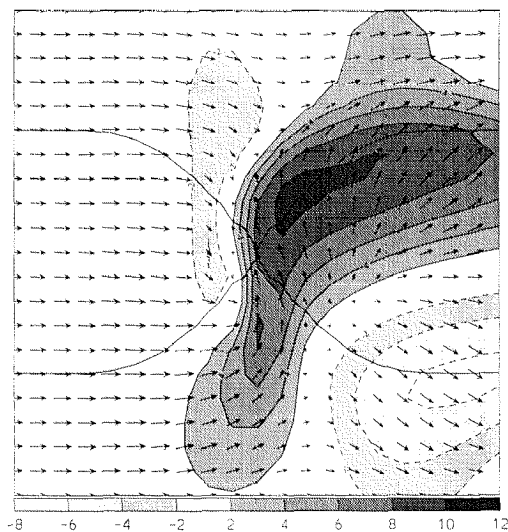


Figure 6. Closer look at gap winds (subdomain of Fig.5b)

the zone of southerly flow to the north. The separation of the flow to the west of the gap is also evident in the isentropic distribution along the east/west cross-section (Fig.5a). In contrast to the linear flow regime (Fig.4a) the isentropes separate from the topography and exhibit a hydraulic jump like behaviour. To further illustrate the extent of the decoupling of the flow across the gap from aloft, the 301K-contour in Fig.5a, which runs along the ridge, is shown in bold.

The vertical wind velocity in Fig.5a suggests the presence of two – rather than one – wave trains of vertically propagating gravity waves. The first emanates at the separation region near the western flank and its steep angle of ascent is associated with the small horizontal extent of its source region. The second wave train is similar to that observed in the linear case, has a smaller angle of ascent, and it appears that the gap as a whole acts as its source region.

For further analysis we compare in Fig.7 the reduced surface pressure of the nonlinear and linear experiments. It is obtained by removing the hydrostatic part of the pressure distribution (determined from an undisturbed basic state flow with stratification  $N$  and  $U$ ), such that only the geostrophic and dynamically-induced ageostrophic parts remain. In the nonlinear case (Fig.7b) there is a well-defined pressure ridge at the south-eastern flank of the gap, which will be referred to as “Foehn-knee”, a term which is borrowed from the common synoptic terminology for this feature. Note also how the north/south pressure gradient is much enhanced in the gap region as compared to the linear case. This enhancement is a result of gravity wave propagation and is beyond the simple driving mechanism discussed in Fig.2.

## 5 Sensitivity Experiments

In the following subsection we present systematic sensitivity studies of the standard nonlinear solution with respect to (5.1) the topography’s shape and size, and (5.2) the

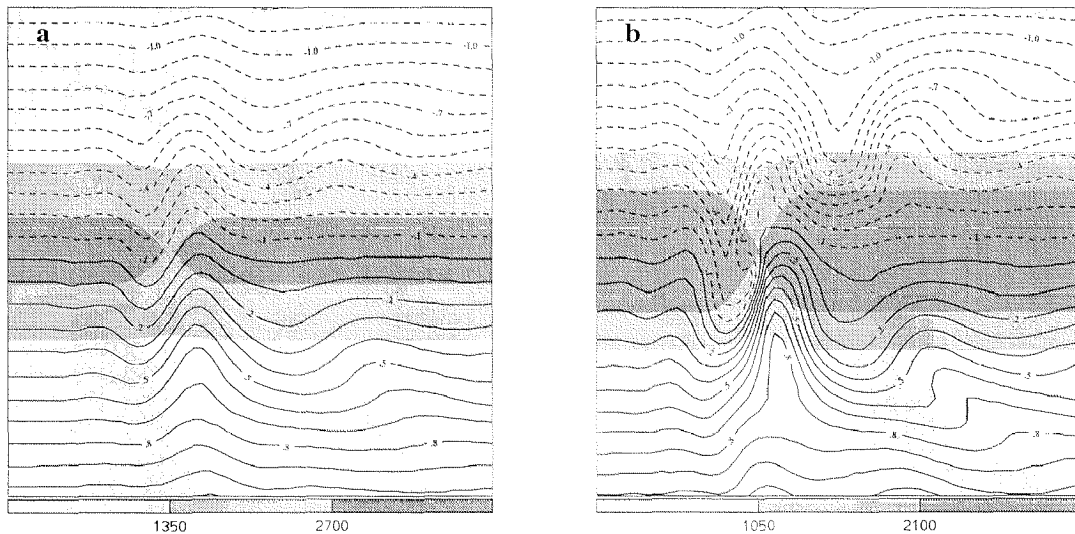


Figure 7. Reduced pressure in (a) the linear ( $\Delta H = 300m$ ) and (b) the nonlinear ( $\Delta H = 900m$ ) flow regime. Note the strong amplification of the pressure contrast in (b).

upstream flow speed. The sensitivity of the flow with respect to background rotation will be addressed in section 6.

### 5.1 Sensitivity to the topography's shape and size

The first set of sensitivity experiments address the role of the topography's scale in terms of the north/south ridge width  $A$  and the west/east gap width  $L$ . Since a modification of both these parameters by the same factor changes the overall scaling of the topography, we also obtain information on the influence of the overall Rossby number. Results are shown in Fig.8 for four experiments, and these can be compared to Fig.5b.

If the east/west-extension of the gap is halved or doubled (Fig.8a,b), the cross-Alpine southerly flow persists, but it becomes more concentrated near the eastern slope of the gap. If the gap width is doubled (Fig.8b) the decoupling of the air in the gap from aloft is reduced. This can be partly understood by the weakening of the flow-splitting at the south-eastern flank of the gap, consistent with a decrease in the zonal Rossby number. On the other hand, if the gap width is halved, a Lagrangian argument applies: Since there is some easterly flow component almost throughout the gap, a narrower gap implies that the air parcels stay only briefly within it and thus feel the south/north pressure gradient only for a short period of time. Thereby the net northward acceleration is reduced. To summarize, the zonal Rossby number  $Ro^x = U/L \cdot f$  is important for the splitting and redirection of the flow at the south-eastern slope of the gap. An intermediate east/west-width of the gap seems optimal to induce strong southerly winds across it.

The width of the Alpine ridge has a strong impact upon the character of the flow solution. Doubling of the width (see Fig.8d) leads to substantially stronger southerly winds across the gap, and the wind maximum is more centered on the gap transect. Similarly, reducing the ridge width results in reduced southerly flow (cf. Fig.8c). This

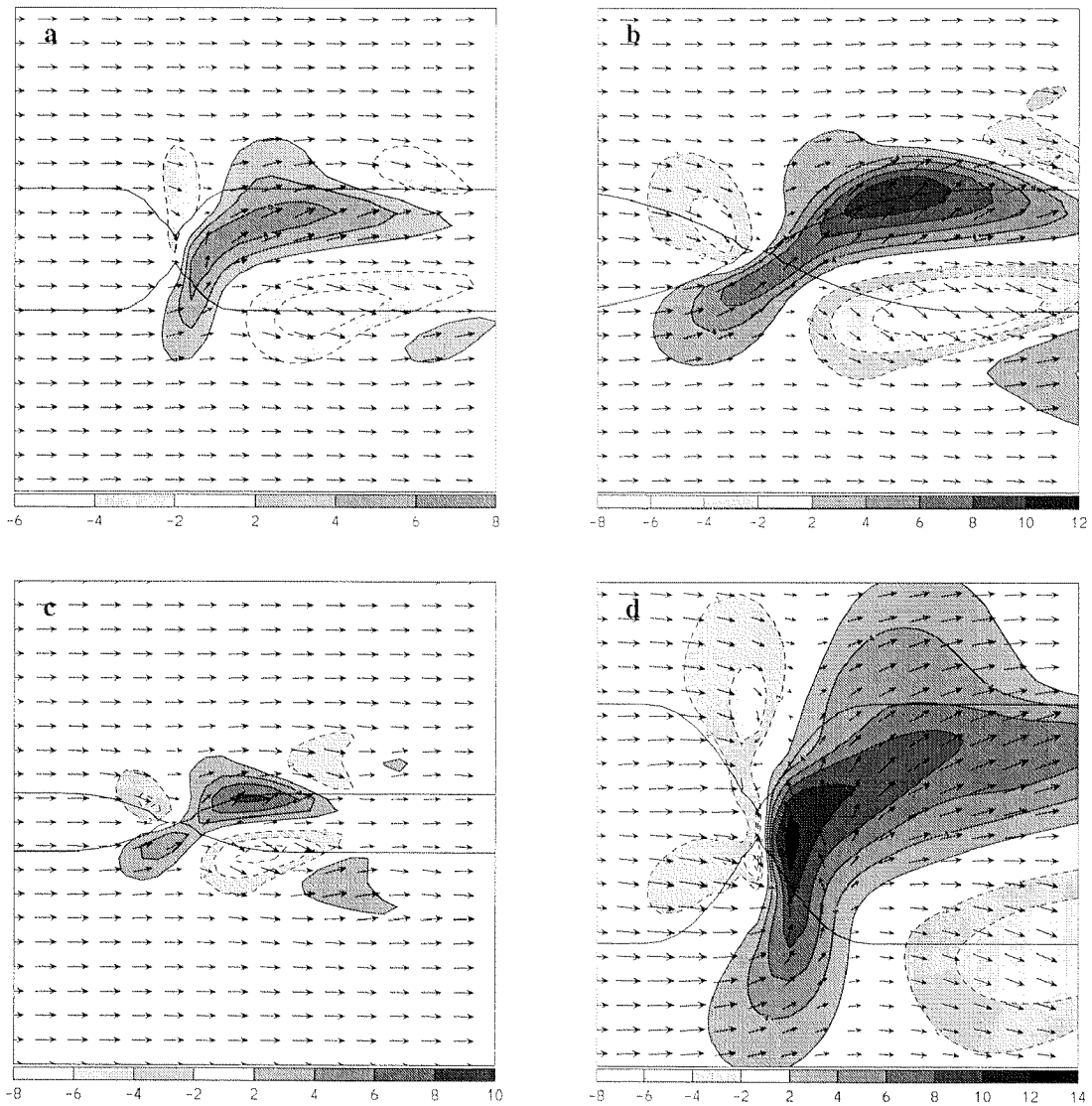


Figure 8. As Fig.5b, but for (a) narrower gap ( $L = 37.5\text{km}$ ), (b) a wider gap ( $L = 150\text{km}$ ), (c) a narrower ridge ( $A = 75\text{km}$ ) and (d) a wider ridge ( $A = 300\text{km}$ ).

reveals the importance of the meridional Rossby number  $Ro^y = U/A \cdot f$ , which is a dimensionless measure of the width  $A$  of the ridge. If the air in the gap is decoupled from the westerly basic-state flow and if an air parcel is driven by the external geostrophic pressure gradient force  $-1/\rho \cdot \partial p/\partial y = f \cdot U$ , simple Lagrangian arguments imply that the air parcel stays in the gap for a time period of  $t \sim O(\sqrt{A/Uf})$ , reaching a maximum meridional velocity of  $v_{max}/U \sim O(\sqrt{Af/U})$ . The experiments with doubled and halved ridge width  $A$ , as well as the experiments with modified upstream velocity (see next subsection) conform well with the above scaling rule, provided the gap flow is decoupled from aloft.

Consistent with the arguments given in section 4, increasing the width (and thus slope) of the Alpine ridge also implies an increase in the wavelength of the topographic waves (and vice versa), as can be noted in the lower two panels of Fig.8.

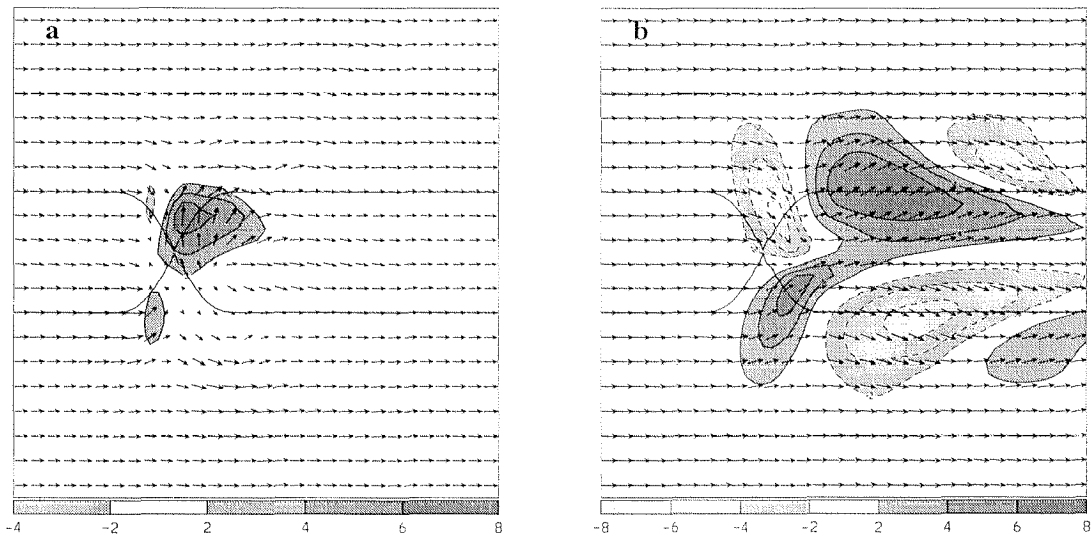


Figure 9. As Fig.5b, but with an upstream velocity of (a)  $5\text{m/s}$  and (b)  $20\text{m/s}$ .

## 5.2 Sensitivity to upstream flow speed

Here the sensitivity with respect to the upstream flow speed is addressed. Two associated numerical experiments are shown in Fig.9, where we have modified the upstream flow speed to  $5\text{m/s}$  and  $20\text{m/s}$ , respectively. The results illustrate that the pressure difference across the ridge cannot be taken as the sole control parameter. While the reduced geostrophic wind velocity (and thus pressure contrast) in Fig.9a indeed reduces the southerly flow as compared to Fig.5b, a further increase of the wind velocity (cf. Fig.9b) does not foster an amplification of the flow response. In contrast, Fig.9b has the characteristics of the linear solution (cf. Fig.4) and lacks a southerly flow across the gap. The absence of the nonlinear response is consistent with the reduced dimensionless mountain height. Partially it might also relate to the increased overall Rossby numbers in the case with  $20\text{m/s}$ , implying that the “symmetry breaking” Coriolis force loses its importance (but see also the following section).

The foregoing experiments demonstrate that a strong meridional pressure difference  $\Delta p$  across the ridge is not a sufficient condition for the occurrence of a southerly wind across a gap transect. This is an interesting observation since many of the operationally used Foehn-forecasting rules in the Alps primarily rely upon  $\Delta p$  (see introduction). Our results suggest that it might in practice be useful to include as a local measure of the dimensionless mountain height the additional parameter  $N/U$  into the underlying shallow Foehn statistics. Here  $N$  and  $U$  denote some measure of the stratification below crest height, and of the easterly unperturbed wind velocity (say, at the  $700\text{ hPa}$  level), respectively. If the  $N/U$  parameter is large enough, the strength of the southerly flow scales approximately with  $\Delta p$  while for small  $N/U$  shallow Foehn is absent irrespective of  $\Delta p$ . In practice however – in particular for deep and narrow valleys such as in the Alps – it might also be that the flow is always within the nonlinear regime, such that consideration of  $\Delta p$  is sufficient.

Finally we note that in the case with smaller upstream velocity the topographic waves



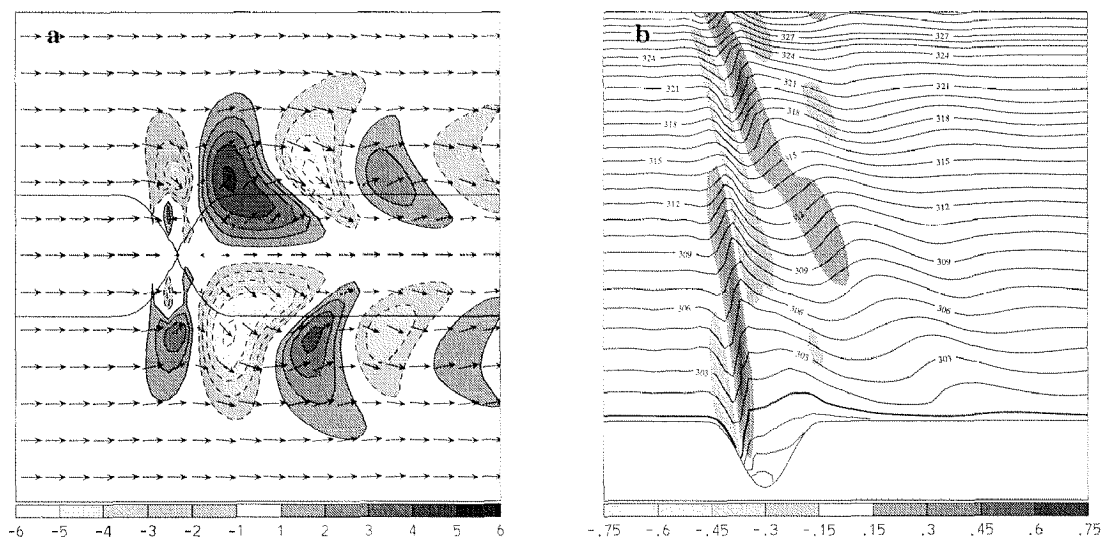


Figure 10. As Fig.5, but with vanishing Coriolis parameter ( $f = 0$ ).

downstream of the gap disappear. In general an increase of the ridge slope (see above), an increase of the stratification (see section 8) and a decrease of the upstream velocity (this section) inhibit the topographic waves. We believe that this behaviour relates to the different strengths of the flow-separation and flow-splitting in the vicinity of the gap.

## 6 Multiple flow solutions for $f = 0$

### 6.1 Sensitivity of standard nonlinear solution for $f \rightarrow 0$

Here we study the sensitivity of the standard nonlinear experiment in Fig.5 with respect to background rotation. From the rules of hydrostatic scaling, this can also be taken as the sensitivity of the hydrostatic flow with respect to the overall horizontal scale of the obstacle. We begin our analysis with a numerical experiment where the background rotation is switched off. If the Coriolis parameter is set to  $f = 0$ , the flow problem has perfect south/north symmetry with respect to the ridge axes. The associated numerical results (Fig.10) confirm this expectation. The gravity wave signature in the section running along the ridge (Fig.10a) is very similar as the one of the standard experiment (Fig.5a), yet the symmetry now precludes any flow through the gap. Rather, the near surface flow solution in Fig.10b is forced to look much alike the linear solution (Fig.4b), and shows the trapped gravity modes earlier discussed in section 3.

Intuitively one would expect that – as a function of the Coriolis parameter – a continuous and smooth transition exists between the rotating flow solution (Fig.5) and the nonrotating limit (Fig.10), i.e. that the steady-state flow fields converge with decreasing Coriolis parameter  $f$  towards the symmetric  $f = 0$  state. However, numerical experiments show that this is – surprisingly – not the case. A systematic set of numerical experiments was conducted with the values of  $f/f_0 = 1, 1/3, 1/6$  and

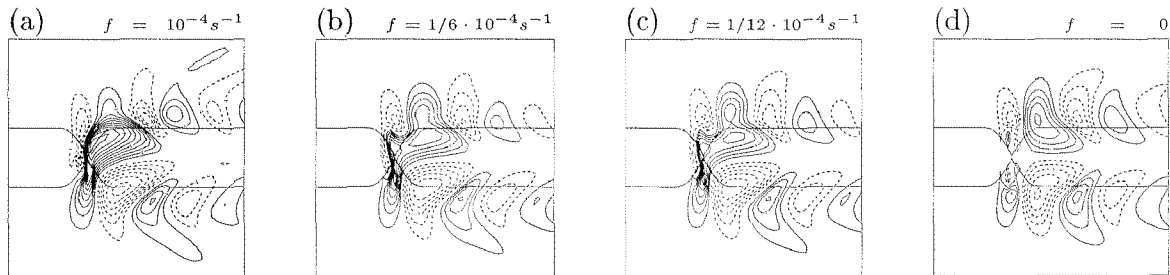


Figure 11. Steady-state meridional wind for standard experiments with  $f \rightarrow 0$ . Note that the flow does *not* converge towards the  $f = 0$  solution shown in Fig. 10a.

$1/12$ , where  $f_0 = 10^{-4} \text{s}^{-1}$ . All experiments were run up to time  $t=60\text{h}$ , whereupon a well-defined steady state is obtained. A selection of the results is displayed in Fig.11, in terms of the southwards flow component on the lowermost model level. The results demonstrate that the limit for  $f \rightarrow 0$  does not converge towards the  $f = 0$  state. Note for instance that there is an almost negligible change between the  $f = 1/6 f_0$  and  $f = 1/12 f_0$  experiments. Despite the weak rotational effects, there is a pronounced southerly flow across the gap, much unlike the symmetric  $f = 0$  state shown in Fig.11d. An additional experiment with  $f/f_0 = -1/12$  was also conducted to test the symmetry of the numerical code, and indeed has produced the same solution as that shown in Fig.11c except for a change in sign. Therefore, we hypothesize that the flow problem in absence of rotation ( $f = 0$ ) has multiple solutions: a symmetric one (which we have seen in Fig.10) and two asymmetric ones (which are obtained in the limits  $f \rightarrow 0^+$  and  $f \rightarrow 0^-$ ). Thus, several questions emerge: Do the asymmetric states also exist in the absence of rotation? Are they stable with respect to small-amplitude perturbations? Is it possible to induce a transition from one solution to another, i.e. what is the stability of the flow solutions with respect to finite-amplitude perturbations? These issues are addressed in the following subsections.

## 6.2 Existence and stability of multiple solutions for $f = 0$

To test whether an asymmetric state can indeed exist in the nonrotating limit, the model is run with  $f = 0$  but initialized with a flow-solution derived from the  $f/f_0 = 1/12$  experiment by removing the geostrophic pressure gradient associated with the mean flow. The initial flow field has a southerly component across the gap as in Fig.11c. The purpose of the experiment is to test whether this asymmetry is able to persist within the symmetric nonrotating dynamical framework. The integration was carried out for 96h with a horizontal resolution of  $\Delta x = 5.6\text{km}$  and clearly demonstrates the stability of the asymmetric flow solution, even in the nonrotating framework.

The stability of the symmetric state was tested by a similar 96h long integration, and the flow was found to be perfectly stable at a resolution of  $\Delta x = 5.6\text{km}$ .

Both the symmetric and asymmetric flow solutions can be classified as wake flows since they contain nonzero potential vorticity (PV). The PV is generated by dissipative processes associated with the flow separation on the upstream side of the gap and gravity wave breaking over the gap region, similar as in the numerical experiments of flow past isolated topography (Schär and Durran 1997). To the extent that

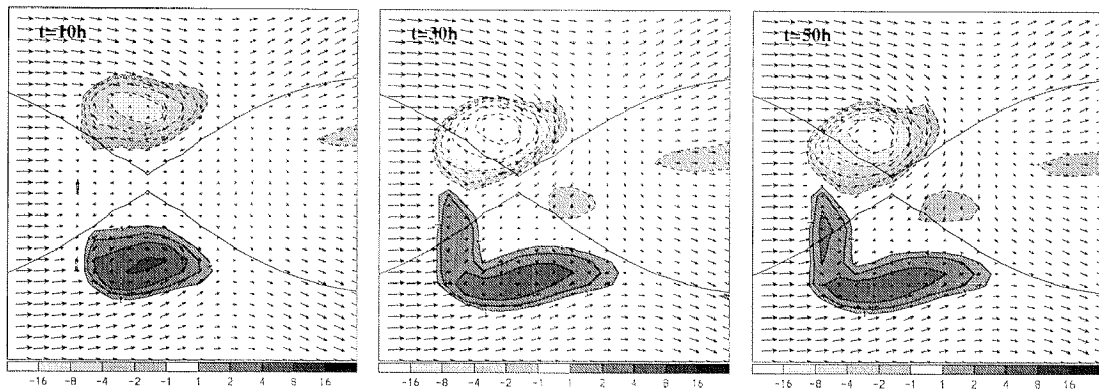


Figure 12. Decay of symmetric solution in a high-resolution experiment. The panels show PV and wind vectors at the second model level (about 200m above ground) at times  $t = 10h, 30h, 50h$  (from left to right).

the stability of wake flows also depends upon the Reynolds number (Batchelor 1967) and thus upon the numerical resolution employed, the stability analysis described above does not guarantee stability of the flows at higher resolutions (or Reynolds numbers). We have thus repeated the stability experiments described above with an increased resolution of  $\Delta x = 2.8km$ . As initial and lateral boundary conditions the steady fields of the  $5.6km$  runs were used. In the case of the *asymmetric* state we find that the flow is stable, but in the corresponding run with the *symmetric* state the initially symmetric flow decays into the asymmetric one due to a wake-instability. In stratified flows such instabilities are due to the presence of anomalies of potential vorticity in wake region, and are associated with barotropic energy conversions (Schär and Smith 1993; Schär and Durran 1997). Further details on the decay of the symmetric solution at high resolution are thus analysed in terms of the low-level distribution of PV. At early times in the simulation (Fig.12a), the positive and negative PV anomalies, which result from the flow separation at the eastern edge of the gap, show excellent north/south-symmetry. The vortices are stationary (no vortex shedding) for two reasons: First, the induced flow field of each vortex helps the other to withstand the westerly basic state flow. Second, the vortices are partly sheltered from the upstream flow by the topography. During the transition to the asymmetric state (Fig.12b) the symmetric negative PV anomaly in the north intensifies whereas the southern positive PV anomaly weakens. This is accompanied by a shift of the whole PV-dipole towards south. Again, in terms of vortex-dynamics, we speculate that now the intensified northern vortex can be held stationary by a weaker southern vortex because its closer position to the pass increases the sheltering effect. In contrast, the southern vortex now feels more strongly the westerly basic state flow. So it needs an intensified northern vortex to maintain its position.

In our particular numerical experiment the southerly solution results, but this is by mere coincidence and depends upon minor asymmetries (such as rounding errors) in the initial fields. A schematic picture of the PV-pattern corresponding with the three different flow solutions is depicted in Fig.13.

In summary, while traditional wake instabilities in homogeneous flows past blunt bodies (Batchelor 1967; Hannemann and Oertel 1989), in shallow-water dynamics (Schär

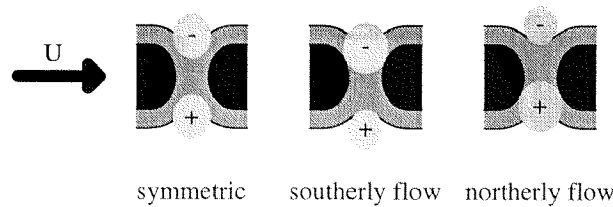


Figure 13. Schematics of low-level PV distributions for the three multiple flow solutions.

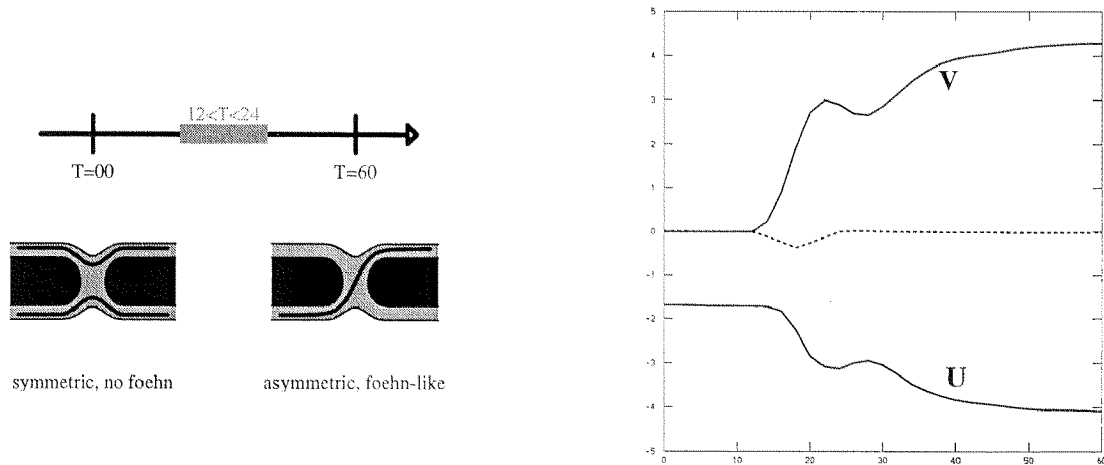


Figure 14. Externally induced transition from the symmetric to the southerly flow solution in a low-resolution experiment. The right-hand panel shows the time-trace of wind components at the gap. The dotted curve is a time trace of the implied pressure contrast.

and Smith 1993), and in stratified flows past isolated smooth topography (Schär and Durran 1997) yield either vortex shedding or a transition into a turbulent flow regime, the initially symmetric flow along a ridge transected by a gap can decay and settle down in the asymmetric stationary flow. From the behaviour of the individual vortices there is some evidence that vortex shedding is here suppressed by the sheltering effect of the underlying gap topography. The instability process thus provides a satisfactory explanation for the nature of the detected multiple flow solutions.

### 6.3 Externally induced transition between multiple flow solutions

When multiple solutions of a nonlinear problem are stable with respect to small-amplitude perturbations, it is still likely that finite-amplitude perturbations are able to promote a transition between the different flow solutions. To test this hypothesis several experiments were conducted at a resolution of  $\Delta x = \Delta y = 5.6 km$ . With this resolution, all the three multiple solutions are stable with respect to small-amplitude perturbations (see previous subsection). Here we describe an experiment where a transition from the symmetric to the southerly asymmetric flow solution is induced. Note that in a high-resolution run with  $\Delta x = \Delta y = 2.8 km$  this experiment would be meaningless since the symmetric solution is unstable (see previous subsection).

The experiment starts with the symmetric state at time  $t = 0$  and is integrated over  $t = 48h$ . Between  $t = 12h$  and  $t = 24h$  a northward directed pressure gradient is applied. The forcing starts at time  $t = 12h$ , increases linearly from zero within the

next  $6h$  to its peak value, and then decreases again until it vanishes at time  $t = 24$  (see dashed curve in Fig.14b). The peak value of the pressure gradient at time  $t = 18h$  is given by  $(\partial\phi/\partial y)_p = -0.0167m/km$  where  $\phi$  denotes the geopotential height. The pressure forcing is applied through the lateral boundary fields. Results in terms of the time traces of the wind components at the gap are shown by the full lines in Fig.14b. These show that the transient forcing indeed promotes a permanent transition into the asymmetric flow state.

Similar experiments were carried out to test the transition from the southerly to the northerly flow regime, and from the southerly to the symmetric one. The former of the two experiments was successful, while we were unable to find a suitable forcing that enabled the transition from an asymmetric into the symmetric regime. This is probably indicative of the weak stability of the symmetric solution with respect to finite amplitude perturbations.

Other transitions studied included an experiment where the upstream velocity was linearly increased during  $24h$  from  $U = 10m/s$  to  $30m/s$ , using the asymmetric flow solution as initial condition. The increase in upstream velocity reduces the nonlinearity parameter  $\hat{\Delta}H = N \cdot \Delta H/U$ . As to be expected a transition into the symmetric flow solution did occur, at a time when the upstream velocity had a value of about  $U = 15m/s$ .

## 7 More realistic Foehn-like settings

The previously considered experiments were highly idealized and have omitted many of the typical characteristics of e.g. Alpine shallow Foehn events. In the following subsection we present additional results where consideration is given in turn to the impact of (7.1) deep valleys leading to a gap-like pass, (7.2) surface friction and (7.3) the presence of an inversion to the south of the ridge. All these aspects give rise to additional interesting flow features, yet – since the parameter space spanned by these additional environmental settings is very large – our presentation restricts attention to a few selected simulations. Unless stated otherwise, the simulations follow as close as possible the standard setting of the nonlinear experiments earlier presented in section 5.

### 7.1 Impact of deep valleys leading up to the gap-like pass

In section 5.1 it was shown that the width of the ridge has a major impact upon the southerly winds through the gap. However, the utilized topography did prescribe identical widths to both the ridge and gap transects. In contrast, the real Alpine topography is characterized by deep valleys which intrude from north and south into the Alpine ridge and join at major Alpine passes. In reality, the width of the gap transect is thus much narrower than the ridge itself. This might be relevant for the flow dynamics since short gap transects reduce the importance of rotational effects and might thus be more susceptible to gravity-wave propagation.

To test this hypothesis we use an alternate topographic configuration shown in Fig.3b. Here the parameter  $\beta$  in equation (4) is set to 0.5. The gap has the same north/south width as in the standard case (cf. Fig.5), while the ridge has the same width as in the wide ridge case (cf. Fig.8d). Keeping the meridional width of the gap as in the standard case ensures that the length scale for the meridional gravity waves in the

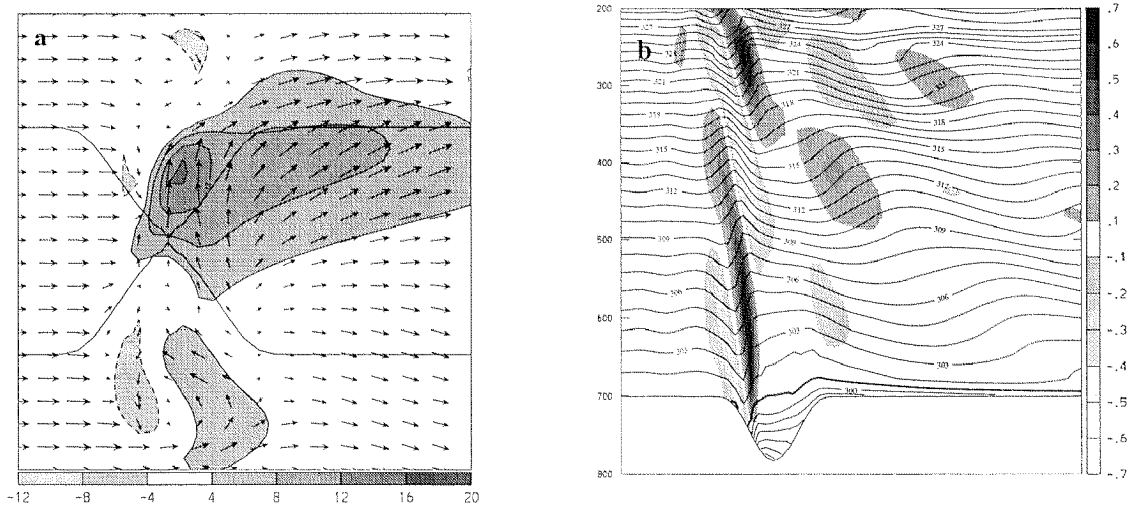


Figure 15. As Fig.5, but with valleys north and south of the gap. The width of the ridge is as in Fig.8d.

gap is unchanged. Increasing the width of the ridge on the other hand implies a larger cross-ridge pressure contrast, and is thus conducive to stronger acceleration on the gap transect. Results are shown in Fig.15 and demonstrate the importance of the valleys. From the three settings considered, Fig.15a reveals the strongest southerly flow with values up to  $\sim 18m/s$ , compared to  $\sim 10m/s$  and  $\sim 13m/s$  in Fig.5 and 8d, respectively. A narrow gap also concentrates the southerly wind into the center of the gap transect. The isentropes do only marginally penetrate into the gap (Fig.15b), and the signature of flow separation and lee vortex to the south-west of the gap are much stronger, and a somewhat weaker vortex now appears to the north-east of the gap. The air in the gap is well decoupled from the flow aloft. Furthermore, as compared to the case in Fig.8d, the southerly wind maximum is displaced further north, consistent with the reduced rotational effects upon gravity wave propagation. Rotational effects suppress gravity wave propagation, and the wider the gap, the more symmetric is the wind distribution. The optimal geometry for shallow Foehn is thus one with a wide mountain ridge (which induces a strong pressure contrast) and a narrow gap width (which allows strong gravity wave effects).

## 7.2 Impact of surface friction

To study the effects of surface friction, several additional experiments were conducted using a full surface layer formulation (Louis, 1979) representing a no-slip lower boundary condition. To this end, the roughness length for the whole domain was set to a constant value of  $g \cdot z_0 = 0.1m^2s^{-2}$ , a value that corresponds to arable land. The surface fluxes of heat were set to zero in these experiments. Otherwise the setting is as in the standard nonlinear case earlier discussed in section 4.

The inclusion of surface friction invalidates the analytical solution of the basic state uniform flow. Since an analytical solution including the effects of surface friction is no longer available, we used a one-way nesting technique to obtain the background

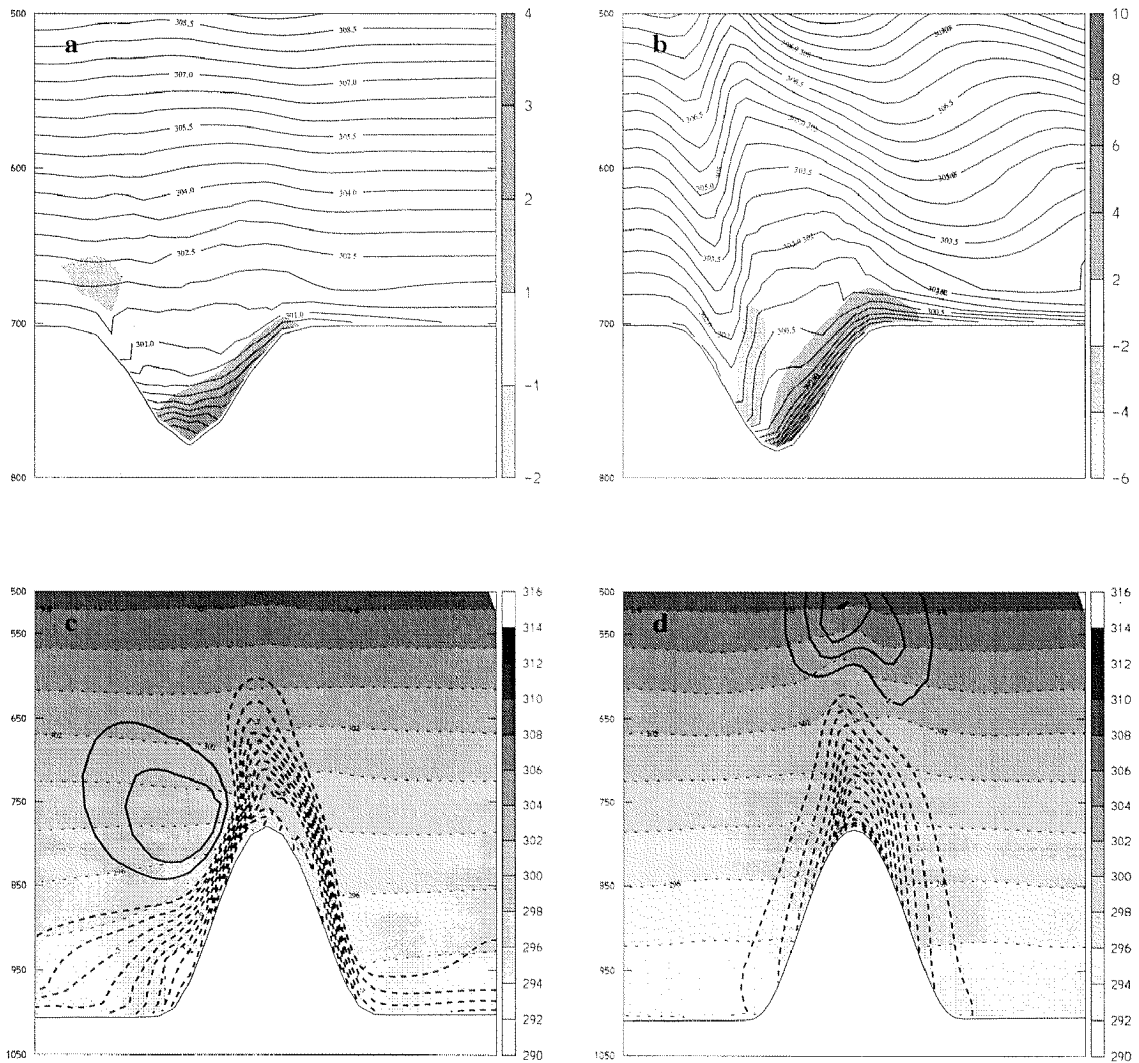


Figure 16. Comparison of the flow with surface friction (left) and without surface-friction (right). Top panels (a, b) show an west/east vertical section with potential temperature (solid lines) and meridional wind velocity (shaded). Bottom panels (c, d) show a north/south-section with potential temperature and deviations from the upstream zonal velocity  $U = 10 \text{ m/s}$  (contour interval is  $1 \text{ m/s}$ , negative contours are dashed).

flow fields in the presence of a two-dimensional ridge. To this end, we specify at the boundaries of the outer domain (resolution  $\Delta x = \Delta y = 11.2 \text{ km}$ , domain size  $N_x = 121$ ,  $N_y = 81$  gridpoints) a uniform flow and stratification, whereupon a well-defined boundary layer structure develops, which includes at low levels a near-neutral stratification and some northwards Ekman flow. The steady-state structure of this boundary layer flow is then used to drive the simulation in the inner nest (resolution  $\Delta x = \Delta y = 5.6 \text{ km}$ , domain size  $N_x = 121$ ,  $N_y = 81$  gridpoints).

Comparison of the solutions is shown in Fig.16, with no-slip and free-slip solutions on the left and right, respectively. The top panels show that – even with surface friction included – the southerly winds through the gap persist, although they are substantially weaker than in the case with a free slip lower boundary condition. The

isentropes in a west/east-section also reveal striking differences in the strength of the upper-level gravity wave. In the no-slip case (Fig.16a) the isentropes above the ridge are only slightly displaced from their upstream height and do not penetrate into the gap. Also, the prominent hydraulic jump like feature of the free-slip simulation (Fig.16b) is completely absent, and the southerly winds across the gap have an almost symmetric distribution with respect to the gap axes.

In the lower panels of Fig.16 we display the deviation from the mean zonal along-ridge flow speed ( $U = 10m/s$ ) together with the isentropic distribution in a south/north section running across the gap. In both cases, there is a pronounced deceleration within the gap. However, as indicated by the drastically different flow solution discussed above, the underlying physical mechanisms for the deceleration of the zonal flow are very different. In the free-slip case (Fig.16d) the deceleration is largely associated with the hydraulic jump like feature evident in Fig.16b, while in the no-slip case (Fig.16c) it is dominated by boundary layer processes. The zonal flow shows some asymmetry with respect to the ridge axes, which includes an accelerated jet-like feature to the south, slightly below the height of the ridge line. These features are already present far upstream of the gap and are presumably associated to the inhibition of the Ekman southerly flow across the ridge.

An additional effect of the surface friction is to completely remove the stationary trapped gravity mode identified in the linear simulation. This is not surprising since the gravity wave response is drastically reduced, and since the trapped gravity mode has a shallow vertical structure and is thus susceptible to the damping by surface friction.

All of this shows that the boundary layer actively supports the decoupling of the gap flow from the upper-level westerly flow. For the  $z_0$  values under consideration, surface friction indeed leads to a completely different flow solution where the upper-level flow is almost unaffected by the presence of the gap. While both flow solutions in Fig.16 exhibit a southerly gap flow, the underlying physical mechanisms are thus quite different. In the free-slip flow regime, the flow-response is governed by a deep gravity wave response, while in the no-slip regime it is dominated by a pronounced decoupling of the upper-level flow from the boundary layer. The selection of the flow regimes is likely to depend on a range of parameters, such as the upstream stratification and wind-speed, the underlying  $z_0$  value, and other factors. Additional experiments with increased surface friction (larger  $z_0$ ) showed no qualitative differences to the one presented in Fig.16a,c. For experiments with reduced  $z_0$  values we found that the flow situation approaches the free-slip solution in a continuous way. There is no abrupt transition from a no-slip flow solution to a free-slip solution.

Overall the experiment gives support to previous studies of boundary layer effects in stratified flow past topography (e.g. Miller and Durran 1991; Georgelin et al. 1994) which did find that boundary layer effects can have a major impact upon the strength of the upper-level gravity waves. Our study of these aspects have only covered a small portion of the parameter space, and the resulting effects demonstrate that this is an area which would merit further study.

In the nonrotating limit discussed in the previous section, we found that the flow problem has multiple solutions. Additional experiments in this limit but with surface friction included have indicated that boundary layer processes – at least with the roughness parameter selected – may completely suppress multiple flow solution. Even with strong perturbations we were unable to promote a switch from the sym-



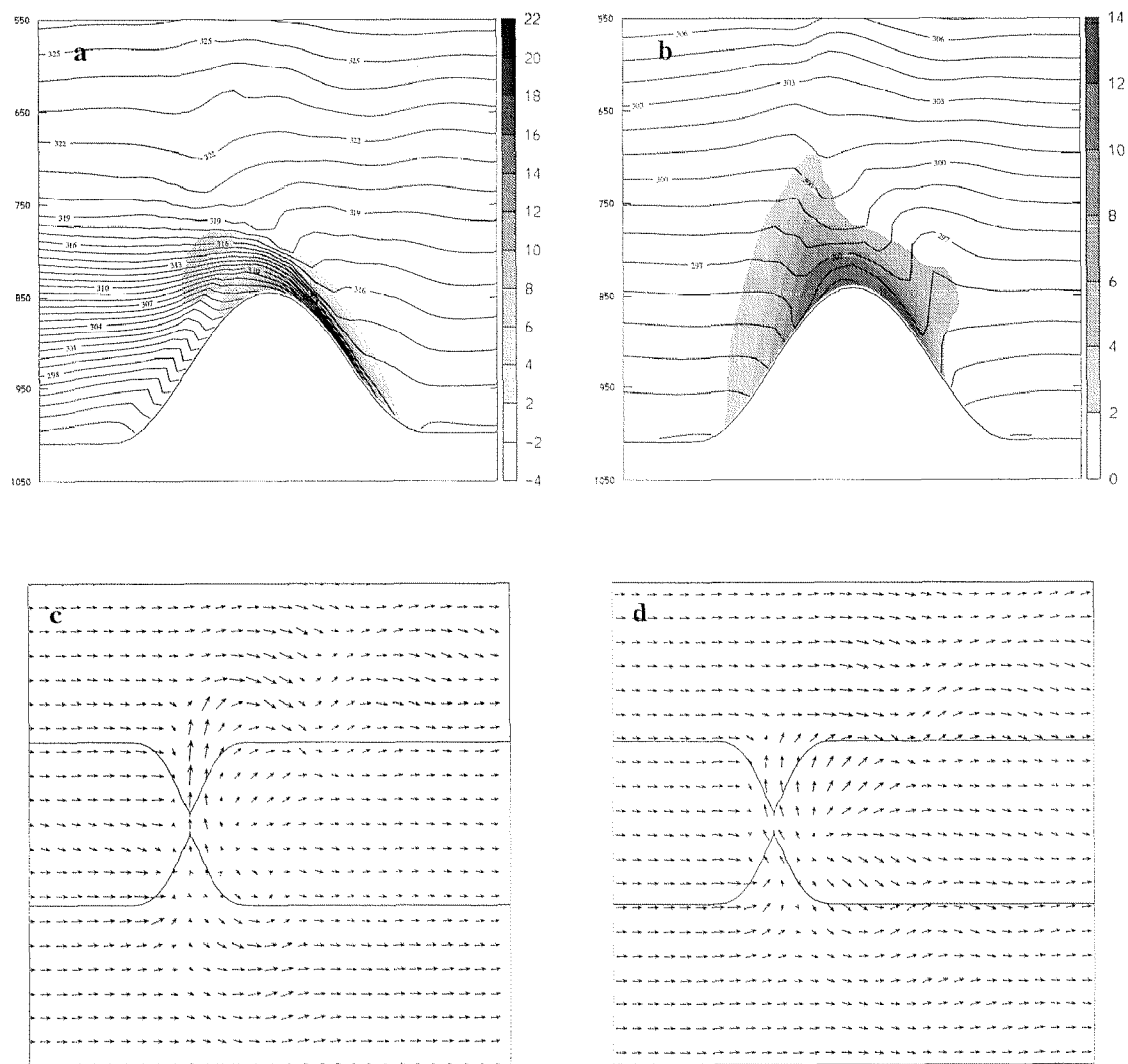


Figure 17. Comparison of standard case (right) with a flow solution characterized by an inversion to the south of the ridge (left). The top panels (a, b) show a north/south vertical section with potential temperature and meridional wind velocity. Bottom panels (c, d) show surface wind vectors.

metric to the asymmetric regime. This is not surprising, since the detailed analysis in the previous section has revealed that the multiple flow solutions do depend upon the presence of gravity waves and flow splitting processes, which are suppressed by boundary layer processes.

### 7.3 Impact of an inversion

The presence of strong inversions to the south of the Alps is a common feature in many observations of deep and shallow south Foehn. The inversion to the south (and its absence to the north) appears to be associated with low-level advection and orographic blocking of cold air, and with diabatic cooling from evaporating precipitation. Depending on the situation, the inversion height may be located below pass height, or

in between the pass and the ridge height. Each of these situations is expected to lead to a particular flow response. Here we give consideration to an idealized setting where the inversion is located in between the pass and the ridge height. Such an inversion at a height of 2000m was for instance noted in the "Alpine Foehn of the century" by Seibert (1985) and Hoinka (1985). These studies also suggest that the inversion to the south supports the blocking of the low-level air in the Po-valley.

To mimic the presence of an inversion to the south of the ridge (above pass, but below ridge height), an idealized two layer atmosphere was specified. Our standard configuration is enhanced by adding a lower more stably stratified layer to the south of the ridge, which is assigned a stratification of  $N = 0.02s^{-1}$ . In the upper layer and to the north of the ridge we specify  $N = 0.01s^{-1}$  as in the previous experiments. In order for the difference to become more clear, we chose a gap depth of 1500m (instead of the standard case with 900m), yielding a pass height of 1500m. The inversion itself is located at a height of 2500m, i.e. 1000m above the gap saddle point. Since the ridge has a height of 3000m, the imbalance below 2500m between northern and southern side is "blocked" except near the gap. Only in the gap-region a strong density-driven current can occur.

Quasi-steady results using the free-slip lower boundary condition are shown after 80h integration time in Fig.17. Results with and without the presence of an inversion to the south are displayed in the left-hand and right-hand panels, respectively. The top panels show how the southerly flow across the gap is heavily intensified by the presence of the inversion, resulting in a pronounced downslope wind storm with wind speeds up to 22m/s (compare Fig.17a with 17b). Also, the jet of southerly winds now extends much farther towards the north (Fig.17c). The strong gap wind of the inversion case are in accord with the increased meridional pressure gradient, and the whole flow is now reminiscent to a "flowing off" as in the hydraulic theory. As a result, there is also a net warming near the gap exit, which results from the adiabatic warming of air parcels which descend from near the inversion level. Such a warming (and drying) is a very common feature of Foehn observations in the Alps. For the simulations in the previous sections, however, it is only marginally present, since airparcels that reach the lee slope of the gap originate from similar levels upstream.

The overall dynamics of the flow still appears comparable to the standard nonlinear case discussed in section 5, except for the gravity-driven enhancement resulting from the mass imbalance on the two sides of the obstacle. For instance, the hydraulic jump like feature on the western flank of the gap is present in all simulations, and there is a clear indication of flow separation and flow splitting upstream and downstream of the gap (not shown). Note also the absence of steepened or overturned gravity waves in the south/north sections of Fig.17a,b, a feature which is presumably related to the presence of critical levels for wave vectors oriented towards northerly directions.

Additional experiments were conducted for slightly different configurations. One case studied includes – in addition to an inversion to the south – a low-level cold-air pool to the north. As to be expected, the presence of this pool retards the northward progression of the warm Foehn-like gap flow. In yet another case consideration was given to a two-layer structure with a step increase in stratification at a height of 3500m. This configuration produced interesting interactions of gravity waves with the stratification profile, and appears to hinder flow-splitting in the lower layer.

## 8 Concluding remarks

This study was motivated by the frequent occurrence of shallow Foehn in the Alpine region. In contrast to deep Foehn cases, the cross-Alpine southerly flow in shallow Foehn cases is essentially confined to the valley transects, whereas the mid-tropospheric flow can have a westerly or even a north-westerly direction. Here consideration was given to an idealized model problem: The flow of a rotating stratified stream of air along a two-dimensional ridge transected by a gap.

With intermediate Rossby-numbers and a sufficiently deep gap, the flow within the gap decouples from the flow aloft and is driven by the geostrophic pressure gradient along the gap axes to yield a Foehn-like flow. The associated dynamics is heavily affected by gravity wave propagation, critical levels, non-linear effects, and there is also some evidence that a transition to supercritical-like flow may occur. Factors that increase the strength of the pressure-driven flow across the gap include an optimal scaling of the ridge width (wide enough to feel the rotational effects, narrow enough to allow gravity wave propagation), a deep gap to force the decoupling from the upper-level flow, and an inversion to the south of the Alpine-like topography which in effect increases the pressure gradient.

Of particular interest is the demonstration that the limit  $f \rightarrow 0$  is singular, i.e. the flow solution does not converge towards the symmetric  $f = 0$  solution. Rather there exist multiple stationary solutions for  $f = 0$  (two with northerly and southerly flow across the gap, respectively, and one with north/south symmetry). The existence of these multiple steady states was related to a wake instability, yet vortex shedding is suppressed by the presence of the ridge downstream of the gap. Their occurrence is of substantial conceptual and practical interest. To our knowledge it is the first demonstration that such multiple steady states can exist in simple mountain flow problems. It also appears possible that the sudden onset and decay of shallow south Foehn may be related to the transition between multiple flow solutions, for instance when triggered by slow changes in the larger-scale flow. The current analysis of multiple steady states restricts attention to nonrotating flow with a free slip lower boundary condition, but it is possible that similar multiple states may also exist in a more general framework.

The flow across the gap shows several of the characteristics of typical shallow Alpine south Foehn events. The realism of the solutions is further increased when an inversion on the righthand flank of the ridge (looking along the ridge in the upper-level flow direction) was included. Such an inversion over the Po valley is often observed in Alpine Foehn cases. The overall flow structure is highly complex, and shows several hydraulic-jump-like features. One such jump may occur on the gap axes downstream of the mountain pass (see Fig.17b). Yet another one may occur in the along-ridge direction at the western flank of the gap (see Fig.16b), and it appears to support the decoupling the near surface southerly flow through the valley transect from the westerly flow aloft. At lower levels there is clear evidence for flow-separation and flow-splitting effects. Gravity wave activity is responsible for a strong amplification of the imposed pressure gradient across the gap.

The direct applicability of the model problem to shallow Alpine south Foehn is clearly limited by its simplicity. In particular, sensitivity studies conducted in section 7 demonstrate that beside rotational effects, shallow Foehn is sensitive to surface friction and to details in the stratification profile. Additional factors which might need

consideration include moist dynamics as well as a fully three-dimensional forcing (e.g. by a confined southerly flow ahead of an approaching cold front). Furthermore, the current study is limited to hydrostatic dynamics and thus not applicable to narrow gaps with horizontal scales below a few kilometers. Despite these limitations, the adoption of an idealized flow configuration has served to reveal some of the basic dynamic properties of rotational flow past a gap, a flow problem which is very common in our atmosphere.



# PART C

# LINEARIZED FLOW OVER ISOLATED OROGRAPHY: THE INFLUENCE OF ROTATION <sup>1</sup>

MICHAEL SPRENGER,<sup>2</sup> RENÉ FEHLMANN, HUW DAVIES and CHRISTOPH SCHÄR

## Summary

In an influential diagram Smith (1989) determined the critical mountain heights for flow splitting and for wave breaking. The flow situation in this study is analog to Smith's: a uniform flow with constant upstream velocity  $U = 10\text{m/s}$  and constant stratification  $N = 10^{-2}\text{s}^{-1}$  impinging on a witch-of-agnesi mountain of along-stream width  $a$  and normal-to-flow width  $b$ . In contrast to Smith's study we include the Earth's rotation by assuming a typical midlatitude value of  $10^{-4}\text{s}^{-1}$  for the Coriolis parameter  $f$ .

The influence of the Coriolis force is measured by the along-flow Rossby number  $Ro^x = U/af$  and the normal-to-flow Rossby number  $Ro^y = U/bf = Ro^x/r$ , where  $r$  denotes the aspect-ratio  $b/a$  of the mountain. We determined *linear* estimates for the critical mountain heights for stagnation near the surface upstream and downstream of the mountain, for the stagnation aloft and for the intersection of isentropic surfaces with the lower boundary.

The results for an axisymmetric mountain ( $r = 1$ ) are as follows: For large Rossby numbers,  $Ro^x \gg 1$ , the height for upstream stagnation *decreases* with *increasing* Rossby number. In contrast, it *decreases* with *decreasing* Rossby number in the low Rossby number limit ( $Ro^x \ll 1$ ). In an intermediate range ( $Ro^x \approx 1$ ) the critical height for stagnation to the lee of the mountain is smaller than the one for stagnation on the windward side. The stagnation of the flow above the mountain decreases with increasing Rossby number, which is in agreement with the stronger gravity-wave activity for larger Rossby numbers. The smallest critical mountain heights result from the intersection of the streamlines with the topography except in the quasigeostrophic limit where the critical mountain height for upstream stagnation is smaller.

For elliptical mountains ( $r \neq 1$ ) two extreme regimes exist: ridge-like mountains ( $r > 1$ ) and narrow mountains ( $r < 1$ ). In the weakly rotating case ( $Ro \gg 1$ ) the critical mountain heights for upstream stagnation conform with Smith's result:  $H(\text{ridge-like}) < H(\text{elongated})$ . In the quasigeostrophic limit, on the other hand,  $H(\text{ridge-like}) > H(\text{elongated})$  prevails. Furthermore, the intersection of the isentropes with the surface yields the strongest limitation on the applicability of the linear theory.

*Nonlinear* simulations were further used to check the validity of the above *linear* estimates. Generally, the linear model overestimates the critical heights, and the dependency on the aspect-ratio  $r$  appears far less pronounced in the nonlinear results than in the linear ones. In the quasigeostrophic limit the upstream stagnation seems to be related to the formation of a Taylor cap like feature.

---

<sup>1</sup>to be submitted to *Tellus*

<sup>2</sup>Corresponding author: Swiss Federal Institute of Technology, GI-ETH, Winterthurerstr. 190, CH-8057 Zürich, Switzerland, e-mail: sprenger@geo.umnw.ethz.ch

## 1 Introduction

Nonlinearities are responsible for the most interesting dynamical features of the atmosphere. Often, the flow characteristics can only be understood by means of such nonlinear processes. The origin of the nonlinearities might be directly inherent in the air masses, as it is the case with cyclogenesis, or it might be indirectly “forced” by external parameters. As such an external parameter act high mountains (Smith 1979, Binder and Schär 1995). Many nonlinear phenomena associated to mountains gained a lot of interest in the past: flow splitting on the windward side (Smith 1989, Smith and Gronas 1993), the formation of quasi-stationary lee vortices (Smith and Grubisic 1993, Schär and Smith 1993a), the transition to a von Karman vortex street (see e.g. Schär and Durran 1997, Sun and Chern 1994, Schär and Smith 1993b), the breaking of gravity waves (Smith 1977, Bacmeister 1993) and upstream blocking (Pierrehumbert and Wyman 1985).

Due to their great influence on the flow, it is most important to know under what atmospheric and orographic situations these phenomena occur. Different approaches were used in the past: observational studies (see e.g. Mayr and McKee 1995), nonlinear numerical models with highly idealized atmospheric and orographic settings (Smith and Gronas 1993, Bauer 1997, Clark and Peltier 1984, Schär and Durran 1997) and analytical models, which primarily rely on linear theory (Smith 1979, 1989). The advantage of the latter two strategies is that they allow to prescribe a well-defined parameter space, whereas the first strategy cannot be renounced at due to its direct applicability to reality. Since nonlinear simulations are very resource demanding, many regime diagrams were gained by mean of linear “quasi-analytical” methods. Smith (1989) used linear theory to subdivide the parameter space into regions with flow splitting and wave breaking. In another study Smith (1988) included the collapse of density surfaces. Of course, these results must be taken with some caution. *Linear* models will never be able to correctly predict *nonlinear* phenomena. But they can, nevertheless, yield some qualitative dependences on mountain shapes and other parameters. Furthermore, Smith deduced from his studies some physical insight regarding the mechanisms which lead to flow splitting and wave breaking.

In this study, we use a linear model to subdivide the parameter space into regions where linear theory might be appropriate to use. In addition to the parameters chosen by Smith (1989) (aspect ratio and height of the mountain), we include the *Coriolis force* and the angle of attack of the impinging flow. Following Smith, we focus on three phenomena: near-surface stagnation, stagnation aloft and collapse of isentropic surfaces. We will also compare these results with nonlinear simulations although not in a systematic way. This will allow us to see whether the results of the linear theory are applicable, if not quantitatively, at least qualitatively.

Smith (1989) discussed only the nonrotating case. But from theoretical considerations rotation can be expected to be of some importance for the flow past mountains with horizontal scales larger than about  $50km$ . In fact, the influence of the Coriolis force was shown in many studies. Pierrehumbert and Wyman (1985) looked at upstream blocking, Chen and Smith (1987) studied the blocking and deflection of the airflow by the Alps, Smith (1982) deduced expressions for the change in atmospheric fields in the weakly rotating case and Olafsson and Bougeault (1997) showed that gravity-wave drag reacts sensitively to rotation.

The outline of the paper is as follows. We will first describe the idealized flow problem.



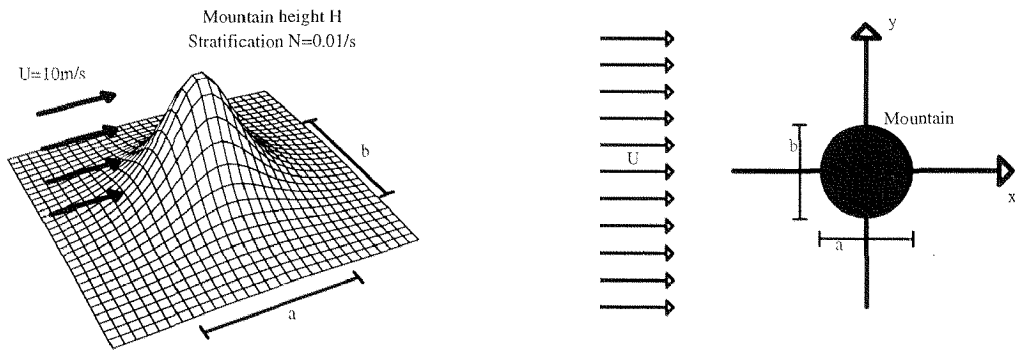


Figure 1. Model problem: isolated orography of height  $H$  and horizontal half-widths  $a$  and  $b$ , uniform upstream flow with velocity  $U = 10\text{m/s}$  and stratification  $N = 10^{-2}\text{s}^{-1}$ .

Strongly connected with that, we then present some details of the linear theory and the nonlinear numerical model used. Subsequently, we discuss the main results of this work, the applicability of the linear theory both for an axisymmetric mountain, and for arbitrary elliptical mountains. Finally, in the conclusion, we compare the linear results with the nonlinear results.

## 2 Problem Description, Linear Theory and Numerical Model

In this section we first present the idealized model problem and then discuss some numerical details. It will become evident that some of the numerical parameters have also an influence on the critical mountain heights which will be obtained in the following sections. Therefore we also present at this point a discussion on the sensitivity of the results to the numerical parameters.

### 2.1 Problem Description

The flow problem is depicted in Fig.1. A uniform basic state flow is impinging on an isolated mountain. The basic state flow is characterized by a constant velocity  $U = 10\text{m/s}$  and a uniform stratification  $N = 10^{-2}\text{s}^{-1}$  (Brunt-Väisällä frequency). Whereas the basic state flow is kept fixed during the whole series of experiments, the mountain shape, its horizontal extension and orientation varies from experiment to experiment. But we concentrate on one family of mountains which can be parametrized by

$$h(x, y) = \frac{H}{[1 + (x/a)^2 + (y/b)^2]^{3/2}} \quad (1)$$

$H$  determines the mountain height,  $a$  and  $b$  its horizontal extensions. This witch-of-agnesi profile for the mountain was also chosen by Smith (1989). Thus, in choosing this profile, we are able to compare our results with his, wherever possible. With the inclusion of the Coriolis parameter  $f$ , the parameter space of the flow problem is 6-dimensional:  $U, N, f, a, b, H$ . As mentioned before, the basic state defined by  $U,$

$N$  and  $f$  will be kept fixed at typical midlatitude values:  $U = 10\text{m/s}$ ,  $N = 10^{-2}\text{s}^{-1}$  and  $f = 10^{-4}\text{s}^{-1}$ , so that the resulting parameter space becomes 3-dimensional.

For the following discussion it is more insightful to use some dimensionless numbers instead of the remaining three dimensional length scales  $a$ ,  $b$  and  $H$ . We use:

$$Ro = \frac{U}{a \cdot f} \quad \hat{H} = \frac{N \cdot H}{U} \quad r = b/a \quad (2)$$

The along-stream Rossby number  $Ro$  measures the importance of rotational effects and the ratio  $r$  determines the shape of the mountain ( $r > 1$  corresponding to broad ridge-like mountains and  $r < 1$  corresponding to narrow elongated mountains). The dimensionless mountain height  $\hat{H}$  is the square ratio of the available kinetic energy in the flow ( $1/2 \cdot U^2$ ) and the potential energy needed to surmount the mountain ( $1/2 \cdot NH^2$ ). From this energy argument one expects a flow over the mountain for  $NH/U < 1$  and flow around it otherwise (Sheppard 1956). We will see that the linear theory only partly agrees with this expectation! In principle, we should also include the dimensionless parameter  $Na/U$ . This parameter measures the non-hydrostatic effects of the flow. We restrict ourselves to horizontal scales  $a > 10\text{km}$ . This yields  $Na/U > 10$  for the values of  $N$  and  $U$  prescribed above. Therefore, no large non-hydrostatic effects can be expected.

## 2.2 Linear Theory

The linearized equations of motion take the following form in the Boussinesq approximation (Lüthi 1994):

$$\begin{aligned} L(u') - f \cdot v' &= -(p'/\rho_0)_x \\ L(v') + f \cdot u' &= -(p'/\rho_0)_y \\ L(w') &= -(p'/\rho_0)_z + b' \quad \text{with buoyancy} \quad b' = g \cdot \Theta'/\Theta_0 \\ u'_x + v'_y + w'_z &= 0 \\ L(b') + N^2 \cdot w' &= 0 \end{aligned} \quad (3)$$

where  $L$  denotes the operator  $L = U \cdot \partial/\partial x + \epsilon$ . The first term of  $L$  denotes advection and the second term dissipation. From its definition it might be anticipated that a disturbance will decay downstream on a length scale of  $1/\epsilon \cdot U$ . At the upper model lid, a radiation condition is applied, such that no energy can be back reflected. Furthermore, we used free slip boundary conditions at the bottom.

The great advantage of the above linear model is that the flow behaviour can be understood by means of gravity waves. Since this is of some importance for the further work, we quote here some main results (see e.g. Durran 1990, Gill 1982). If we assume a periodic mountainous landscape of the form  $\eta(x, y) = H \cdot \exp[i \cdot (kx + ly)]$ , we can solve the flow problem analytically. We decompose the perturbations according to  $\phi' = \phi^* \cdot \exp\{i \cdot (kx + ly + nz)\}$  ( $\phi = u', v', p', w', b'$ ). Then we can express the vertical wave number  $n$  by means of the horizontal wave numbers  $k, l$  (if we assume  $\epsilon = 0$  at this point for convenience),

$$n^2 = n^2(k, l) = \left(\frac{N}{f}\right)^2 \cdot \frac{1 - S^2}{Ro^2 - 1} \cdot K^2 \quad \text{with} \quad K^2 = k^2 + l^2 \quad (4)$$

where  $Ro = U \cdot k/f$  measures the importance of rotational effects and  $S = U \cdot k/N = f/N \cdot Ro$  is a measure of non-hydrostatic effects. We see that vertically propagating gravity waves ( $n^2 > 0$ ) occur in an intermediate range  $N/U > k > f/U$  of zonal wavenumbers  $k$ . For other along-flow wavenumbers  $k$  the disturbances decay exponentially in the vertical. Furthermore, at  $S = Uk/N = 1$  and  $Ro = Uk/f = 1$  we get singularities. These singularities mark a qualitative transition in the flow solution.

The flow solution for an isolated mountain  $\eta(x, y)$  can be obtained by means of a Fourier decomposition (Lüthi 1994). We decompose the mountain into its Fourier components. For each component we know the solution. We superpose these solutions to get the final flow. According to the above discussion, the predominant wave numbers in the spectrum of the mountain will determine the qualitative behaviour of the flow. If, for instance, the horizontal extension of the mountain is of order  $a$ , the Fourier components of order  $2\pi/a$  will be most important in the spectrum of the mountain, and thus dominate the flow behaviour.

The Fourier decomposition is performed by a program developed by Lüthi (1994). The number of Fourier components in the decomposition of the mountain were chosen to be  $N_x = 2048$  in flow direction and  $N_y = 512$  normal to the flow direction. A test revealed good convergence of the results with those numbers. If  $N_x, N_y$  were halved, the results remained the same in a 5%-range. Since we are interested in accurate estimates of special flow points, we chose a high resolution of  $D_x = D_y = 0.1$ , i.e. the half-width  $a$  of the mountain is resolved by  $1/D_x = 10$  grid points. Increasing the resolution by a factor of two ( $D_x = D_y = 0.05$ ) only led to minor changes of the results. The coefficient of dissipative damping  $\epsilon$  was kept at the constant value of  $\epsilon = 0.0000015s^{-1}$ . This corresponds to a time  $1/\epsilon (\approx 7d)$  during which the atmosphere relaxates. The dissipation might partly reflect physical processes, and partly it is introduced for numerical reasons. Since the discrete Fourier decomposition assumes periodic lateral boundary conditions, any disturbance downstream of the mountain will also appear upstream. The damping guarantees that no disturbance remains at the downstream lateral boundary.

### 2.3 Nonlinear Simulations

At some places in this study we will also compare the results of the linear theory with the results of a nonlinear model. We used the Europa Modell (EM) of the German and Swiss weather service (Majewski 1991 and Majewski and Schrodin 1994). The EM is well established both in numerical weather prediction and idealized numerical studies. For our experiments we used a slightly modified form of the code which allows an f-plane approximation. Furthermore, we used free slip at the lower boundary and a KDB-type gravity-wave absorber at the upper boundary (Klemp and Durran 1983, Bougeault 1983, Herzog 1995). The only parametrization package employed is a turbulence formulation with a second-order closure scheme of hierarchy level 2 (Mellor and Yamada 1974, Müller 1981). Consistent with the free-slip lower boundary condition, the vertical turbulent fluxes of heat and momentum are set to zero near the surface. We used in the horizontal  $N_x = 121, N_y = 81$  grid points. In the vertical, 34 hybrid levels were used, with somewhat increased level density near the surface in order to better resolve near-surface processes. The horizontal resolution was varied according to the horizontal extension of the mountain. We had about 8 grid points to resolve one half-width  $a$  of the mountain. Lüthi (personal communication) found that for reasonable results, three grid points would even be enough. The timestep

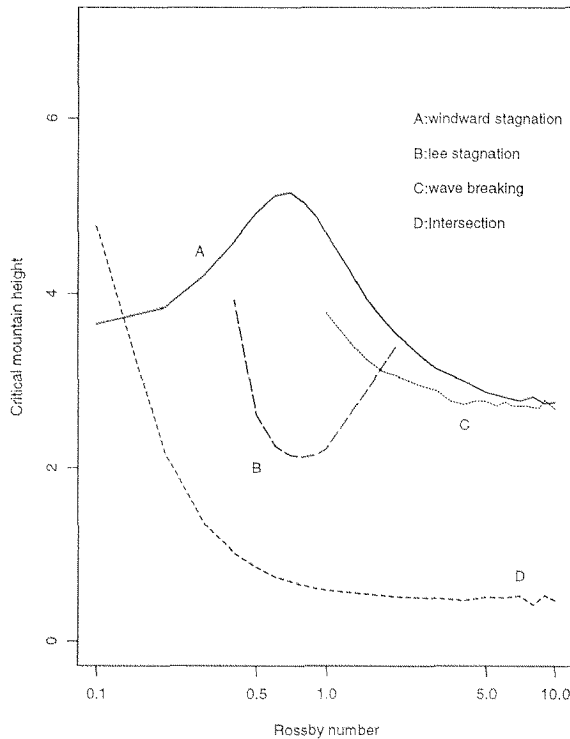


Figure 2. Regime diagram for axisymmetric mountain. Critical dimensionless mountain heights for (A) upstream near-surface stagnation, (B) downstream near-surface stagnation, (C) stagnation aloft, and (D) intersection of isentropes with the ground are shown as a function of the along-flow Rossby number  $Ro = U/af$ .

$\Delta t$  was adapted according to the Friedrichs-Courant-Levi criterion in order to ensure numerical stability. The integration time was 60 hours or more, which guaranteed good convergence. When lee vortices occurred, we obtained good convergence on the windward side. The basic state was chosen to be the same as in the linear model experiments. The lateral boundary values were kept constant during the whole simulation and “communicated” to the interior by means of a Davies relaxation scheme (Davies 1976).

### 3 Axisymmetric Mountain

In this section we study the different mechanisms which can limit the applicability of the linear theory for an axisymmetric mountain. We specifically look at the stagnation of the near-surface flow on the windward side (a) and in the lee (b) of the mountain. Then, we concentrate on the stagnation of the flow in the free atmosphere, i.e. above the mountain (c), and finally we look at the intersection of the streamlines with the topography (d). Our aim is to gain a regime diagram which tells us at what mountain heights these phenomena—according to the linear theory—occur. These critical heights might then give a hint for the mountain heights at which flow splitting and blocking (a), downstream stagnation (b), wave breaking (c) and streamline collapse (d) occur in “reality”, i.e. when the full nonlinear dynamics is considered.

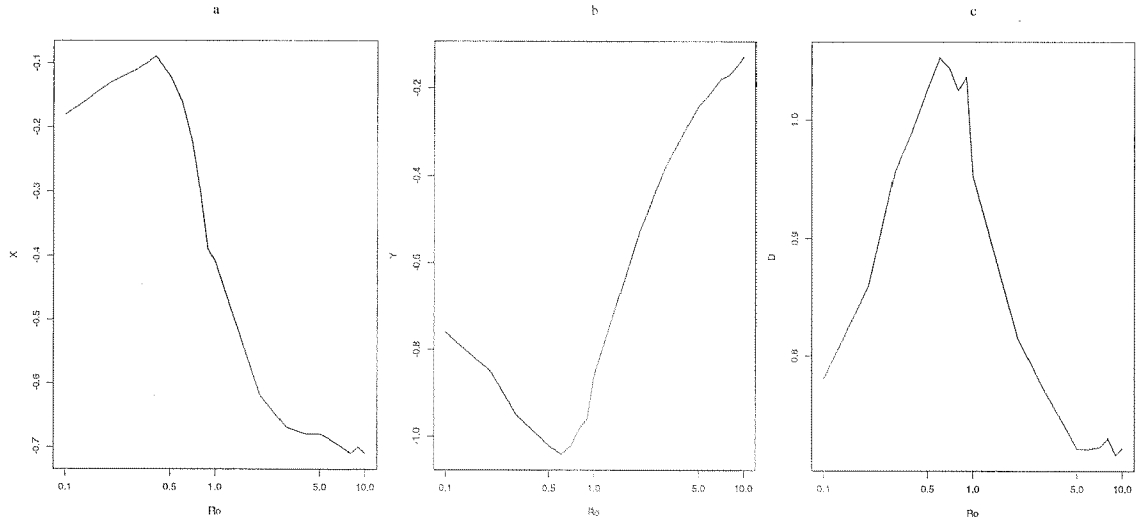


Figure 3. Position of the upstream stagnation point as a function of the Rossby number  $Ro = U/af$ . X- and Y-coordinates of the stagnation point in units of half-width  $a$  of the mountain (a and b) and distance of the stagnation point from the mountain axis (c).

### 3.1 Upstream Stagnation

Two questions are of special interest with respect to upstream stagnation. At what mountain height occurs the transition from flow over to flow around the mountain? Where will the flow split? Linear estimates for these quantities are obtained as follows: We choose a fixed mountain height of 100m. The perturbation surface wind  $(u', v')$  for this mountain height results from the Fourier decomposition, as described in section 2.2. We then determine the curve where  $v' = 0$ . On this curve  $u'$  is minimized (negative values!). If the mountain height is increased, the curve  $v' = 0$  keeps its form and  $u'_{min}$  scales linearly with the height due to the linearity of the model. Therefore, a critical mountain height can be determined at which the perturbation wind  $u'$  exactly “opposes” the basic state flow  $U$ , resulting in vanishing zonal velocity. Together with the vanishing meridional velocity  $v'$ , the location and the critical mountain height for a stagnation point is found. The results are depicted in Fig.2 (curve A) and in Fig.3.

For large Rossby numbers ( $Ro \gg 1$ ), the critical mountain height *decreases* with *increasing* Rossby number. This can be understood by gravity wave activity. In fact, for small-scale mountains ( $U/f \gg a \gg U/N$ ) the vertical propagation of gravity waves induces an upstream/downstream-asymmetry (see Fig.4 right). On the windward side, the flow decelerates and in the lee the flow accelerates. Evidently, the stronger the deceleration of the upstream flow, the smaller the critical mountain height for upstream stagnation. Since this upstream/downstream-asymmetry becomes more pronounced with increasing Rossby number, the deceleration becomes stronger and thus the critical mountain height smaller.

Interestingly, this behaviour does *not* continue into the small Rossby number limit. In contrast to the above discussed nonrotating limit ( $Ro \gg 1$ ), the critical mountain height *increases* with *increasing* Rossby number in the quasigeostrophic limit ( $Ro \ll 1$ ) (Fig.2 curve A). In order to understand this behaviour it is worthwhile to take a closer look at the flow fields in these two limits (Fig.4). Obviously the flow fields

change qualitatively in the transition  $Ro = 0.1 \rightarrow 1 \rightarrow 10$ . In the quasigeostrophic limit ( $Ro = 0.1$ ), the upstream/downstream-asymmetry vanishes (Fig.4d). This follows from the dispersion relation (4), which states that no “symmetry breaking” gravity waves propagate vertically in the quasigeostrophic limit. Orographically induced disturbances decay exponentially in the vertical. Furthermore, a clear mountain anticyclone can be discerned (Fig.4a). From this observation one might expect that the stagnation point moves to the south as the Rossby number is decreased. In contrast, the stagnation point should lie on the along-flow symmetry axis of the mountain in the nonrotating limit ( $Ro \gg 1$ ), since no symmetry-breaking Coriolis force is present. The X- and Y- coordinates of the numerically determined stagnation points fulfill these expectations (Fig.3a,b). For large Rossby numbers ( $Ro \gg 1$ ) the Y-coordinate is nearly 0, i.e. the stagnation point near the along-stream symmetry axis. In contrast, for small Rossby numbers ( $Ro \ll 1$ ) the stagnation point has large negative values of Y, i.e. it lies far to the south. Furthermore, in the limit of small Rossby numbers the stagnation point lies near the north/south symmetry axis of the mountain (small values for X in Fig.3a). This is in agreement with the quasigeostrophic prediction by Schär and Davies (1988). It is this change of the position of the stagnation point which must be responsible for the unexpected behaviour of the critical mountain height with respect to changes in the Rossby number.

If the Rossby number is large ( $Ro \gg 1$ ), the stagnation point lies near the center of the windward side of the mountain. The prediction of the linear model for upstream stagnation might therefore correspond to upstream blocking and flow splitting in the nonlinear case. The air will move sideways around the mountain with splitting at the stagnation point. It is, however, not so clear what stagnation means in the quasigeostrophic limit  $Ro \ll 1$ . Here, the stagnation point lies not on the upstream side of the mountain, but on its southern side near the north/south symmetry axis. It was found analytically by Schär and Davies (1988) that the occurrence of such a stagnation point might correspond to a Taylor cap. Part of the air just above the mountain is then decoupled from the background flow and remains approximately at rest.

In order to judge the prediction of the linear model we also performed some simulations with the nonlinear model. With a Rossby number of  $Ro = 1$  we should obtain flow splitting at a dimensionless mountain height of  $NH/U = 4.67$  according to the linear theory. The prediction of the nonlinear model is  $1.5 < NH/U < 1.625$ . Therefore, the linear theory considerably overestimates the critical mountain height. This is in agreement with the observation of Smith (1989), who found the same for the nonrotating limit ( $Ro = \infty$ , note that Smith introduces a factor  $1/2$  for the mountain heights. So, a mountain height of 2 in our simulations corresponds to one of 1 in Smith’s simulation). Furthermore, the linear model predicts the stagnation to occur at  $x/a = -0.36$  and  $y/a = -0.8$ , whereas the nonlinear model yields  $x/a = -0.45$  and  $y/a = -0.33$ . The stagnation point does not lie so far to the south as predicted by linear theory. We will discuss these differences further in the conclusions.

It is most interesting that we were also able to see the development of a Taylor cap by means of nonlinear simulations. The analytical solution by Schär and Davies (1988) predicts the occurrence of a Taylor cap at a nondimensional mountain height of  $NH/U = 3\sqrt{3}/2 \approx 2.6$ . In the nonlinear simulations we found the development of a nearly motionless air mass just above the mountain in the transition from dimensionless mountain height 2 to 2.6 (Fig.5). The surface winds show the typical anticyclonic

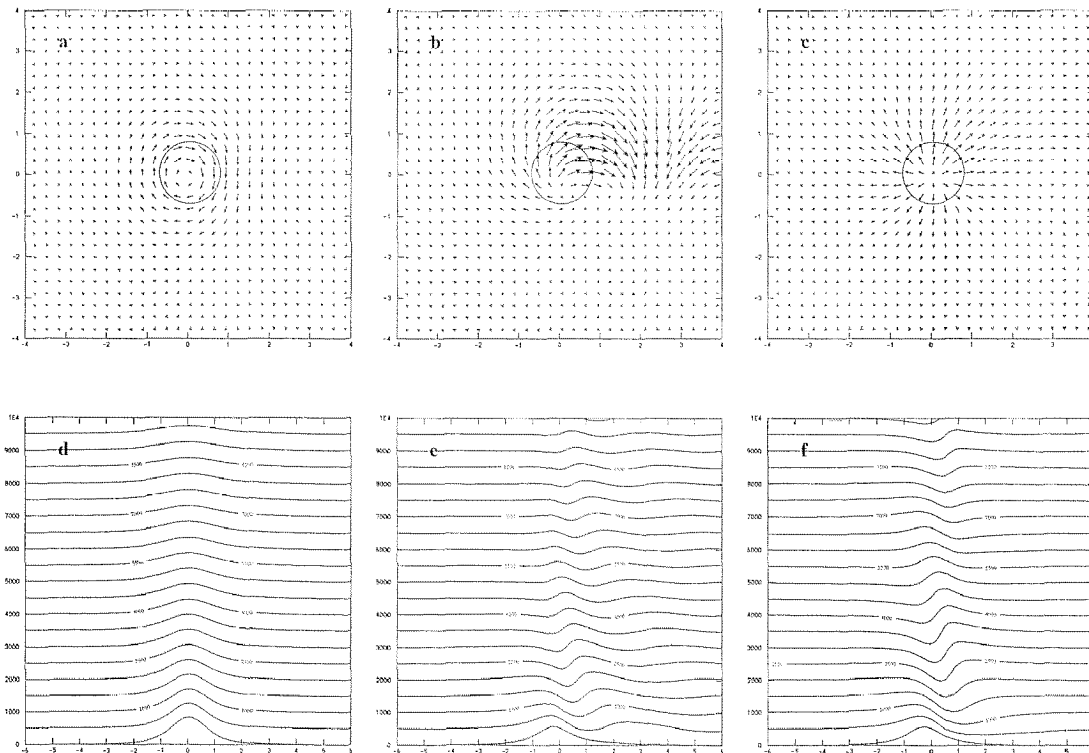


Figure 4. Linear flow response for  $Ro = 0.1$  (left),  $Ro = 1$  (middle) and  $Ro = 10$  (right). Upper panel: surface wind disturbances ( $u', v'$ ), lower panel: streamlines (isentropes) in a vertical section through the center of the mountain in flow direction.

movement of the the quasigeostrophic behaviour. In the lee, a well-pronounced trough develops, as it was already reported by Peng et al. (1995). In Fig.5a the mountain height is 2000m and no flow decoupling (Taylor cap) is discernible. For the mountain of height 2600m (Fig.5b) the region with wind speed less than  $2m/s$  (dashed line) is quite extended and marks off a Taylor cap like feature.

### 3.2 Downstream Stagnation

In the previous subsection we looked at the stagnation of the near-surface flow on the *windward* side of the mountain. Here we focus on the near-surface stagnation *downstream* of the mountain. In fact, in an intermediate range of Rossby numbers ( $2 > Ro > 0.5$ , approximately) surface waves appear downstream of the mountain (Fig. 6). They have their origin in the transition from ( $Ro > 1$ ) to ( $Ro < 1$ ). We stressed in the section 2.2 how a singularity occurs at critical wavenumbers  $k$  which satisfy  $k \cdot U/f = 1$ . For a mountain with a half-width  $a$ , such that  $Ro = U/af = 1$ , these critical wave numbers will not be negligible in the Fourier decomposition of the mountain. If we express the wavelength  $\lambda$  which corresponds to the critical wave number  $k = f/U$  in units of the half-width  $a$  of the mountain, we get:

$$\frac{\lambda}{a} = 2\pi \cdot \frac{U}{a \cdot f} = 2\pi \cdot Ro \quad (5)$$

For  $Ro = 0.5$  we get  $\lambda/a \approx 3.1$  and for  $Ro = 2$  we get  $\lambda/a \approx 12.6$ . These values are

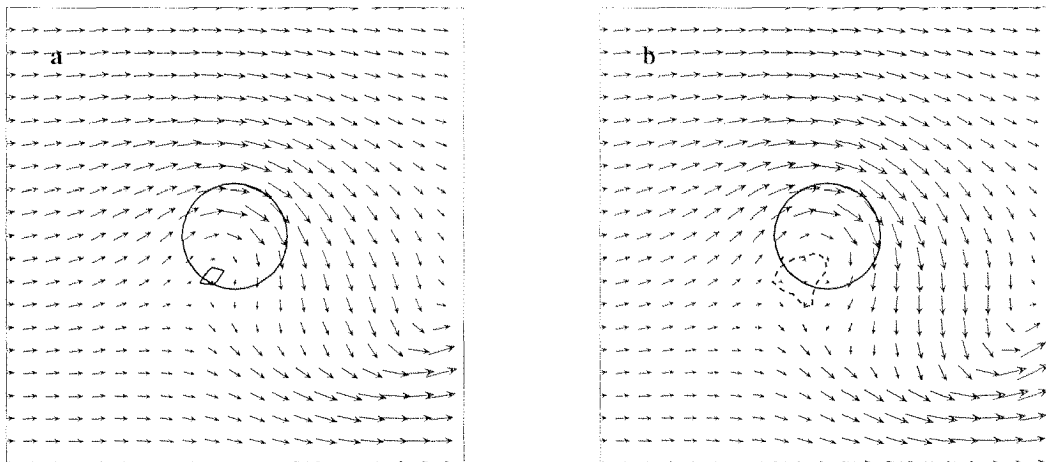


Figure 5. Nonlinear simulation for  $Ro = 0.1$  and non-dimensional mountain heights of  $NH/U = 2$  (a) and of  $NH/U = 2.6$  (b). Shown are surface wind vectors, 2m/s-velocity contour (dashed) and the half-width contour of the mountain (solid). On the right a Taylor cap may be discerned.

in good agreement with the numerical results (Fig.6 and Fig.7). These so-called low-level near-inertial waves were already found in other studies (see for example Trüb and Davies 1994 or Bauer 1997).

The intensity of the downstream waves scale with the mountain height due to the linearity of the model. Therefore, we can obtain a critical mountain height for downstream stagnation with the same method as for upstream stagnation. We find that the critical dimensionless mountain height at which the flow will stagnate depends strongly on the Rossby number (Fig.2 curve B). This could be expected from the above argument. The interesting fact is that the critical height becomes *smaller* for this downstream stagnation than for the previously discussed upstream stagnation in an intermediate range of Rossby numbers (compare curves A and B in Fig.2). Therefore, the limitations of the linear model arise from downstream stagnation instead of upstream stagnation for these intermediate Rossby numbers. The qualitative form of the curve can be understood by the following argument. The surface waves become strongest in an intermediate range of Rossby numbers ( $Ro \approx 1$ ). Therefore, in this intermediate range the critical mountain height becomes small. Outside this range the amplitude of these lee-waves are small and therefore the associated critical mountain heights large (see e.g. Trüb and Davies 1994).

In nonlinear simulations with a similar flow situation, Trüb (1993) found that these downstream waves persist for high mountains. They occur in this case as well-pronounced humps in the streamlines downstream of the mountain.

Both the stagnation on the windward side and in the lee of the mountain indicate a limitation for the applicability of the linear theory. But one may expect that the windward stagnation with the accompanying flow splitting leads to a much stronger qualitative change in the flow than the humps in the lee of the mountain. Therefore, even if the critical height for downstream stagnation is smaller than the one for upstream stagnation, the latter might be more important for the qualitative behaviour of the whole flow solution.



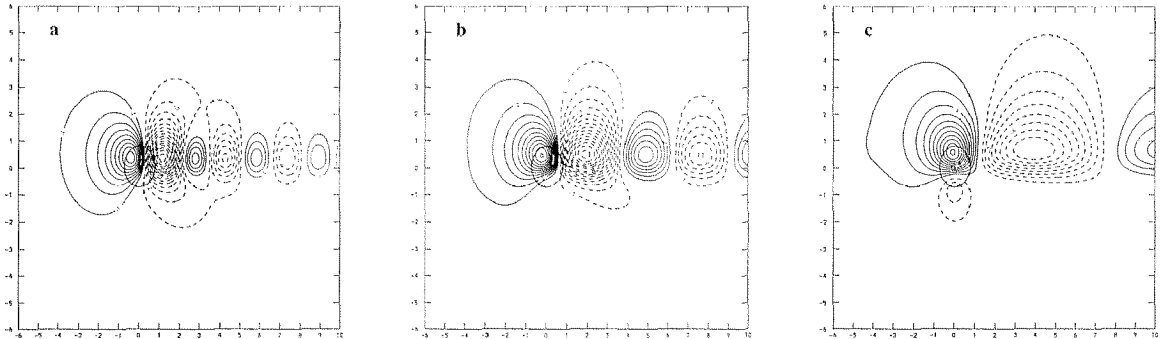


Figure 6. Linear surface waves to the lee of the mountains (north/south wind component).  
(a)  $Ro = 0.5$ , (b)  $Ro = 0.9$ , and (c)  $Ro = 2.0$ .

### 3.3 Upper-Level Flow Reversal and Wave Breaking

Stagnation of the zonal flow in the free atmosphere, i.e. above the mountain, means that the isentropes overturn. The resulting unstable stratification leads to strong turbulent mixing. The situation is somewhat related to the breaking of water waves.

The linear model predicts a critical mountain height for the along-flow stagnation above the mountain (Fig.2 curve C). The procedure to obtain the critical mountain height and the vertical position of the breaking region is as follows. The  $u'$ -field was calculated at 10 levels from  $0m$  to  $10km$  height, resulting in a  $\Delta z$  of  $\approx 1111m$ . The minimum was then evaluated on every level. This level was then taken as the center of a new set of 10 model levels, which now had a  $\Delta z$  tenfold reduced to  $\approx 111m$ . This procedure was repeated one further time. Then, the resulting critical mountain height turned out to be well-determined. But it is somewhat more difficult to locate the vertical position of the flow reversal region very accurately, since the extrema are not clearly defined in the vertical (see Fig.8).

The critical mountain height *decreases* with *increasing* Rossby number. But while the critical mountain height remains more or less constant for large Rossby numbers ( $Ro > 5$ ), it increases considerably near Rossby number 1. The gravity waves which emanate from the mountain (Fig.8) give the explanation for this. They become stronger as the Rossby number increases (compare Fig.8a and 8b). Therefore, the along-flow velocity perturbations become stronger and, in consequence, the critical mountain heights smaller. Furthermore, the gravity waves propagate more steeply with an increasing Rossby number (Fig.8). In fact, for large Rossby numbers the stagnation point lies just above the mountain peak, whereas for smaller Rossby numbers it is located downstream of the mountain (not shown). For small Rossby numbers, the stagnation point even lies downstream, *below* the mountain peak (not shown). Note also that in the quasigeostrophic limit ( $Ro \ll 1$ ) it is not possible to determine a stagnation point above the mountain. In this limit “no” gravity waves emanate from the mountain. The disturbances decay in the vertical, as described by the dispersion relation in section 2.2. Therefore, the regime diagram was not extended to Rossby numbers smaller than 1.

As in the case of near-surface stagnation, the linear model seems to overestimate the critical mountain heights for wave breaking. In a nonlinear simulation with  $Ro = 1$ , we were able to fix the critical mountain height for wave breaking somewhere between

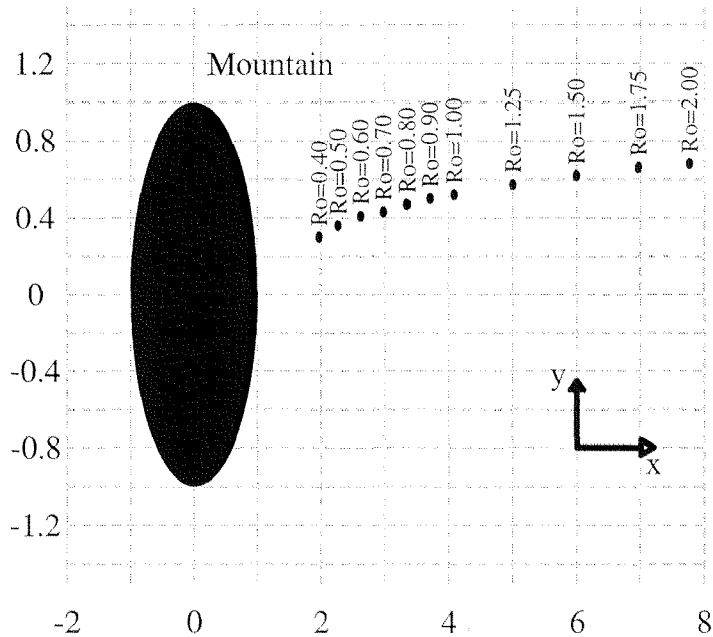


Figure 7. Position of the downstream stagnation point as a function of Rossby number (measured in half-widths  $a$  of the mountain).

$NH/U = 0.75$  and  $NH/U = 1.5$ . Between these two mountain heights the transition to vertical isentropes occur. The linear model, in contrast, predicts a critical height of 4. Therefore, the factor between “linear” and “nonlinear” results is of the same order of magnitude ( $\approx 2.5$ ) as in the case with upstream stagnation. But one should also keep in mind that the nonlinear model used is hydrostatic and therefore not able to directly simulate wave breaking. Therefore, the estimates of the nonlinear model have to be taken with some caution.

It is important which process occurs first: upstream stagnation near the surface (flow splitting) or stagnation in the free atmosphere (wave breaking). If flow splitting occurs first, most of the air moves sideways *around* the mountain. This leads to weaker gravity waves above the mountain, and thus to a reduced tendency for gravity-wave breaking. Similarly, if gravity-wave breaking occurs first, the flow changes qualitatively too. The breaking region works as a source of gravity waves which then “communicate” the disturbance to other flow regions and thus change the flow qualitatively. This will also change the tendency for flow splitting (Smith 1989). The linear model predicts flow splitting at  $NH/U = 4.7$  and wave breaking at  $NH/U \approx 4$ . This order of occurrence is reproduced by the nonlinear simulation (flow splitting:  $1.5 < NH/U < 1.625$ , wave breaking  $0.75 < NH/U < 1.5$ ). Hence, the linear model is able to give the correct order in this case.

### 3.4 Intersection of Isentropes with Lower Boundary

So far we focused on the velocity fields to determine the limitations of the linear model. The critical mountain heights turned out to be larger than  $NH/U = 1$ . But, in fact, the linear model predicts an intersection of streamlines with the lower boundary at much smaller critical mountain heights (Fig.2 curve D). Such an intersection is

not possible if the velocity at the intersection point does not vanish. Therefore, the intersection indicates a limitation of the linear model.

The critical mountain height, at which an intersection of isentropic surfaces occurs, can be deduced as follows. Take two isentropic surfaces which are at level  $z_0$  and  $z_0 + \Delta z$  far upstream, respectively. If  $\eta(x, y; z)$  denotes the vertical displacement at position  $(x, y)$  of the isentropic surface which far upstream is at level  $z$ , the height of these two surfaces will be  $z_0 + \eta(x, y; z_0)$  and  $z_0 + \Delta z + \eta(x, y; z_0 + \Delta z)$  at any position  $(x, y)$ , respectively. The two isentropic surfaces will intersect if

$$z_0 + \eta(x, y; z_0) > z_0 + \Delta z + \eta(x, y; z_0 + \Delta z) \quad (6)$$

This criterion becomes

$$1 + \frac{\partial \eta}{\partial z} > 0 \quad (7)$$

in the limit  $\Delta z \rightarrow 0$ . Since the fraction  $\partial \eta / \partial z$  scales linearly with the mountain height, a critical mountain height at which equality prevails can be determined.

The critical mountain height decreases with increasing Rossby number. Fig.4 gives the explanation to this fact. The vertically propagating gravity waves lead to a pronounced upstream/downstream asymmetry in the large Rossby number limit ( $Ro \gg 1$ ). This means that the isentropes intersect the ground in the lee of the mountain at quite small mountain heights. In contrast, in the quasigeostrophic limit ( $Ro \ll 1$ ) the disturbances decay in the vertical, and therefore the upstream/downstream asymmetry vanishes. This leads to the large increase of the dimensionless mountain height for small Rossby numbers. Furthermore, the position where the isentropes intersect with the ground move from  $x/a = 1.25$  for  $Ro = 10$  to  $x/a = 0$  for  $Ro = 0.1$ , i.e. from a position to the lee of the mountain to the peak of the mountain.

Smith (1988) gives a critical mountain height of  $NH/U = 0.5$  in the nonrotating limit ( $Ro = \infty$ ) for the ‘‘collapse of the density surfaces’’ (in isotheric coordinates). We obtain a value of  $NH/U = 0.47$  for a Rossby number of  $Ro = 10$ . Furthermore, Smith predicts the collapse to occur at  $x/a = 1, y = 0$ , whereas we obtain  $x/a = 1.25, y = 0$ . Therefore, the agreement in this limit is reasonably good.

Note that the critical mountain height for the collapse of the isentropic surfaces is smaller than the critical mountain heights for upstream and downstream stagnation, as well as for stagnation aloft (Fig.2), except at the small Rossby number limit. In this limit the curves for upstream stagnation and isentropic surface collapse intersect.

## 4 Elliptical Mountains

In this section we discuss the influence of the shape of the mountain. We can easily take the shape into account by allowing different values for the zonal ( $a$ ) and meridional ( $b$ ) half-width of the mountain (see equation 1, section 2.1). Thus, we get one further dimensionless parameter  $r = b/a$  which can be changed. Large values  $r > 1$  correspond to broad ridge-like mountains (i.e. flow from north towards the Alps), small values  $r < 1$  to narrow elongated mountains (i.e. flow from west towards the Alps). In the diagrams of this section we keep the half-width  $a$  of the mountain the same, thereby defining the zonal Rossby number  $Ro^x = U/af$ , whereas the meridional half-width  $b$  and the associated meridional Rossby number  $Ro^y = U/bf = 1/r \cdot Ro^x$  varies.

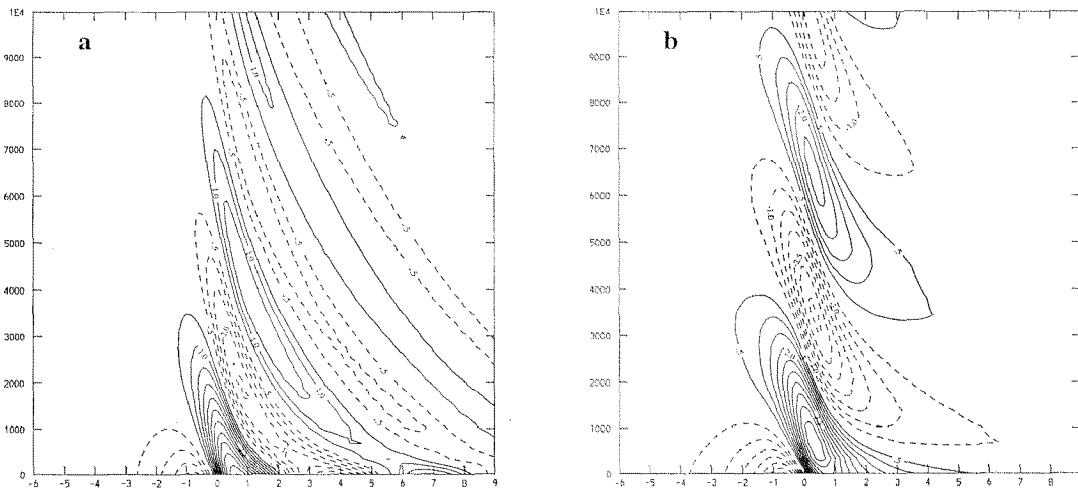


Figure 8. Linear results for zonal wind perturbation  $u'$  emanating from the mountain for  $Ro = 1$  (a) and  $Ro = 5$  (b).

Hence, we obtain a change in the aspect ratio  $r$  and in the meridional Rossby number  $Ro^y$ , while keeping the zonal Rossby number  $Ro^x$  fixed. Depending on the regime in the  $Ro^x/ Ro^y$ -diagram, different approximations might be applied.  $Ro^x \gg 1, Ro^y \gg 1$  marks the non rotating limit,  $Ro^x \ll 1, Ro^y \ll 1$  the quasigeostrophic limit. If only one of the two parameters is small,  $Ro^x \ll 1$  or  $Ro^y \ll 1$ , the semigeostrophic approximation might be used (see e.g. Davies and Horn 1988).

In the following we will discuss the different phenomena, as in the axisymmetric case. In addition, we will also discuss the influence of the angle  $\alpha$  of the approaching flow in subsection (e). This might be insightful to understand the flow characteristics if the approaching flow toward the Alps (for example!) turns from north to west or vice versa.

#### 4.1 Upstream Stagnation

The critical dimensionless mountain height for upstream stagnation reacts very sensitively to the aspect ratio  $r$  of the mountain (Fig.9). The procedure for finding the stagnation point is the same as in section 3.1. For large Rossby numbers  $Ro^x \gg 1$ , the critical mountain height shows the behaviour that Smith found for the nonrotating case. The height  $NH/U$  increases with decreasing aspect ratio  $r$ . But in the quasigeostrophic limit ( $Ro^x \ll 1$ ) the height decreases with decreasing aspect ratio  $r$ . Furthermore, we find that for broad, ridge-like mountains (large values  $r$ ) and intermediate Rossby numbers, very large critical mountain heights emerge (up to  $NH/U = 14$ !).

The unexpected behaviour of the critical mountain height might become clearer if the location of the stagnation point is taken into account (Fig.10). For  $Ro^x = 6$  and  $Ro^x = 0.2$  the X-coordinate (measured in half-widths  $a$  of the mountain) remains approximately the same for all aspect ratios  $r$ , whereas the coordinate changes for the intermediate value  $Ro^x = 1$  (Fig.10 left). A look at the corresponding Y-coordinate

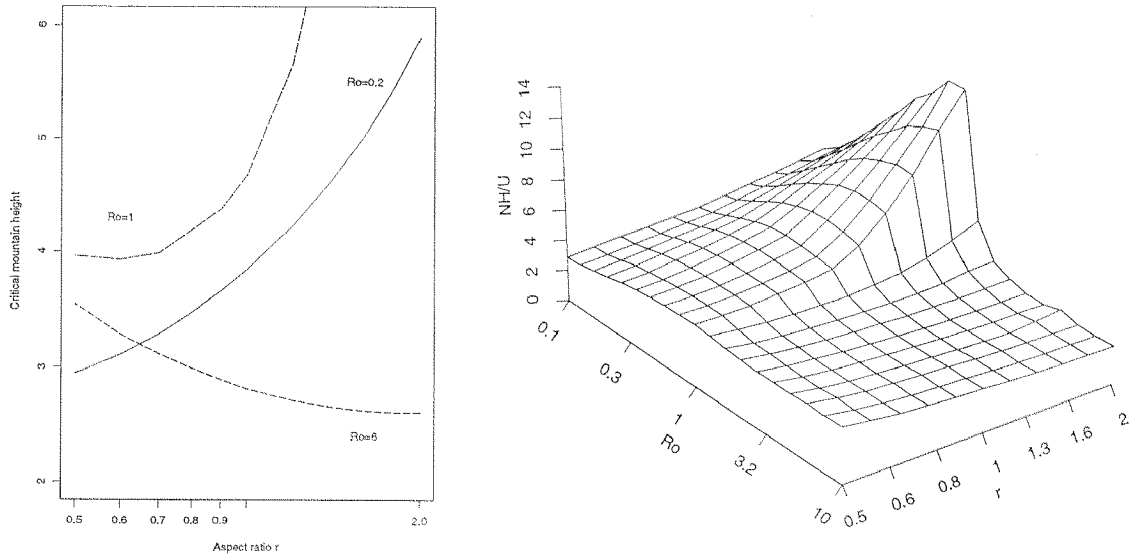


Figure 9. Critical dimensionless mountain height for upstream stagnation as a function of  $r$  and  $Ro^x$ . Left: selected Rossby numbers, Right:  $r/Ro$ -diagram (The grid points correspond to values  $r = 0.5, 0.6, 0.7, 0.8, 0.9, 1, 1.2, 1.4, 1.6, 1.8, 2$  and  $Ro = 0.1, 0.2, 0.3, 0.4, 0.5, 0.6, 0.7, 0.8, 0.9, 1, 2, 3, 4, 5, 6, 7, 8, 9, 10$ )

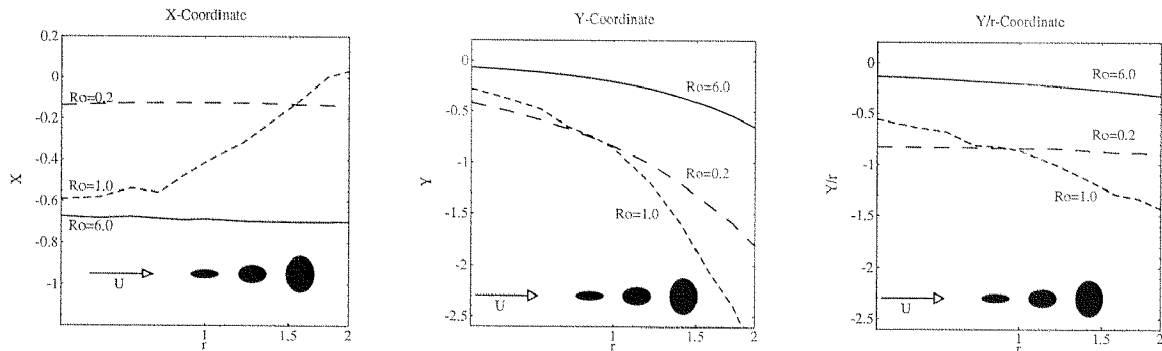


Figure 10. Location of the upstream stagnation point for  $Ro = 6$ ,  $Ro = 1$  and  $Ro = 0.2$ , depending on the aspect-ratio  $r$  of the mountain. From left to right: X-coordinate, Y-coordinate,  $Y/r$ -coordinate

(again measured in half-widths  $a$  of the mountain) shows a moving of the stagnation point towards the south for all three Rossby numbers. But this might be attributed partly to the “stretching” of the mountain in this direction (Fig.10 middle). It is more insightful to measure the Y-coordinate of the stagnation point in units of the half-width  $b$  of the mountain in this direction. Then, we obtain the location *relative* to the mountain (Fig.10 right). With this perspective we get again the situation that the position relative to the mountain changes only for intermediate Rossby numbers ( $Ro^x = 1$ ), while it remains approximately fixed for large and small Rossby numbers. It is clear that in the nonrotating limit ( $Ro^x = \infty$ ) the stagnation point lies on the along-flow symmetry axis of the mountain ( $Y = 0$ ). In the quasigeostrophic limit ( $Ro^x \ll 1$ ), on the other hand, the induced mountain anticyclone leads to a stagnation

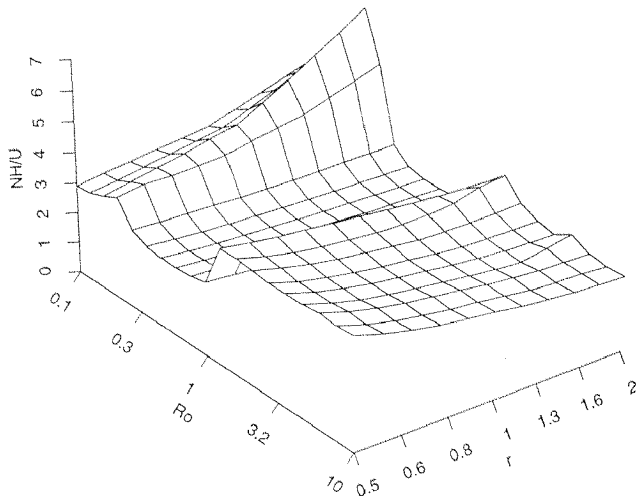


Figure 11. As Fig.9, but with *downstream* stagnation taken into account. The “valley” corresponds to downstream stagnation.

point at the normal-to-flow symmetry axis of the mountain ( $X = 0$ ). Now, in our experiments we keep fixed the along flow half-width  $a$  of the mountain and thus the corresponding Rossby number  $Ro^x = U/af$ . But, the normal-to-flow Rossby number  $Ro^y = U/bf = 1/r \cdot Ro^x$  varies in accordance with the aspect ratio  $r$ . In the intermediate range ( $Ro^x = 1$ ), this means  $Ro^y = 2$  for  $r = 0.5$  and  $Ro^y = 0.5$  for  $r = 2$ . Therefore,  $Ro^y$  changes in a critical range, which in turn forces the moving of the stagnation point from the upstream position for  $r = 0.5$  towards the right (when looking downstream) to the southern position for  $r = 2$ . This might give a hint for the qualitative shape of the curve, although it cannot explain it quantitatively.

We compared the predictions of the linear theory for upstream stagnation with nonlinear simulations for a Rossby number  $Ro = 1$ . The linear model predicts critical mountain heights  $NH/U$  of

$$3.96(r = 0.5) \rightarrow 4.67(r = 1) \rightarrow 13.75(r = 2) \quad (8)$$

The nonlinear simulations, on the other hand, yield the following intervals

$$1.47\dots 1.63(r = 0.5) \rightarrow 1.5\dots 1.63(r = 1) \rightarrow 2\dots 2.25(r = 2) \quad (9)$$

As mentioned before, the estimates of the linear model are much too large. But the tendency seems to be correct, although it is by far not so pronounced as in the linear theory. This indicates already that something quite important is missing in the linear model. Note that this tendency is in contrast to the one which Smith found for the nonrotating limit. There, the critical mountain height *decreases* with increasing aspect ratio. Hence, rotational effects must not be neglected for  $Ro = 1$ !

## 4.2 Downstream Stagnation

As in the axisymmetric case, surface waves emerge downstream of the mountain for an intermediate range of Rossby numbers  $Ro^x$ . From the nature of these waves, as discussed in section 3.2, it is clear that the along-flow Rossby number  $Ro^x$  determines

the occurrence of these waves. Thereafter, they emerge approximately at the same Rossby numbers  $Ro^x$ , with the same intensity and the same along-flow wavelength as in the axisymmetric case. Only their normal-to-flow extension is substantially modified by the aspect-ratio  $r$  of the mountain. The normal-to-flow extension is essentially determined by the extension of the mountain in this direction.

In the axisymmetric case, we found that the critical height for downstream stagnation becomes smaller than the one for upstream stagnation in an intermediate range of Rossby numbers  $Ro^x$ . The same is true for arbitrary elliptical mountains (Fig.11). Note especially how insensitive the critical mountain height for downstream stagnation (the “valley” in the diagram) is with respect to the aspect-ratio  $r$ .

### 4.3 Upstream Flow Reversal and Wave Breaking

In contrast to downstream stagnation, stagnation in the free atmosphere, i.e. above the mountain, reacts sensitively to the form of the mountain. We show in Fig.12 the behaviour of the dimensionless critical mountain height  $NH/U$  for flow reversal (curve A) together with the dimensionless height  $NZ/U$  where this stagnation occurs. The Rossby number is fixed at  $Ro^x = 4$ .

The height for flow reversal at  $Ro^x = 4$  shows qualitatively the same behaviour as for the nonrotating case, which was investigated by Smith (1989). *Increasing* the aspect-ratio  $r$  leads to *smaller* critical mountain heights. The explanation remains the same as the one proposed by Smith. In the nonrotating limit ( $Ro = \infty$ ) an increasing aspect-ratio  $r$  means an approach towards the 2d-ridge case. For a 2d-ridge, the gravity waves, which emanate from the ridge, disperse only *in the along-flow* direction. There is no *along-ridge* dispersion as they propagate vertically. Therefore, an approach towards the 2d-ridge case (increasing  $r$ ) leads to *stronger* gravity-waves above the mountain, and therefore to an increased tendency for flow reversal and to smaller critical mountain heights.

For broad, ridge-like mountains ( $r > 1$ ), the flow reversal occurs *above* the mountain peak. The height where the flow reverses is bigger than the height of the mountain ( $NZ/U > NH/U$  in Fig.12). In contrast, for *narrow* mountains ( $r < 1$ ), the wave breaking region moves downstream (not shown), *below* the peak height.

For an approximately axisymmetric mountain ( $r = 1$ ), the critical heights for upstream stagnation (curve B) and flow reversal (curve A) intersect. This was also observed by Smith for the nonrotating limit. The physical implications remain the same as the ones discussed for the axisymmetric mountain. The process which occurs first, i.e. at lower mountain heights, will change the *qualitative* behaviour of the flow. Therefore the critical height for the other process, i.e. the one with the larger critical height, must be taken with extreme care.

### 4.4 Intersection of Isentropes with Lower Boundary

In Fig.12 the critical mountain height for the intersection of isentropic surfaces with the ground (C) is shown for a Rossby number  $Ro^x = 4$ , together with the critical heights for upstream stagnation (B) and stagnation aloft (A). The critical height for intersection increases slightly with increasing aspect ratio  $r$  of the mountain. The position of the intersection depends weakly on the aspect ratio ( $x/a \approx 1$  and  $y/a \approx 0$ ). Note that the critical height for intersection (C) is smaller than the ones for stagnation

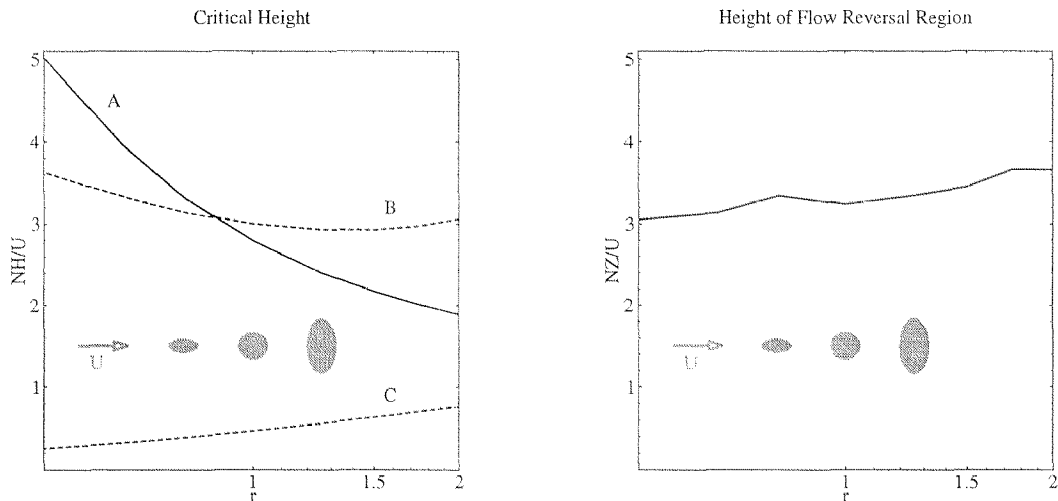


Figure 12. (Left) Linear estimates of dimensionless critical mountain height for wave breaking (A), upstream stagnation (B), and intersection of isentropes with the ground (C). (Right) Dimensionless height of wave breaking region. The Rossby number is fixed at  $Ro^\alpha = 4$

(A and B). Therefore –as already found for the axisymmetric mountain–, the limiting factor for the applicability of the linear model is this intersection. It seems that an intersection of curves A and C is possible at larger aspect ratios  $r$ . In an additional test we, therefore, chose an aspect ratio  $r = 4$ . For this ridge-like mountain we obtain a critical height for upstream flow reversal of  $NH/U = 1.53$ , whereas the one for the intersection of the isentropes with the ground is  $NH/U = 1.05$ . Although the latter is still smaller, they are similar enough such that both processes might be of relevance for the breakdown of the linear theory. We will discuss this issue further in the conclusions.

In section 4.1 we showed that flow splitting sets in for critical mountain heights  $NH/U$  of

$$1.47\dots 1.63(r = 0.5) \quad \rightarrow \quad 1.5\dots 1.63(r = 1) \quad \rightarrow \quad 2\dots 2.25(r = 2) \quad (10)$$

It is instructive to compare these obvious limiting heights for the applicability of the linear theory with the ones obtained from linear theory for the intersection of isentropes with the ground. The corresponding heights  $NH/U$  are

$$0.25(r = 0.5) \quad \rightarrow \quad 0.47(r = 1) \quad \rightarrow \quad 0.76(r = 2) \quad (11)$$

Hence, linear theory predicts the same tendency with respect to  $r$  as the nonlinear model, although these latter estimates rely on the upstream stagnation of the flow.

#### 4.5 Angle of Attack

In this subsection we study the influence of the angle with which the flow impinges on the mountain. This part is strongly motivated by the findings of the previous sections, where we obtained a pronounced dependence on the mountain shape. But there we focused only on flows parallel to the main axes of the mountain.



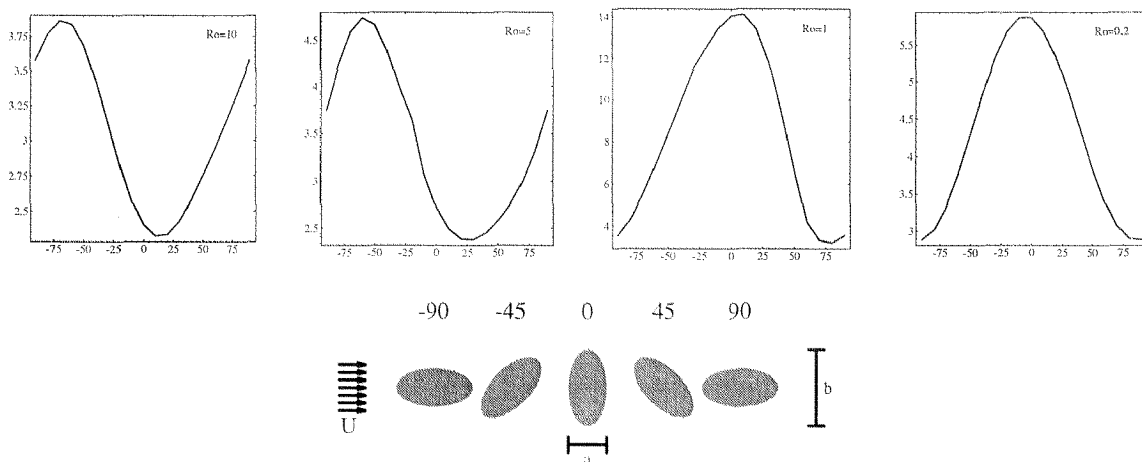


Figure 13. Critical dimensionless mountain height for upstream stagnation as a function of direction of the impinging flow. Rossby number=10, 5, 1, 0.2 from left to right.

In the following experiments we chose a mountain with fixed aspect ratio  $r = b/a = 2$ . This means a broad ridge-like mountain for a flow direction of  $\alpha = 0^\circ$ . A schematic picture illustrating the flow situation, in particular the definition of the angle, is given in Fig.13. Furthermore, there the critical mountain heights for stagnation upstream of the mountain are depicted for four different horizontal extensions (four values of  $a$  and hence  $Ro^x = U/af$ ). For the *nonrotated* case ( $\alpha = 0^\circ$ ), the along-flow Rossby number  $Ro = U/af$  takes the values 10, 5, 1 and 0.2. For an angle of rotation of  $\alpha = \pm 90^\circ$  the along-stream Rossby number changes to  $Ro = U/bf$ , i.e. half of its nonrotated value.

For large Rossby numbers a good symmetry with respect to  $\alpha$  is achieved. The small deviations from symmetry might be attributed to the still present weak rotational effects and to numerical inaccuracies. In fact, in the nonrotating case ( $Ro^x = \infty$ ) a perfect symmetry should exist, because no direction of rotation is favoured with respect to the other. In accordance with the previous sections, a minimum is observed at  $\alpha = 0^\circ$ , i.e. for broad ridge-like mountains. Good symmetry emerges also in the low Rossby number limit ( $Ro = 0.2$ ). But here, in agreement with previous results, a maximum is observed for  $\alpha = 0^\circ$ , i.e. for broad ridge-like mountains. It is in between these limiting cases that the critical height shows no symmetry with respect to  $\alpha$  (see cases with  $Ro^x = 5$  and  $Ro^x = 1$  in Fig.13)

In Fig.14 the change of the perturbation wind fields are shown for a Rossby number  $Ro^x = 1$ . It becomes clear that the flow pattern approximately “rotates” with the mountain. The main features of the flow turn in a similar way as the mountain itself. If the mountain is more asymmetric (larger values of  $r$ ) the transition from  $\alpha = -90^\circ$  to  $\alpha = +90^\circ$  might be more complex. A simple method to obtain approximate flow fields for the intermediate fields relies on the superposition principle, which applies in the linear theory. For an axisymmetric mountain, the flow solution is known (see Fig.4). If two such solutions, but with slightly shifted mountain centers, are added, a new solution is found. This solution corresponds to an elongated mountain on which the flow does not impinge along the main axis of the elongated mountain.

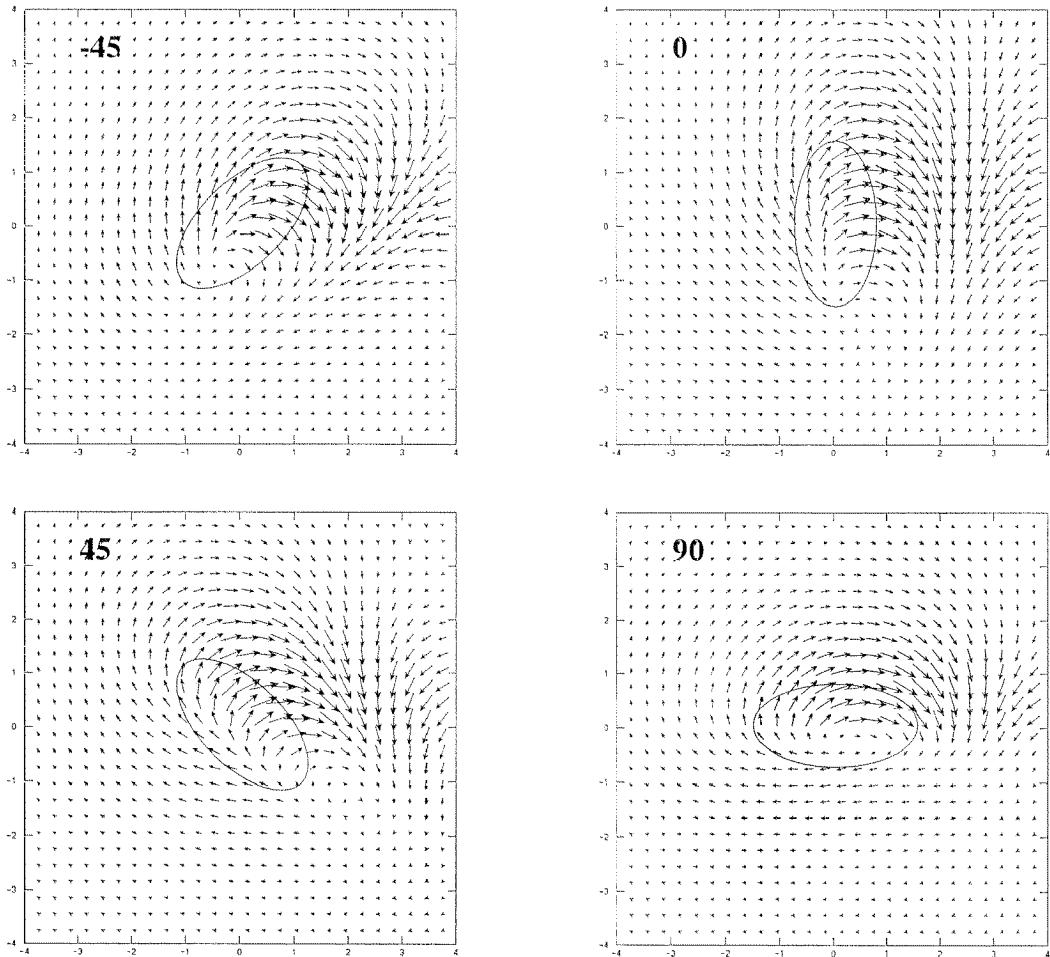


Figure 14. Perturbation wind vector  $(u', v')$  according to linear theory as a function of rotation angle of the mountain ( $\alpha = -45^\circ, 0^\circ, 45^\circ$  and  $90^\circ$  from left to right). Rossby number  $Ro^x = U/af$  corresponding to ( $\alpha = 0$ ) along-stream width is 1 (see Fig.13).

## 5 Conclusions and Further Remarks

The primary purpose of this study was to examine the validity of a linear theory. We investigated several processes which might limit the applicability of the linear theory: stagnation in the luv of the mountain (a), stagnation in the lee (b), stagnation (flow reversal) in the free atmosphere above the mountain (c), and the intersection of streamlines with the lower boundary (d). These phenomena might relate to such important nonlinear flow features as flow splitting, blocking and the formation of a Taylor cap (a), strong downstream vertically trapped waves together with vortex formation (b), the breaking of vertically propagating gravity-waves and the thus induced strong turbulence (c), and the formation of strong near surface inversions (d). The special focus of this study lies in the consideration of rotation (Coriolis force).

We found *linear* estimates for the critical heights for the above mentioned dynamical flow features. Specifically, we looked how they depend on the horizontal extension

of the mountain (the influence of the Coriolis force), on the form of the mountain, and on the direction of the impinging basic-state flow. The critical mountain heights show a strong dependence on all these parameters.

The results for an axisymmetric mountain are summarized in Fig.2. For large Rossby numbers,  $Ro \gg 1$  (small horizontal extension), the height for upstream stagnation *decreases* with *increasing* Rossby number (A, right). In contrast, it *decreases* with *decreasing* Rossby number in the low Rossby number limit ( $Ro \ll 1$ ) (A, left). In an intermediate range ( $Ro \approx 1$ ) the critical height for stagnation to the lee of the mountain is smaller than the one for stagnation on the windward side (B). The stagnation of the flow above the mountain decreases with increasing Rossby number (C). This is in agreement with the stronger wave activity in this case. Furthermore, the critical mountain height is somewhat smaller than the one for upstream stagnation. The most restricting factor is the intersection of the streamlines with the topography (D). It is only for the quasigeostrophic limit that the critical mountain heights for intersection of the isentropic surfaces become larger than the ones for the other limiting factors.

With respect to the form of the mountain, two extremal cases might be compared: narrow elongated mountains and broad, ridge-like mountains. We were able to verify Smith's result for the weakly nonrotating limit ( $Ro \gg 1$ ). There, the critical mountain heights for stagnation on the windward side of the mountain fulfill the relation  $H(\text{ridge-like}) < H(\text{elongated})$  (Fig.9). In the quasigeostrophic limit ( $Ro \ll 1$ ), on the other hand, the reverse is true:  $H(\text{ridge-like}) > H(\text{elongated})$ . Furthermore, the stagnation point moves from its position on the along-flow symmetry axis in the nonrotating limit towards the south to its position near the normal-to-flow symmetry axis of the mountain in the quasigeostrophic limit ( $Ro \ll 1$ ). This displacement of the stagnation point might correspond to a transition of the physical implications of the stagnation. Whereas stagnation in the nonrotating case is associated with blocking and flow splitting, it might be associated with Taylor cap formation in the quasigeostrophic limit. The critical mountain heights for stagnation in the lee of the mountain depend only weakly on the aspect ratio of the mountain. Finally, the critical heights for flow reversal were found to show the qualitative behaviour already stated by Smith. Ridge-like mountains favour flow reversal with respect to elongated mountains. For an along-flow Rossby number of 4 we showed that the critical mountain height for the intersection of isentropic surfaces with the ground is smaller than the ones for the other limiting factors (see Fig.12).

The linear model predicts critical mountain heights for upstream stagnation and flow reversal aloft which are too large. It is only the critical height for intersection of isentropic surfaces with the ground which stays small ( $NH/U \approx 0.5$ , with the exception of the quasigeostrophic limit). Therefore, it is this intersection of the isentropes with the surface which restricts the applicability of the linear model, and therefore calls in question the critical mountain heights for the other limiting processes. From this observation one might wonder whether the linear model is even *qualitatively* able to yield critical mountain heights for upstream stagnation and stagnation aloft, i.e. the correct behaviour with respect to Coriolis force, flow direction and form of the mountain. A final answer to this question cannot be given as a result of this work. But it might be noted that the non-dimensional mountain heights for upstream stagnation, as found by the nonlinear model, remain of order 1. Therefore, it might be in fact the non-dimensional mountain height  $NH/U$  which determines whether the flow splits or not. If so, the aspect-ratio, the Rossby number and the flow direction would only be

additional, "secondary" parameters with respect to the non-dimensionless mountain height. A further study on this point would be highly desirable.

Of course, it is not possible to compare these theoretical, highly idealized model studies *directly* with observations. The occurrence of nonlinear phenomena, such as flow splitting and wave breaking, will be strongly modified by complex topographic and synoptic/mesoscale atmospheric conditions which can be incorporated in theoretical studies only with great difficulties. Furthermore, temporal changes in the large scale flow can considerably influence the atmospheric response due to a mountain. But, the linear results might give a *hint* whether a nonlinear phenomena occurs or not. They yield a theoretical background. So, for example, if the large scale wind impinging on the Alps turns from west to north-west, the aspect-ratio of the Alps changes. This would lead to a change in the tendency for flow splitting, according to our linear results. It might be of some interest to look for such effects.



# PART D

# THE MODIFICATION OF A FRONT BY THE ALPS: A CASE STUDY USING THE ALPEX REANALYSIS DATA SET<sup>1</sup>

NATASCHA KLJUN,<sup>2</sup> MICHAEL SPRENGER and CHRISTOPH SCHÄR

## Summary

The interaction of a cold front with the Alps is studied by means of real- case numerical simulations. The case considered happened at the end of the Alpine Experiment (ALPEX) on 28 April - 2 May, 1982. Simulations are performed with the numerical weather prediction model chain EM/HM of the German and Swiss Weather Services. The outer EM simulation (56km horizontal resolution) uses initial and lateral boundary fields taken from the ALPEX IIIb reanalysis data set compiled by the German Weather Service. This reanalysis data set is based on the operational EM analysis scheme but takes into consideration a wide range of field phase data taken during the ALPEX field campaign. A comparison is performed of simulations driven by the ALPEX and ECMWF reanalysis data. The simulation driven by the former captures the intensity and vertical depth of the developing lee cyclone substantially better than the corresponding run driven by the ECMWF reanalysis.

The transient development of the cold-frontal interaction including a wide range of associated mesoscale phenomenon is analysed using HM simulations with a horizontal resolution of 14km. These show that the north-westerly flow ahead of the approaching cold front is strongly blocked at low levels and experiences flow splitting to the north of the Alps. The passage of the front induces a cold-air outbreak between the Alps and the Pyrenees. The calm air over the Po valley later gives in to pronounced north Foehn which develops when cold-air masses pile up to the north of the Alps and finally spill over it. There is a strong northerly jet to the south of the Gotthard pass, associated with well-pronounced low-level potential vorticity (PV) banners to the east and west of the jet. These streamers are dynamically generated by flow separation at the "exit" of the Gotthard valley transect. Flow separation is also evident at the western edge of the Alps, associated with strong Mistral. The thereby created positive PV anomaly appears to interact with a synoptic-scale upper level PV streamer, which crosses the Alps and finally develops into a deep lee cyclone in the Gulf of Genoa. At the eastern edge of the Alps, the strong northerly wind does not separate from the topography, but rather the associated Bora flow over the Dinaric Alps remains attached to the topography and penetrates as a easterly flow over the Po valley. To visualize and analyze these flow evolutions, a comprehensive trajectory calculations are performed.

---

<sup>1</sup>to be submitted to *Beitr. Phys. Atmosph.*

<sup>2</sup>Corresponding author: Swiss Federal Institute of Technology, GI-ETH, Winterthurerstr. 190, CH-8057 Zürich, Switzerland, e-mail: kljun@geo.umnw.ethz.ch

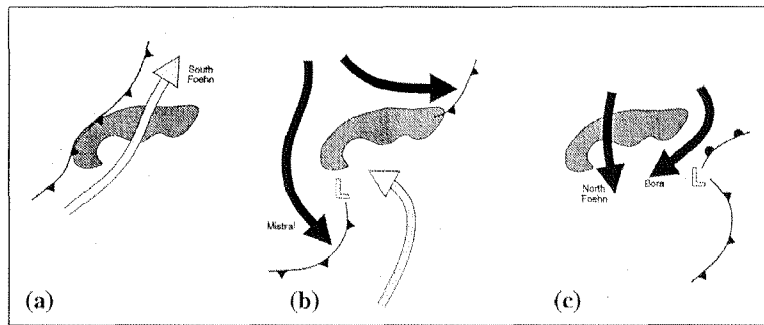


Figure 1. Interception of a cold front by the Alpine crest. (a) deformation of the cold front and onset of south Foehn, (b) cold-air outbreak into the western Mediterranean (Mistral) and formation of a lee cyclone, (c) eastwards progression of the lee cyclone and onset of Bora and north Foehn (adapted from Smith 1985b, figure from Schär et al. 1998).

## 1 Introduction

The interaction of a cold front with the Alps is still in the focus of Alpine mountain meteorology. For instance, many of the objectives of the Mesoscale Alpine Programme (MAP) are directly or indirectly related to the passage of a cold front in the Alpine region (Binder and Schär 1995). Besides the influence of the Alps on the shape and intensity of the front itself, the passage of a cold front is often associated with many mesoscale weather systems (see Figure 1). Ahead of the cold front there may be southerly prefrontal Foehn in the Alpine valleys. As the northerly winds impinge on the Alps, the flow splits on the windward side. Westward deflected cold-air masses are responsible for a cold-air outbreak into the Mediterranean sea between the Alps and the Pyrenees. The resulting Mistral wind is then further intensified by the channelling along the Rhone valley. Later the calm in the Po valley is usually replaced by the North Foehn. Over the gulf of Genoa a lee cyclone may form. Finally, the eastward deflection of cold air around the Alps leads to the formation of the north-easterly Bora wind which flows over the Dinaric Alps, and sometimes reaches as far west as the Po valley. In this study we consider such an event which contains almost all of the aforementioned mesoscale flow features. The case occurred at the end of the Alpine Experiment (Kuettner 1980).

One particular objective of our study is the assessment of the ALPEX-IIIb reanalysis data set. This reanalysis was conducted by the German Weather Service (DWD) for the ALPEX Special Observing Period SOP, 1 March – 30 April 1982, and the following 8 days which were included due to a strong South Foehn case which occurred briefly after the end of the SOP (Gerhard 1994). The value of this reanalysis will be assessed by comparing a pair of 56 km EM simulations driven by the ALPEX and ECMWF reanalysis data set, respectively. The simulations cover the period from 29 April 00 UTC to 1 May 1982, 08 UTC. It will be shown that the additional information available in the ALPEX-IIIb reanalysis results in a substantially improved simulation of the overall development and in particular of the formation of a lee cyclone associated with the selected case. This result is of some interest and may suggest that the generation of a reanalysis data set for the forthcoming MAP special observing period is well justified.

The second objective of the study is to provide a detailed high-resolution account



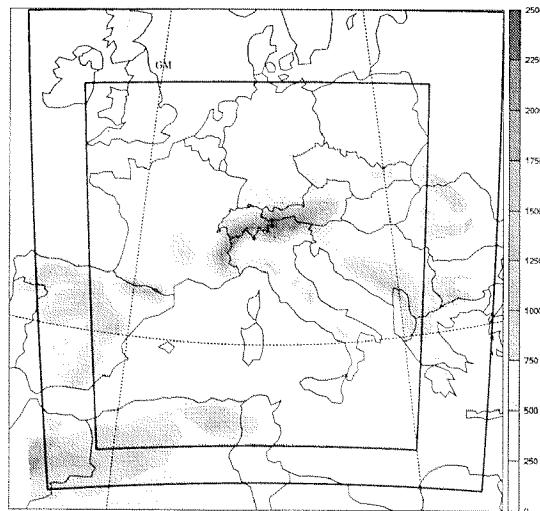


Figure 2. Horizontal domain of the EM and one-way nested HM simulation, respectively. Shaded: EM topography.

of the associated mesoscale flow systems in the Alpine region. To this end, the EM simulation will be driven by the ALPEX-IIIb reanalysis and refined by high-resolution (14 km) simulations using the HM model. This model is used by the German and Swiss weather services for operational forecasting in slight different domains.

In our analysis of the simulations, we focus on the transient development of synoptic and mesoscale features and wind systems. This analysis includes time series of variables at selected locations, and trajectory calculations using the methodology of Wernli (1995) to elucidate the flow splitting north of the Alps, the channelling of the air through the Gotthard pass and the strong deflection of the air at the eastern edge of the Alps. Special emphasis is further given to the potential vorticity (PV) perspective in terms of upper-level PV advection (Mattocks and Bleck 1984; Tafferner 1990), diabatic generation of PV vortices (Hoskins et al., 1985; Morgenstern 1998), and low-level PV banners to the lee of the Alps (Aebischer and Schär 1997).

The flow features to be addressed include the retardation and modification of the impinging cold front (cf. Davies 1984; Heimann and Volkert 1988; Hoinka et al. 1990; Egger and Hoinka 1992), the blocking and splitting of the incident flow (Pierrehumbert and Wyman 1985; Chen and Smith 1987; Binder et al. 1989), the cold-air outbreak into the Western Mediterranean sea and the associated generation of northerly Mistral winds (Pettre 1982), the formation of an Alpine lee cyclone over the Gulf of Genoa (e.g. Buzzi and Tibaldi 1978), the onset of North Foehn over southern Switzerland and the Po valley, the onset of Bora winds over the Dinaric Alps, and the formation of an anticyclonic orographic vortex over the Adriatic sea (Steinacker 1984a, 1984b).

The outline of the paper is as follows: Section 2 presents the numerical model and gives a brief discussion of the driving reanalysis products. In section 3 we compare simulations driven by the ALPEX-IIIb reanalysis and the ECMWF reanalysis. Section 4 provides a detailed analysis of associated mesoscale flow systems. Sensitivity experiments regarding the effects of surface friction, orographic height and diabatic processes follow in section 5. The paper is concluded in section 6.

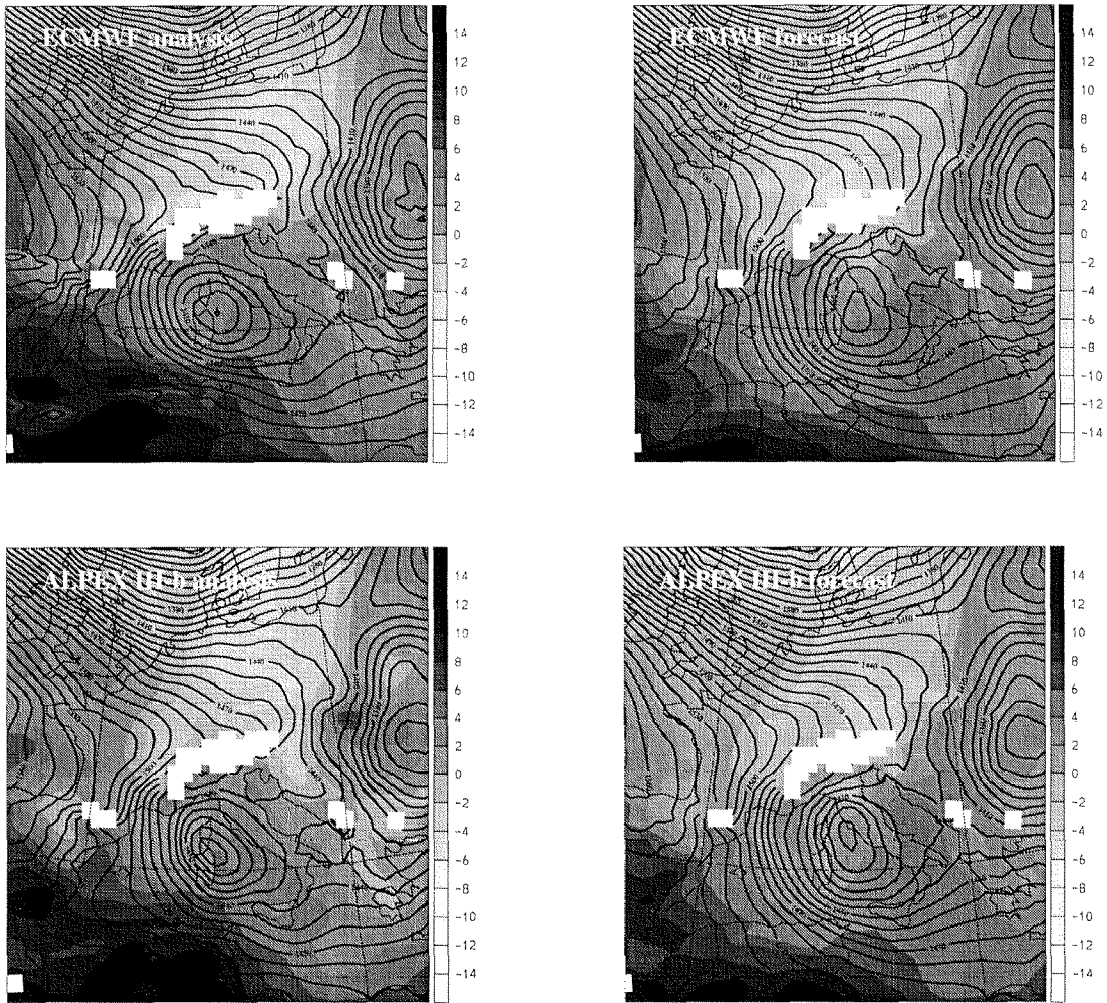


Figure 3. Geopotential and temperature at 850 hPa at time  $t=42$  h for ECMWF and ALPEX-IIIb analysis and forecast, respectively. The white areas correspond to the intersection of the 850 hPa-surface with the topography. A lee cyclone is correctly captured by both forecasts.

## 2 Numerical Model, and Initial and Lateral Boundary Conditions

### 2.1 Modelling System

All simulations of the study were performed with the numerical modelling system originally developed by the German Weather Service (DWD). The low-resolution version of this model is referred to as the Europa-Modell (EM). It has a horizontal grid spacing of 56km and is used operationally by the DWD with a domain covering all of Europe as well as the Northern Atlantic. The high-resolution model (HM) is one-way nested into the EM, has a horizontal resolution of 14km and has been derived from the EM in a collaboration between the DWD and the Swiss Meteorological Institute (SMI). These institutions run the HM to provide high-resolution short-range weather forecasts. A detailed description of the model can be found in Majewski (1991) and

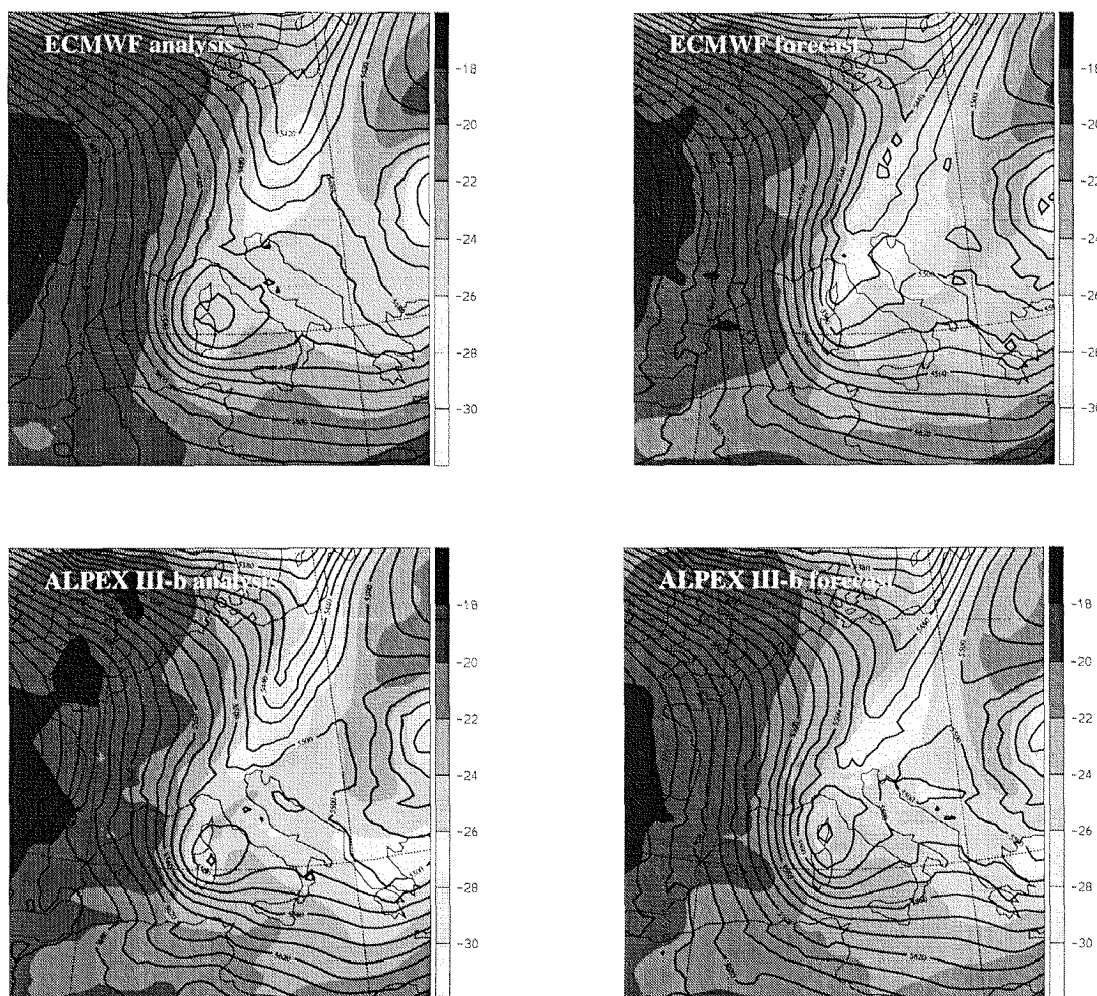


Figure 4. Geopotential and temperature at 500 hPa at time  $t=42$  h for ECMWF and ALPEX-IIIb analysis and forecast. Note that the ECMWF forecast shows *no* closed geopotential contours, in contrast to the analyses and the ALPEX-IIIb forecast.

Schrodin (1995).

The model is based on the hydrostatic approximation. Furthermore, it contains advanced physical parameterizations for radiation (Ritter and Geleyn 1992), surface layer processes (Louis 1979), boundary layer processes and turbulence (Mellor and Yamada 1974, Müller 1981) and grid-scale cloud microphysics of the Kessler type including a parametrization of the ice phase and moist convection (Tiedtke 1989). For the HM simulations, a KDB-type gravity wave absorber is employed at  $p = 20$ hPa level (see Klemp and Durran 1983; Bougeault 1983). The implementation of this absorber in pressure coordinates is by Herzog (1995). At the lateral boundaries the models are driven using relaxation boundary conditions (Davies 1976). The relaxation zones have a width of 8 grid points, and the boundary updating frequencies are 6 h and 2 h for the EM and the HM, respectively. For the interim times, the boundary fields were linearly interpolated in time.

Here we used a  $55 \times 55 \times 20$ -grid for the EM run and a  $163 \times 163 \times 30$ -grid for the

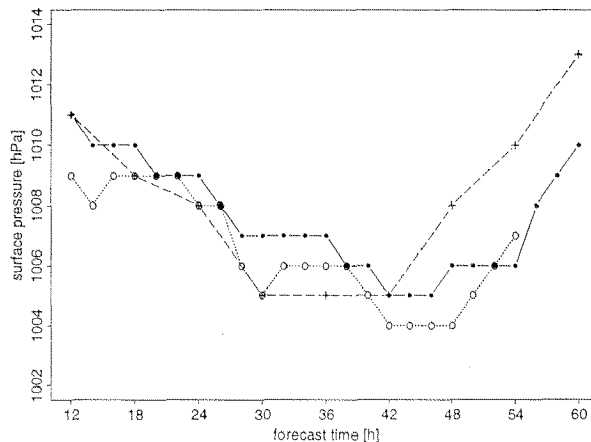


Figure 5. Evolution of mean sea-level pressure (hPa) in the center of the cyclone based on ALPEX-IIIb reanalysis data (+ - - +), EM run (● - ●), and HM run (○ · · ○).

one-way nested HM run was used. The purpose of the  $56km$  EM run is primarily the generation of driving fields with appropriate temporal resolution of 2h. In order to improve the representation of gravity waves, the explicit rather than the semi-Lagrangian advection was employed for our integrations with time steps of 300s for the EM and 75s for the HM run. The domains for the outer EM and the one-way nested HM are presented in Figure 2. Note that the employed HM domain extends further east and south than the operational domains employed by the Swiss and German Weather Services. The numerical models were initialized on 29 April 1982 00 UTC and are integrated for 56 h. Throughout the integration period the EM is driven at its lateral boundaries by either the ECMWF reanalysis or the ALPEX-IIIb reanalysis.

## 2.2 The ALPEX-IIIb Reanalysis from DWD

The EM analysis scheme is based upon optimal interpolation and an earlier version of the ECMWF data assimilation scheme (Lönnerberg and Shaw 1987, see also Schrodin 1995). The ALPEX-IIIb reanalysis itself has its origin in the ALPEX project (Gerhard 1994). The German Weather Service (DWD) performed a reanalysis (based on GTS data) of the slightly extended AlpeX Special Observing Period (SOP, 1 March – 8 May 1982). The initial and boundary fields are available every 6 hours on the rotated spherical model grid ( $181 \times 129$  grid points, mesh size  $0.5^\circ$ , 20 vertical hybrid levels and additionally interpolated to 11 standard pressure levels). The following three-dimensional fields are included in the data set: temperature, geopotential, water vapour and cloud water contents, relative humidity (on pressure levels only), horizontal wind components and vertical velocity (for the initialized analysis only). Surface fields are: surface pressure, temperature, snow amount, soil temperatures and water contents (2 layers), temperature and dew point at 2 m above ground, wind components at 10 m above ground, radiation balance at the top and bottom of the atmosphere, cloud cover (high, medium, low, total), sensible and latent heat fluxes and momentum flux at the surface, base and top of main convective clouds (the last 6 surface fields only for the initialized analysis).

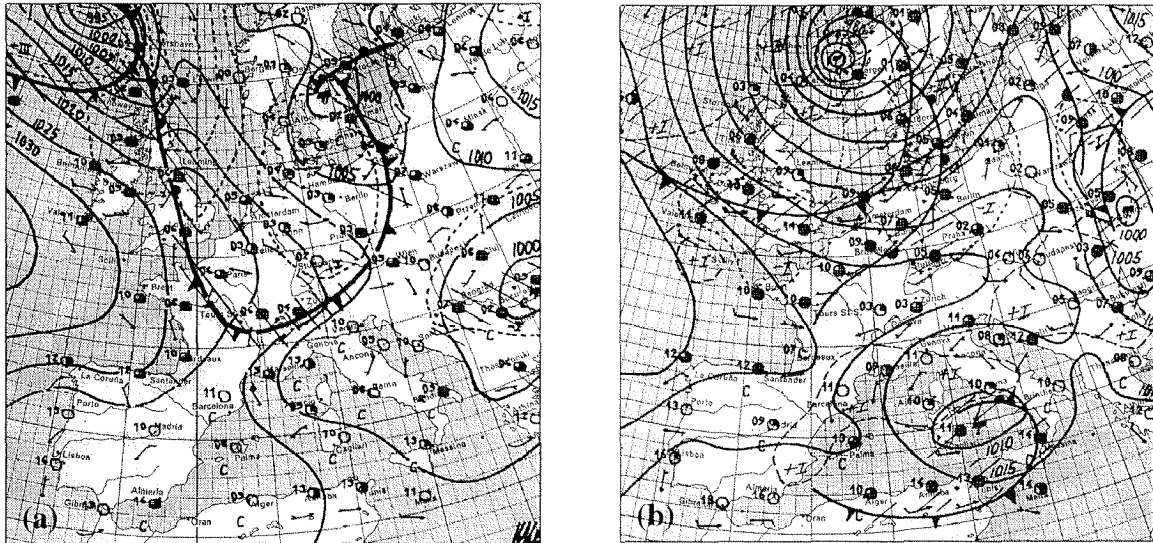


Figure 6. Surface weather charts of the Swiss Meteorological Institute at 00 UTC on (a) 30 April and (b) 1 May 1982. A cold front impinges on the Alps from north. In subsequence, a lee cyclone develops in the Gulf of Genoa.

### 3 Comparison of ALPEX versus ECMWF reanalysis

In Figures 3 and 4 the ECMWF analysis and the ALPEX-IIIb analysis are compared. Also shown are the results of EM forecasts using the two above mentioned analysis data sets as initial and lateral boundary values. The lee cyclone is captured by both the ECMWF and the ALPEX-IIIb reanalysis. At the 850 hPa level, it is somewhat stronger in the ALPEX-IIIb reanalysis (Figure 3, lefthand panel). In contrast, at 500 hPa, the closed contour lines are more prominent in the ECMWF reanalysis (Figure 4, lefthand panels). In terms of the forecast, however, the lee cyclone is substantially stronger when the forecast is driven by initial and boundary fields of the ALPEX-IIIb analysis than by the ECMWF reanalysis. In the latter run, no closed contour lines emerge at the 500 hPa level. Even at forecast time +48 h (not shown), no cut-off low formation takes place in the ECMWF driven simulation. In contrast, the ALPEX-IIIb run is well able to capture this feature, as can be validated against the ECMWF and the ALPEX-IIIb reanalyses.

The upper-level PV trough at the 310 K isentropic surface also shows substantial differences. The ALPEX-IIIb reanalysis, as well as the ALPEX-IIIb forecast, show the wrap-up of a PV streamer above Sardinia, whereas the runs using the ECMWF reanalysis are unable to predict that phenomenon. Recent studies (Fehlmann et al. 1999) demonstrate the importance of such upper-level PV features for heavy precipitation events in the Alpine region.

Concluding, the lee cyclone is simulated too weak and especially too shallow in its vertical extension when running the simulation with the ECMWF reanalysis. Therefore, in the subsequent sections the EM run driven by the ALPEX-IIIb reanalysis will be used.

Figure 5 shows a comparison of the minimum pressure attained in the ALPEX-IIIb reanalysis, and the respective EM and HM integrations. The cyclone in the lee of the

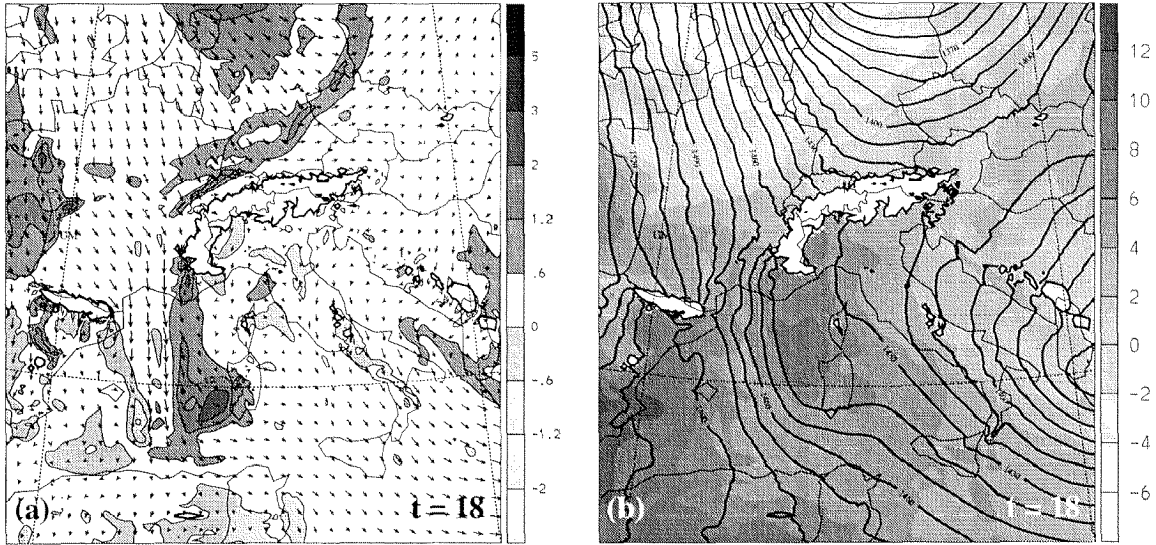


Figure 7. (a) Potential vorticity in pvu and wind field at 850 hPa after 18 hours of simulation; (b) temperature and geopotential at 850 hPa. The cold front is marked by wind shear, an elongated PV anomaly and an increased temperature gradient.

Alps is strongest in the HM simulation and weakest in the reanalysis.

At the 850 hPa surface the difference between reanalysis and HM forecast reaches about 30 gpm, though the location of the cyclone is about the same in reanalysis and EM/HM simulations. The time of the pressure minimum is lagged by 12 h in the HM simulation with respect to the analysis.

Finally, the sensitivity of the outcome of the model run with respect to the starting time of the integration was examined. Two model runs based on analysis starting at 00 UTC and at 12 UTC on 28 April 1982, respectively, were compared. The observed differences between the simulations were only minor.

## 4 Synoptic and Mesoscale Weather Development

In this chapter, the weather development in observations and corresponding simulation in the Alpine region from 29 April to 1 May 1982 is described. The event was selected for study since it shows a rich variety of dynamical features which are temporarily connected. All EM/HM simulations were initialized at 00 UTC on 29 April 1982 and integrated over 56 hours. The section is arranged according to the approximate temporal occurrence of the different flow phenomena: (a) approaching cold front and flow splitting, (b) Mistral and cold-air outbreak, (c) north Foehn, (d) lee cyclogenesis, and (e) anticyclone and Bora. Unless mentioned otherwise, all simulation diagrams are taken from the 14km HM run.

### 4.1 Approaching Cold Front and Flow Splitting

On 28 April 1982 a warm air mass is located over the central parts of Europe. In the course of the following day, the air is replaced by cold air impinging on the Alps from the north. The related cold front (Figure 6) appears in the northern parts of Central Europe 14 hours after the start of the simulation. It can easily be located due to

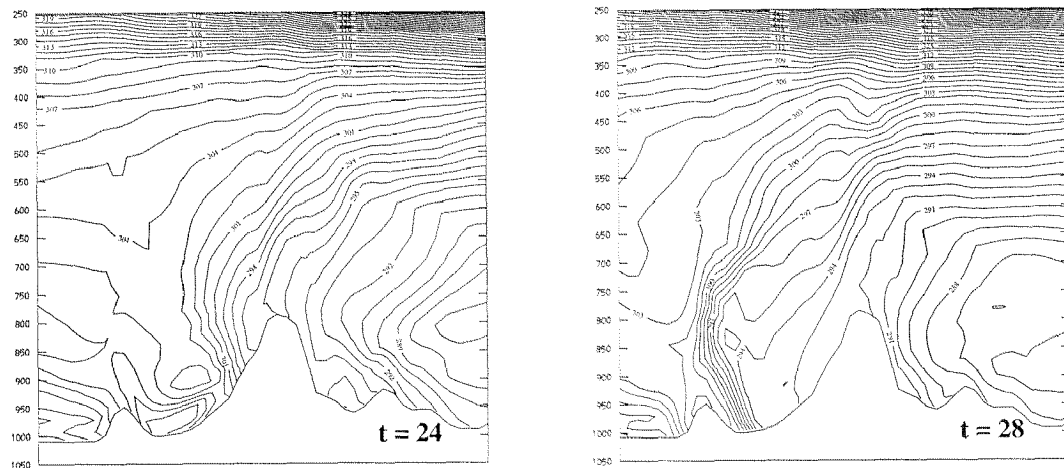


Figure 8. Equivalent potential temperature over a south/north section of the Alps, crossing the Gotthard, after 24 and 28 hours of simulation (contour line interval  $1^{\circ}$  Kelvin). The large horizontal gradient corresponds to the cold front, which intensifies with the passage over the Alpine crest.

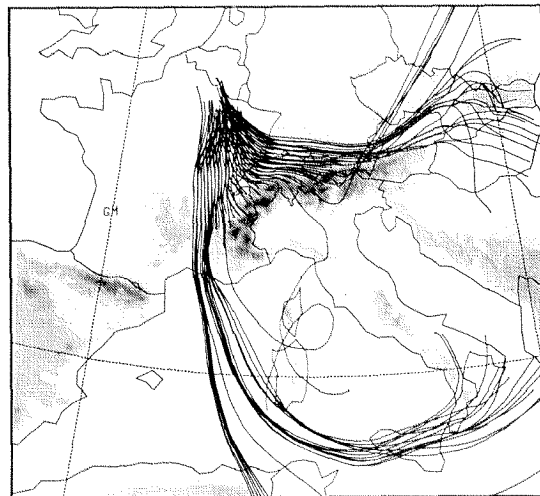


Figure 9. Trajectories starting in the north of the Alps at 870 to 850 hPa. The left part of the trajectories sinks after 6 hours of simulation down to 960 hPa and rises again over the Mediterranean to 670 hPa. The right part rises immediately and finally ends at 740 hPa on average.

wind shear, cold air moving south, strong precipitation and an elongated potential vorticity (PV) feature of diabatic origin (Figure 7).

The cold front moves rapidly towards the Alps and reaches the Alpine crest after 24 hours of simulation. At that time northern flow persists over the Alps, while in the lee of the Alps pressure differences remain low and temperatures high (comparable to time 18, see Figure 7b).

With the passage of the front over the Alpine crest, a strong horizontal gradient in equivalent potential temperature develops south of the Alps (Figure 8). The gradient

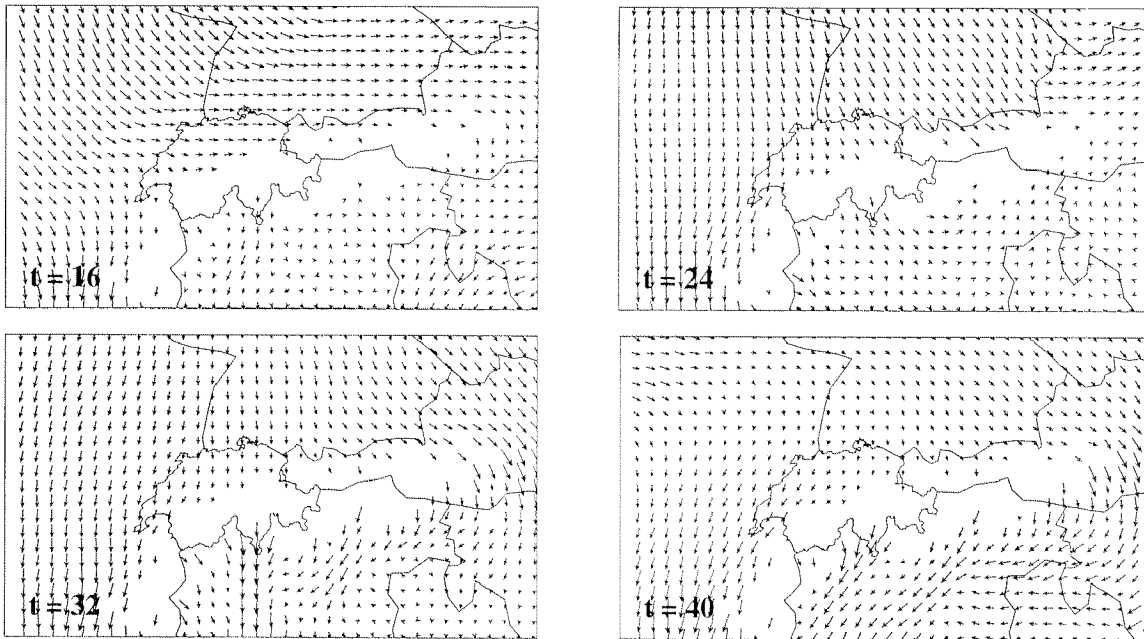


Figure 10. Wind vectors at 850 hPa for time  $t=16$  h, 24 h, 32 h, 40 h. At  $t=16$  h, the flow splits north west of the Alps. With the passage of the front ( $t=24$  h), the tendency for flow splitting is considerably reduced. The calm in the Po valley is finally removed with the onset of north Foehn ( $t=32$  h and  $t=40$  h). Jets emerge south of the Gotthard and south of the Brenner pass.

intensifies considerably with the passage over the Alps. Such a modification of the impinging frontal structure was also reported for another case by an observational study (Hoinka et al. 1990). High values of relative humidity arising from deep convection are found up to 300 hPa (not shown). North of the Alps, on the other hand, only a small gradient in equivalent potential temperature is seen. Figure 8 also shows the retardation of the cold front near the surface. Although the cold front is retarded by the Alps, it is –with a deformation– still visible after crossing them.

The northern low-level air is blocked by the Alps. At time  $t = 16$  h, i.e. 8 hours before the front reaches the Alpine crest, the wind vectors at 850 hPa show clear signs for flow splitting (Figure 10). At this level, the air moves sideways around the Alps. The splitting of the flow at the eastern part of the Alps is also confirmed by trajectory calculations (Figure 9). A detailed description of the used trajectory tool is given by Wernli and Davies (1996). The trajectories were started at time  $t = 12$  h in a small volume north of the Alps. They were then calculated 42 h *forward* in time and 12 h *backward* in time. Thus, the starting point of each trajectory corresponds to time  $t = 0$  h. The starting points lay ahead of the cold front, at levels between 870 hPa and 850 hPa. Note how some air parcels are blocked severely upstream of the Alps and are unable to surmount them. Others drift westwards, flow around the Alps and end up in the cyclonic eddy or they are directed around the east of the Alps. The air parcels which turn to the right, i.e. towards the Rhone Valley, sink to a level of 960 hPa and rise again to higher levels when they reach the Mediterranean. The eastward advected parcels, in contrast, rise immediately to heights of about 740 hPa, which is a typical behavior for a frontal circulation.

When the cold front reaches the Alpine crest at time  $t = 24$  h, the tendency for



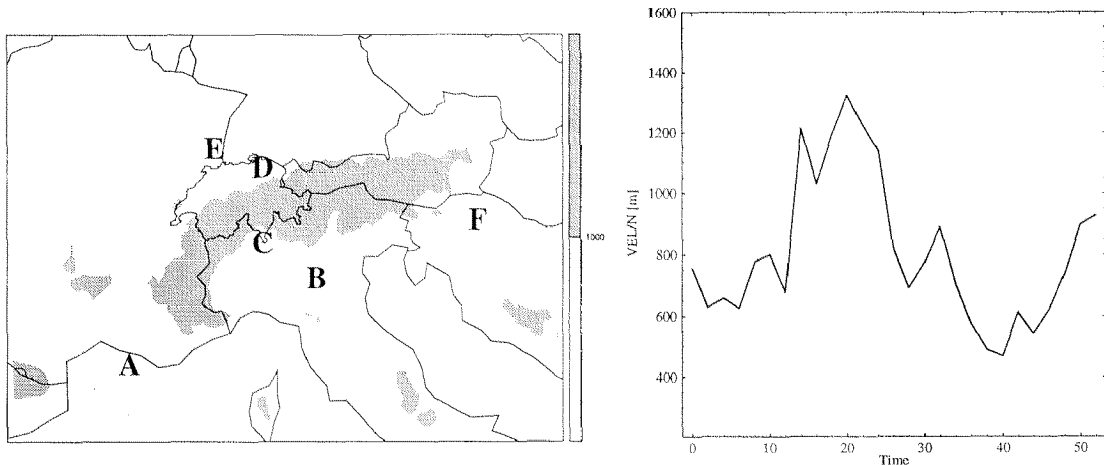


Figure 11. (Left) Coordinates of selected points for timeseries analysis  $A : \lambda = 4.7^\circ, \phi = 42.8^\circ; B : \lambda = 10^\circ, \phi = 45.5^\circ; C : \lambda = 8.4^\circ, \phi = 45.8^\circ; D : \lambda = 8.4^\circ, \phi = 47.2^\circ; E : \lambda = 7.6^\circ, \phi = 48.7^\circ; F : \lambda = 15.7^\circ, \phi = 46.3^\circ$ . (Right) Ratio  $|\vec{V}|/N$  at point E at 850 hPa as a function of time. Small values correspond to increased tendency for flow splitting.

flow splitting is much reduced (Figure 10). This behaviour is in qualitative agreement with estimates of the dimensionless mountain height  $NH/U$ , where  $N$  is the upstream Brunt-Vaisällä frequency,  $U$  the upstream velocity (approximately normal to the Alpine chain) and  $H$  the height of the Alps. For illustration, figure 11 displays the ratio  $|\vec{V}|/N$  at point E (Figure 11, right) upstream of the Alps at 850 hPa. With the approach of the cold front, the tendency for blocking is much reduced after about 20 hours.

#### 4.2 Cold Air Outbreak and Mistral

A strong northerly flow between the Pyrenees and the Alps develops around time  $t = 10 h$  (Figure 13). It then remains constant at  $20 m/s$  during the next 15 hours. At the time of the cold frontal passage, there is a transient increase in specific humidity (Figure 13). The stronger blocking of the northern air and the resultant strengthened channeling of the air along the Rhone valley between the Alps and the Pyrenees leads to a further increase of the northerly jet up to  $27 m/s$  behind the cold front. The maximum of the Mistral jet is located at about 900 hPa and is separated from the calm air in the lee of the Alps by a region of strong horizontal shear. The related cold-air breakthrough also implies a decrease in temperature by about  $6^\circ$ . At its maximum, at time  $t = 36 h$ , the impressive jet reaches as far to the south as Sicily (Figure 12).

#### 4.3 North Foehn

Behind the front, cold air is advected towards the Alps and finally blocked. The air, therefore, piles up to the north, spills over the mountain and induces the north Foehn. The associated strong winds replace the earlier almost windless situation south of the Alps (see Figure 10). Measurements from the surface meteorological ANETZ network of the Swiss Weather Service, confirm Foehn winds in the southern part of Switzerland on 30 April (Figure 14). Observations at two ANETZ stations in southern Switzerland

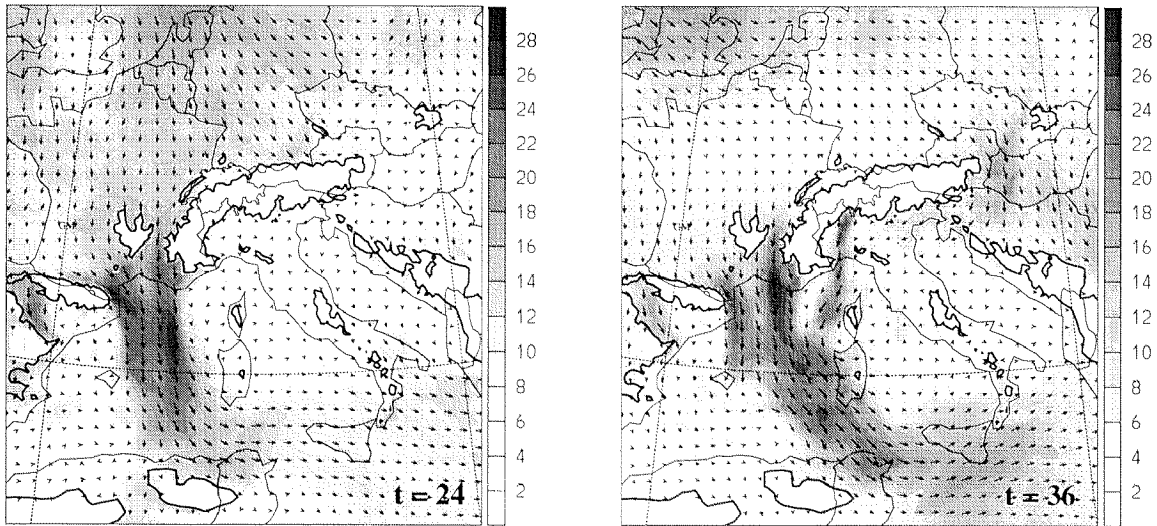


Figure 12. Wind field and horizontal velocity (shaded, in m/s) at 900 hPa after 24 and 36 hours of simulation. Strong winds prevail between the Alps and the Pyrenees and extend far towards the south. They are separated from the initial calm in the Po valley by a strong shear line. The jet south of the Gotthard pass finally removes this calm air ( $t=36$  h).

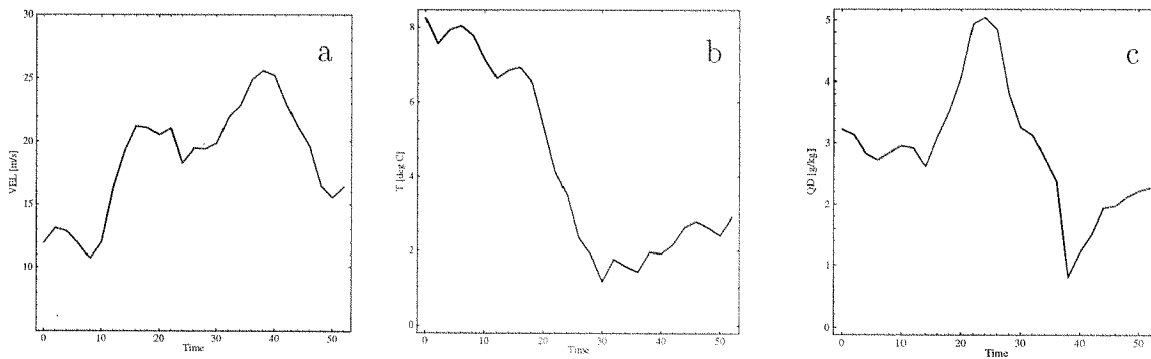


Figure 13. (a) Wind velocity, (b) temperature and (c) specific humidity as a function of time at 850 hPa, between Pyrenees and Alps, at point A in Figure 11. The steep increase in wind speed (a) marks the onset of a cold-air outbreak into the Mediterranean with a subsequent temperature drop of about 6 K (b). The peak in specific humidity (c) marks the passage of the cold front.

show suddenly increasing temperature and wind velocity while pressure and humidity decrease, i.e. typical characteristics of a Foehn event.

As a further indication of Foehn, a strong pressure contrast across the Alps develops some hours before the front reaches the Alps (Figure 15). The pressure gradient reaches its maximum value of 16 hPa/100 km after 34 hours of simulation, compared to 2-4 hPa/100 km at the onset. This increase in pressure contrast is present along the whole range of the Alps. The large gradient is partly caused by the rapid pressure increase to the north of the Alps following the frontal passage (Figure 15). In addition to this hydrostatic build-up of a windward high pressure, the strong northerly winds in the lee and associated gravity wave effects are an essential factor, as it leads to a leeside pressure drop. The strong deformation of the reduced surface pressure field is a typical feature of both north or south Foehn in the Alpine region.

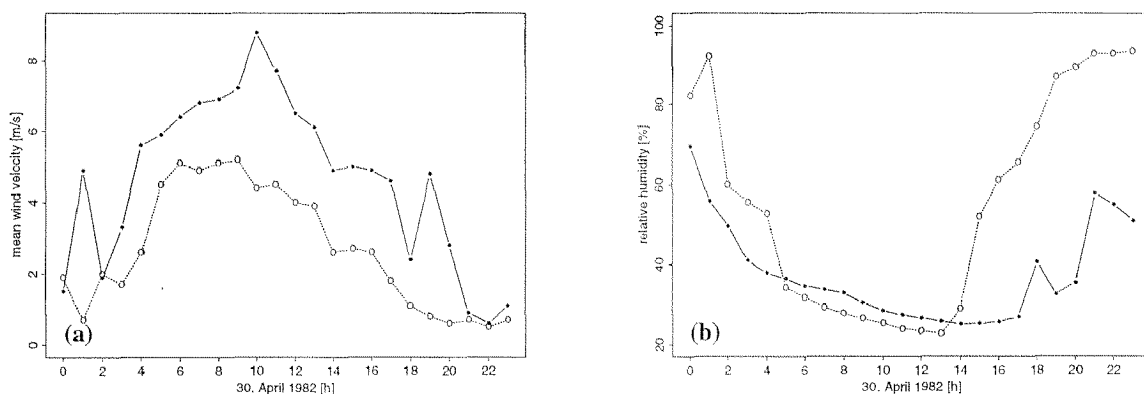


Figure 14. Measurements at Lugano (●—●) and Stabio (○ · · ○) on 30 April 1982. (a) mean wind (m/s) and (b) relative humidity (%). The steep increase of wind speed and the associated steep decrease of relative humidity indicates the onset of north Foehn in the southern parts of Switzerland.

As a striking phenomenon of the north Foehn, a strong southerly jet appears through the Gotthard valley transect (Figure 12, to the right of the Mistral jet). The north Foehn within and to the lee of this gap is considerably stronger than in the regions shielded by higher topography. The 'Gotthard jet' can be explained by means of a strong channeling of the air through the narrow pass region. It is quite remarkable how far the jet reaches towards the south.

Further trajectory calculations elucidate the flow leading to the Gotthard jet (Figure 16). The trajectories were started at point E (see Figure 11), at levels between 870 hPa and 850 hPa, and at time  $t = 24$  h. They were then integrated 12 hours backward in time (towards the north) and 30 hours forward in time (towards the south). The air is channeled through the Gotthard gap. As a consequence of the high wind velocities in the Gotthard pass, the trajectories form a coherent ensemble, i.e. they do not disperse to any noticeable extent. High wind velocities lead to the narrow distribution of the trajectories. Trajectories lose humidity (-40%) while sinking at the southern slope of the Alps and humidity does not increase until the air parcel is relocated over the sea (see table in Figure 16). During the rise and the descent of the air parcel across the Alps, an increase in potential temperature of 7K is observed. This warming and drying is due to contributions from the descent of stratospheric air, as is suggested by the vertical section in Figure 17.

Associated with the Gotthard jet, a negative and a positive PV banner (right and left, respectively, when looking downstream) develop simultaneously, moving away from the Gotthard pass (Figure 20). With increasing wind velocity, the PV banners extend 480 km towards south at a height of 850 hPa. Similar PV banners were noted by Aebischer and Schär (1998). The process leading to these PV banners is flow separation at the southern exit of the Gotthard valley transect. A south-easterly jet can also be attributed to the Brenner valley transect (Figure 10), but it is weaker than the Gotthard jet. This might be the reason why no clear PV banners can be discerned.

After 34 hours of simulation the dry stream of air in the southern part of the Alps and the associated pressure gradient decrease. The pressure distribution in the south

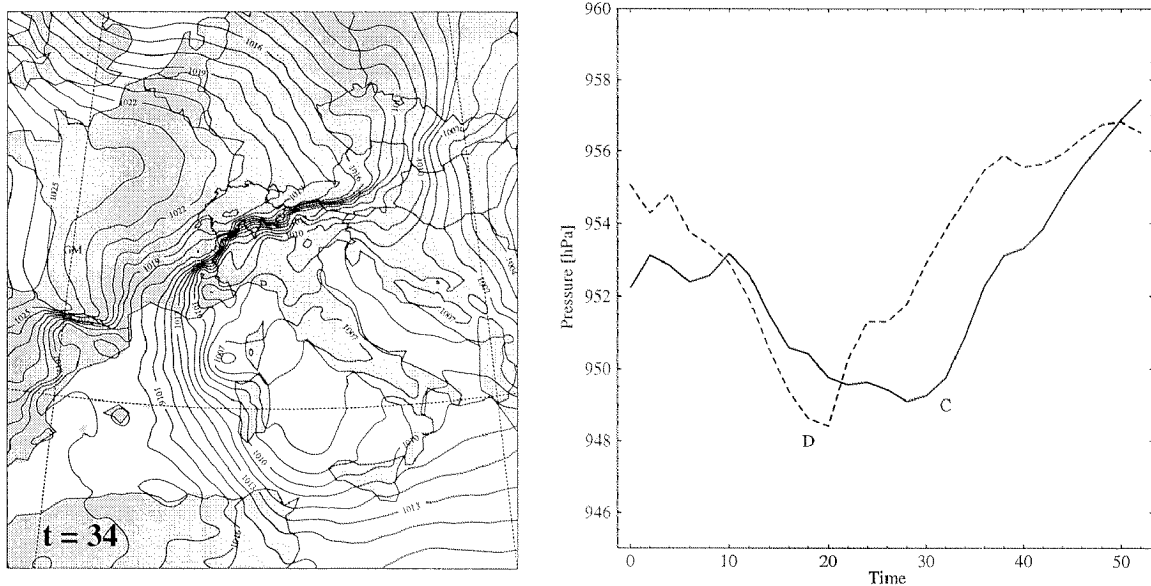
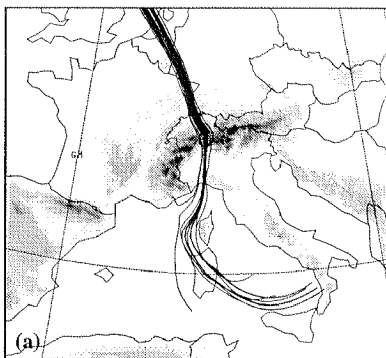


Figure 15. (Left) *Reduced* surface pressure from the HM run at time  $t = 34$  h and temporal development of surface pressure at positions C and D (see Figure 11). The strong deformation of the reduced surface pressure is due to north Foehn. (Right) The sudden increase of surface pressure at time  $t=20$  h north of the Alps (point D) contributes to the strong north/south pressure difference C-D.



t [h]	p [hPa]	$\Theta$ [K]	RH [%]	QD [g/kg]
12	$912 \pm 22$	$280.5 \pm 0.6$	$74.5 \pm 6.2$	$3.1 \pm 0.5$
16	$891 \pm 22$	$281.3 \pm 0.7$	$70.8 \pm 18.1$	$2.9 \pm 0.9$
20	$869 \pm 23$	$282.0 \pm 0.8$	$69.5 \pm 15.6$	$2.6 \pm 0.8$
24	$860 \pm 6$	$282.4 \pm 0.5$	$66.4 \pm 14.2$	$2.4 \pm 0.5$
28	$792 \pm 39$	$283.9 \pm 1.6$	$82.7 \pm 12.5$	$2.2 \pm 0.3$
32	$919 \pm 46$	$285.1 \pm 1.1$	$40.9 \pm 12.5$	$2.3 \pm 0.3$
36	$963 \pm 31$	$286.7 \pm 0.7$	$51.0 \pm 8.0$	$4.2 \pm 0.7$
40	$946 \pm 31$	$287.1 \pm 0.6$	$56.6 \pm 6.2$	$4.4 \pm 0.7$
44	$947 \pm 23$	$287.1 \pm 0.4$	$59.2 \pm 5.5$	$4.7 \pm 0.7$
48	$939 \pm 18$	$286.8 \pm 0.2$	$76.4 \pm 14.3$	$5.6 \pm 1.0$
52	$940 \pm 19$	$286.3 \pm 0.4$	$84.6 \pm 13.9$	$6.1 \pm 1.0$

Figure 16. Trajectories across the Gotthard pass during north Foehn. The table gives the means of pressure level, potential temperature, relative humidity and specific humidity over all trajectories. Furthermore, the spread around this mean is given. The decrease in relative humidity (time  $t=32$  h) is related to the sinking of the air parcels south of the Alps.

of the Alps is increasingly affected by a developing lee cyclone.

#### 4.4 Cyclogenesis in the Lee of the Alps

At the south-western edge of the Alps, the flow separates from the orography (Figure 12). This separation is caused by the strong northerly winds which are channeled through the Rhone valley between the Pyrenees and the Alps (see section 4.2). At the region where separation takes place, a positive (cyclonic) PV anomaly develops (Figure 20). Since at that time Foehn winds cause extremely dry air at the western edge of the Alps, the PV anomaly is unlikely to be of diabatic origin. It must, to a large extent, be caused by the above mentioned flow separation. The detachment

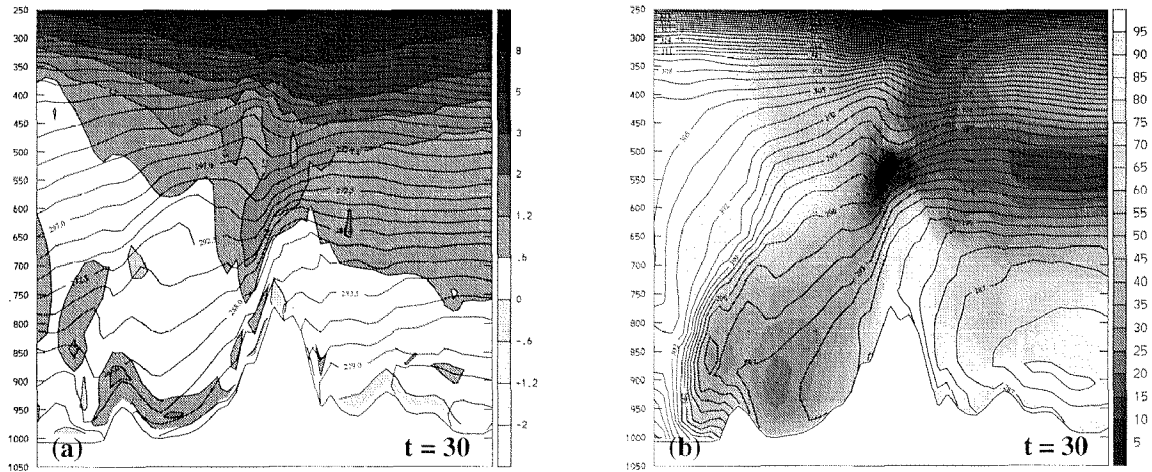


Figure 17. Vertical section for a south/north cross section over the Alps after 30 hours of simulation. (a) Potential vorticity in pvu (shaded) and potential temperature (lines). (b) Relative humidity (shaded) and equivalent potential temperature (lines).

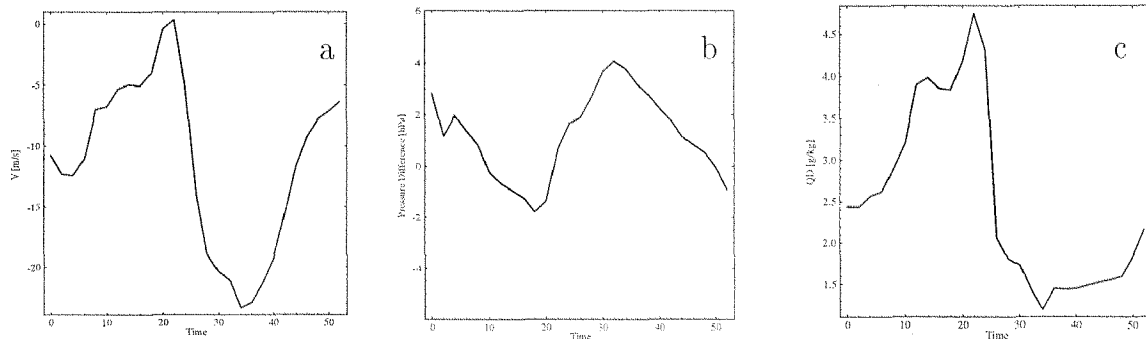


Figure 18. Temporal behavior of (a) northerly wind component at C in Figure 11 (south of the Gotthard pass) and at  $p=850$  hPa, C in Figure 11, (b) north/south surface pressure difference between D - C in Figure 11, and (c) specific humidity at the same position as in (a). The Gotthard jet is marked both with strong winds (see a) and with small specific humidity (see c).

itself may be caused by the frontal system movement or by the overlapping of an upper-level PV streamer at the 310 K isentropic surface (Figure 19). At  $t = 28$  h, the separated PV anomaly develops into a lee cyclone. At this time, the first closed contours appear in the 850 hPa geopotential (not shown), and then intensify during the ensuing hours into a strong lee cyclone.

As mentioned by Steinacker (1984), as well as by Bleck and Mattocks (1984), the advection of the upper-level PV anomaly supports the formation of a lee cyclone but may not be the only source of its origin. In fact, as stated earlier, a cold-air outbreak over the Mediterranean occurs. Such an outbreak was shown to be of some importance in a previous study (Aebischer and Schär 1998). The development of the low-level PV is strongly correlated with the development of the upper-level PV streamer, which carries stratospheric air over the Alps. Having reached the Alps, the upper-level PV streamer is affected by breaking gravity waves and vertically extending moisture processes and subsequently begins to wrap up above Sardinia (Figure 19).

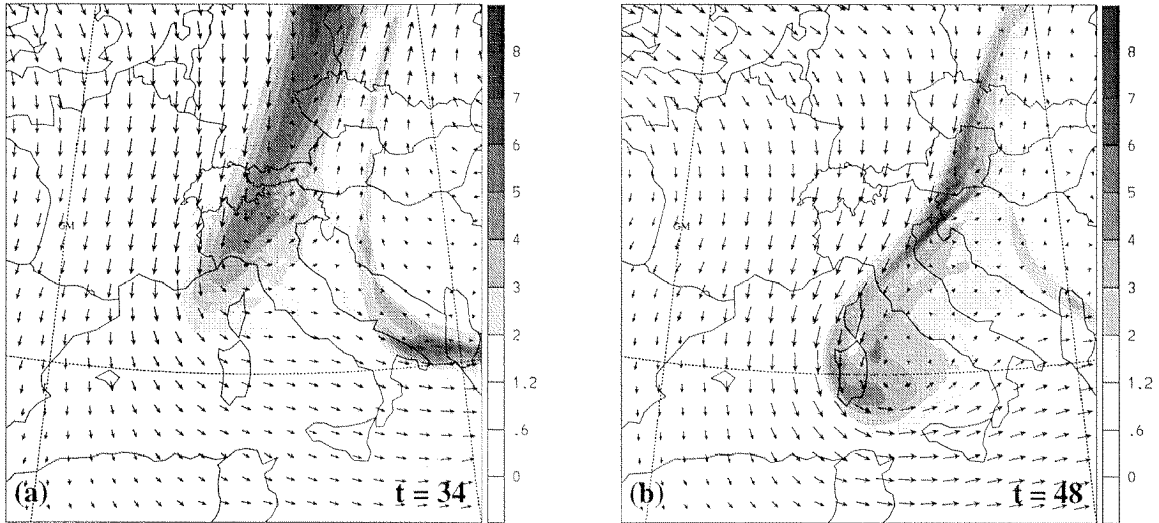


Figure 19. Potential vorticity in pvu and wind field on the 310 K isentropic surface after (a) 34 and (b) 48 hours of simulation, respectively. The passage of the upper-level PV streamer over the western Alps ( $t=34$  h) coincides with the detachment of a low-level PV anomaly. The furling of the upper-level PV streamer is associated with the development of the detached low-level PV anomaly into a lee cyclone.

The lee cyclone then reaches the 500hPa level. At the upper levels, a strong gradient in equivalent potential temperature separates the stratospheric dry air from tropospheric humid air (not shown). High values of PV and low equivalent potential temperature are typical for upper-level streamers (Fehlmann, 1997). Comparing the location of the cyclone center at 850 and 500 hPa respectively shows that the vertical tilt of the lee cyclone is smaller for the lee cyclone than for typical extratropical cyclones. Upper-level PV and low-level PV drift simultaneously towards south.

As soon as the low-level lee cyclone finally leaves the Alpine region and propagates south-eastwards towards Corsica and Sicily (Figure 20), moving steadily over the Mediterranean, relative humidity within the core of the cyclone rises, wind activity intensifies and, finally, heavy precipitation occurs (up to 100 mm/2 h) (not shown). As has already been stressed, the low-level PV at the western edge of the Alps was generated by *dry* processes, i.e. by flow separation. In fact, sensitivity experiments (see section 5.3) reveal that a complete suppression of moisture processes does not significantly modify the picture at the western Alpine edge. Nevertheless, after the formation of the PV banners at the western Alpine tip, moisture processes become important and diabatic processes generate PV, especially when the low-level PV anomaly drifts over the Mediterranean sea. This is consistent with a proposed two-step model for lee cyclogenesis, where an initial, mostly dry phase is followed by a baroclinic and diabatic phase.

#### 4.5 Anticyclone and Bora

After 30 hours of simulation, an anticyclonic flow arises at the eastern edge of the Alps. A clear anticyclone was analyzed by Steinacker (1984) in a hand analysis (Figure 23). Although this anticyclone was simulated too weakly in our simulation, the small horizontal pressure gradient in the south of the Alps is nevertheless a sign for anticyclonic flow, even more so when the anticyclone is overlapped by strong

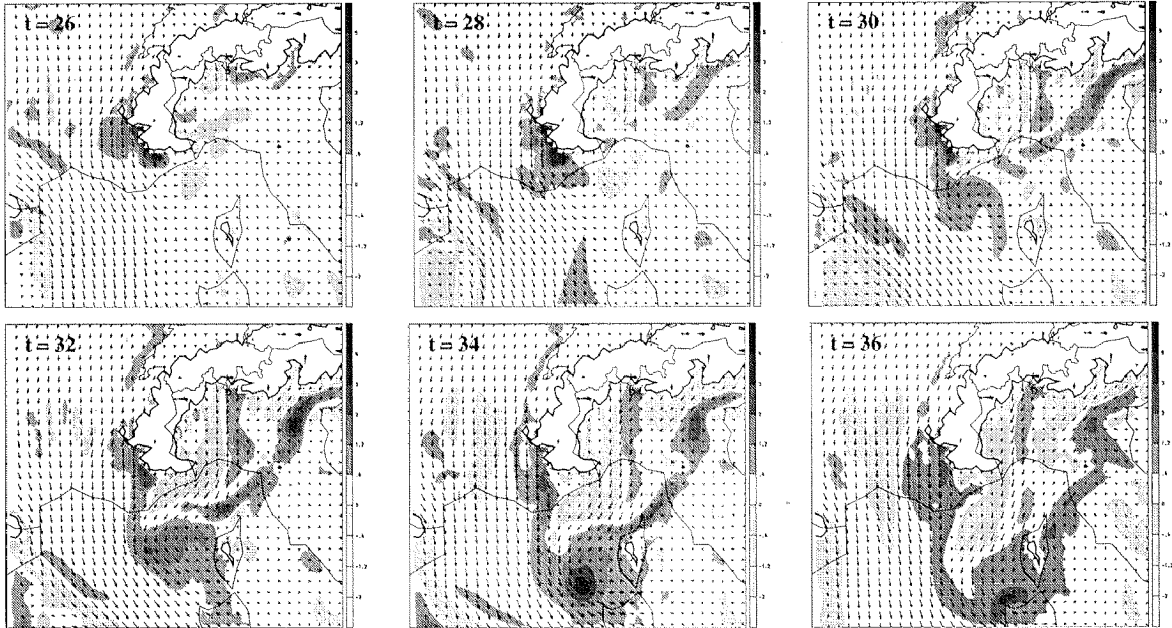


Figure 20. Potential vorticity in pvu and wind field at 850 hPa from  $t = 26$  h to  $t = 36$  h. Note the detachment of a PV anomaly at the western edge of the Alps. It finally matures into a lee cyclone. Furthermore, elongated positive and negative PV banners are discernible south of the Gotthard pass due to the north Foehn.

northerly flow. In spite of the strong northerly winds at upper levels, the low-level flow is “deflected” around the eastern edge of the Alps. In contrast to the situation at the western edge of the Alps, the associated negative PV anomaly does *not* separate from the orography, rather the low-level winds (below approximately 850 hPa) in the Po valley turn to easterly direction after 36 hours of simulation (Figure 22). At higher levels (300 to 400 hPa), behind the upper-level trough (Figure 19), northerly flow persists. At the start of the simulation, the very dry air in the Po valley does not show any motion. With the onset of the north Foehn, which can also be observed in the Inn valley and which is channeled through the Brenner pass, the air slowly begins to move. After 36 hours of simulation, there is a dry wind from north-east over the Po valley and into the Gulf of Genoa. The easterly winds might be driven primarily by the mature lee cyclone in the Gulf of Genoa (Figure 21).

## 5 Sensitivity Study

In this section, a range of sensitivity experiments are presented that are designed to identify the relative importance of the relevant dynamical processes. Three experiments were performed: (a) increasing the overall height of the orography, (b) increasing the roughness length, and (c) omission of all moisture processes. All these changes are expected to have a direct effect on the ability of the Alps to block and split the incident flow.

### 5.1 Effects of Orographic Height

In the following simulation, topography was increased by 20% and smoothed once using a standard filter. The increase led to maximum topographic height of 3300 m

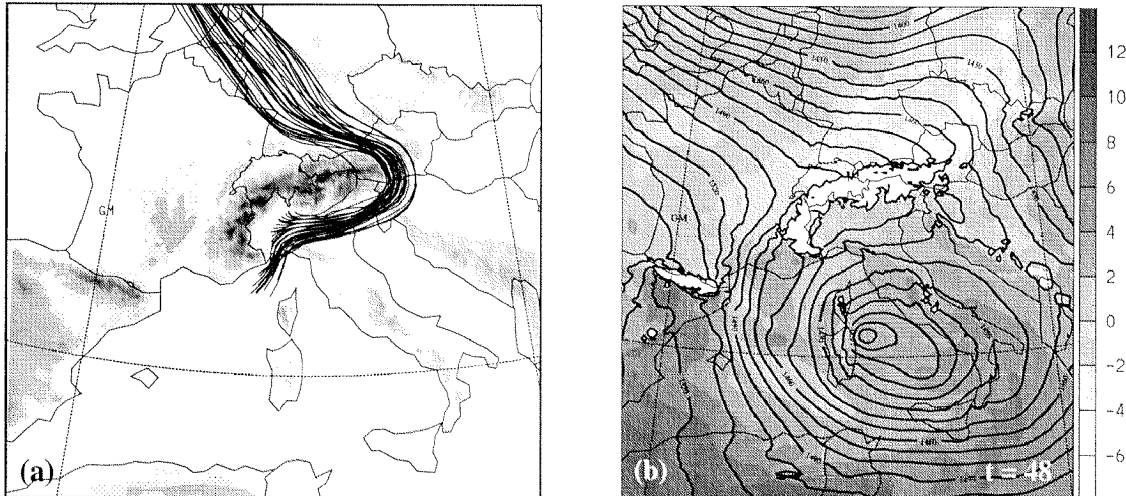


Figure 21. (a) Backward-in-time trajectories starting mostly in the Po valley between 860 and 840 hPa; (b) temperature (shaded) and geopotential (lines) at 850 hPa after 48 hours of simulation. The northerly winds are deflected leesides towards the west at the western edge of the Alps. This might be caused by an anticyclone at the eastern edge and by the already well-matured lee cyclone south of the Gulf of Genoa.

above sea level, instead of 3130 m for the standard case. According to Pierrehumbert and Wyman (1985), increasing the mountain height intensifies the upstream blocking of the low-level air. The boundary conditions were the same as for the standard experiment. The initial fields were obtained by an interpolation from the outer EM run. A separate EM run with correspondingly increased topography was not used, since the changes in the topography are not too large. For the nested HM run the same roughness length as in the standard case was used. Since the roughness length is partly determined by the subgrid-scale topography, this is not completely consistent. Nevertheless, due to the small relative change in the topographic height, the resulting flow fields can be taken as reasonable.

Surprisingly, the tendency for flow splitting does not increase and the cold front still crosses the Alps without being seriously disturbed. The lee cyclone and the anticyclone are not considerably intensified compared to the standard simulation. This is somewhat counter-intuitive since one would expect that the lee cyclone intensifies due to stronger blocking of air behind the higher Alps (Steinacker 1984).

## 5.2 Effects of Surface Friction

In another simulation, the roughness length for the whole integration domain was doubled. An increase in surface roughness length is motivated by the work of Georgelin et al. (1994), who found a significant increase in upstream blocking for a PYREX case.

In our simulation, the flow fields do not change to any great extent with respect to the reference simulation. Due to the increased surface friction, one might expect the near surface flow to slow down and the passage of the cold front across the Alpine crest to be rendered more difficult. As this is not the case, surface friction is not capable of significantly modifying the flow on such short time scales. Also the PV banners are only marginally affected.



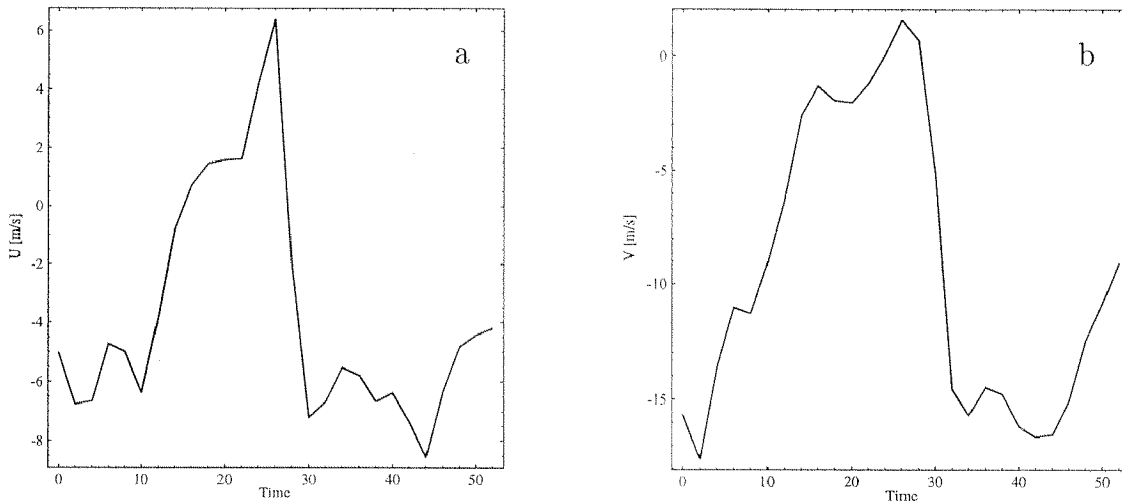


Figure 22. (a) Zonal wind component in the Po valley, point B in Figure 11 and (b) meridional wind component east of the Alps, point F in Figure 11. Both points at 850 hPa. Note the abrupt change in wind direction in the Po valley. At the eastern edge of the Alps the passage of the front is associated with the onset of strong northerly winds.

### 5.3 Effects of Diabatic Processes

Finally, the influence of diabatic processes were investigated. Latent heating can have two important effects on the standard simulation. It can favour a flow over a mountain instead of around it (see e.g. Schneidereit and Schär 1999), due to the additional buoyancy created when condensation occurs. On the other hand, latent heating can induce the formation of low-level PV anomalies and thereby contribute to and interact with frontogenesis and cyclogenesis.

In order to further examine the effects of latent heating, a dry numerical experiment was conducted. For this purpose moisture was completely removed from the initial and boundary data. The dry run is otherwise driven by the same EM run as the standard case.

As a result, the flow of cold air directed towards the Alps from the north is blocked more efficiently than in the standard run. This can be understood as being a consequence of the above mentioned buoyancy effect. The stronger blocking and more efficient horizontal deflection of the air leads to a stronger and faster cold-air outbreak between the Alps and the Pyrenees (not shown). Furthermore, the lack of moisture processes is also discernible in the cold front itself. Besides the stronger retardation of the front due to the blocking, the cold front now appears as a slimmer but stronger band of positive PV anomaly.

Lee cyclogenesis is also modified by the lack of latent heating. As already stressed in section 4.4, the positive PV anomaly at the western edge of the Alps is predominantly generated by (dry) flow separation. The minimal importance of latent heating in its formation might be inferred from a look at the precipitation map, which shows no rain at the western edge of the Alps, from the existence of dry north Foehn winds and, finally, from the dry simulation: The PV blob at the western edge of the Alps still occurs in the dry simulation, with approximately the same intensity. The positive PV values in the center of the *mature* cyclone remain somewhat weaker than before

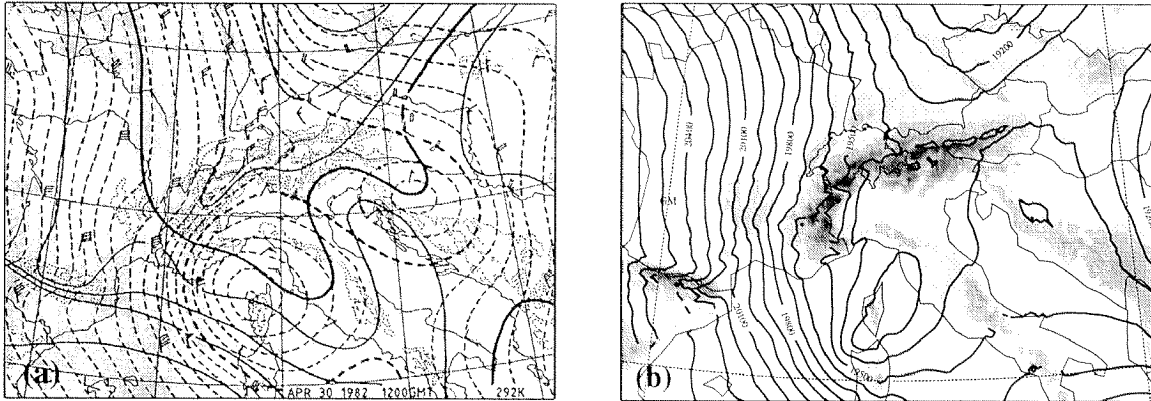


Figure 23. (a) Hand analysis after Steinacker (1984). Montgomery potential (dashed, every 10 gpm) and isobars (every 50 hPa) on the 292 K-isentropic surface over the Alpine Region at 12 UTC on 30 April 1982. (b) Corresponding Montgomery potential from simulation. A lee *anticyclone* is predicted by Steinacker at the eastern edge of the Alps. In contrast, no clear anticyclone occurs in the numerical simulation.

(-1 pvu) and are spread over a larger area. Essentially, the simulation confirms the findings by Aebischer (1996), who concluded that the development of a lee cyclone is intensified by moist processes, but also occurs in absence of humidity processes.

Finally, the negative PV anomaly at the eastern edge of the Alps and the associated anticyclone, is simulated similarly as in the standard case. In succession, however, the anomaly develops further and after 18 hours of simulation it separates from the topography. The anticyclone exists for another 12 hours until it disappears. Yet, the PV anomaly is not strong enough to ensure that anticyclonic closed isobars become evident in the pressure field at 850 hPa.

## 6 Conclusions and Outlook

Results from high-resolution numerical simulations of the modification of an approaching cold front by the Alps were analyzed. Special emphasis was placed upon the *temporal* development of the subsequent Alpine and Mediterranean weather. Furthermore, the dynamics of the lower troposphere was the focal point.

In a first part the ALPEX-IIIb reanalysis data set was compared with the ECMWF reanalysis data set, and it was shown that the former leads to more reliable simulations. The EM simulation with the former captured the intensity and vertical depth of the developing lee cyclone better than the corresponding run driven by the ECMWF reanalysis.

The second objective of this study was the detailed analysis of flow and weather phenomena that accompanied the frontal passage. Before the cold front reaches the Alpine crest, the northerly flow impinging on the Alps splits and moves sideways around the Alps, as was illustrated by trajectory calculations. As soon as the front approaches the crest, the tendency for flow splitting is considerably decreased, due to the strong northerly winds. The front itself passes the Alps whereupon the frontal gradient in equivalent potential temperature intensifies. The low-level parts of the front are retarded by the interaction with the Alps.

Three local wind systems are associated with the passage of the front: The Mistral along the Rhone valley between the Alps and the Pyrenees, the northerly Bora at the eastern edge of the Alps and North Foehn in the lee of the Alps and in the Po valley. The Mistral is associated with an extensive outbreak of cold air into the Mediterranean. The associated strong winds favour the separation of the northerly winds from the western edge of the Alps. A line of strong horizontal shear and an associated PV banner separates the Mistral winds from the calm air in the lee of the Alps. This calm vanishes only with the onset of the North Foehn. The strong winds, especially south of Alpine valley transects (such as the Gotthard and Brenner pass), reach far into the Po valley.

The PV anomaly associated with the western PV banner eventually separates from the Alps and drifts towards the south. When interacting with an upper-level PV streamer crossing the Alps, a lee cyclone develops. The first stage of the cyclogenesis is not strongly influenced by latent heating, but by essentially dry PV dynamics. As soon as the low-level PV moves over the Mediterranean sea, latent heating becomes more important and supports further PV generation. The strong northerly winds not only generate low-level PV at the western edge of the Alps, but also at the eastern edge. There, however, the PV anomalies do not detach from the orography. Nevertheless, the negative PV anomaly is associated with a pronounced anticyclonic flow around the eastern edge of the Alps. Also, the strong jet south of the Gotthard pass, which occurs during the North Foehn phase, is associated with elongated PV banners. They reach lengths up to 500km. Although a weaker jet is also discernible south of the Brenner pass, *no* clear PV banners emerged along it. This might be attributed to the weaker jet intensity and to special topographic features.



# PART E



## References

- Acheson, D. J., 1992: Elementary Fluid Dynamics. *Oxford Applied Mathematics and Computing Science Series*, **397pp**
- Aebischer, U., 1996: Low-level potential Vorticity and Cyclogenesis to the Lee of the Alps. *Diss. ETH Zürich No. 11732*, **127pp**
- Aebischer, U. and C. Schär, 1998: Low-level potential vorticity and cyclogenesis to the lee of the Alps. *J. Atmos. Sci.*, **55**, 186-207
- Armi, L. and R. Williams, 1993: The hydraulics of a stratified fluid flowing through a contraction. *J. Fluid Mech.*, **251**, 355-375
- Bacmeister, J. T., 1993: Mountain wave drag in the stratosphere and mesosphere inferred from observed winds and a simple parameterization scheme. *J. Atmos. Sci.*, **50**, 377-399
- Bacmeister, J. T. and R. T. Pierrehumbert, 1988: On high drag states of nonlinear, stratified flow over an obstacle. *J. Atmos. Sci.*, **45**, 63-80
- Bacmeister, J. T., P. A. Newman, B. L. Gary and K. R. Chan, 1994: An algorithm for forecasting mountain wave-related turbulence in the stratosphere. *Wea. Forecasting*, **9**, 241-253
- Baines, P. G., 1979: Observations of stratified flow past three-dimensional barriers. *J. Geophys. Res.*, **84**, 7834-7838
- Baines, P. G., 1987: Upstream blocking and airflow over mountains. *Ann. Rev. Fluid Mech.*, **19**, 75-97
- Batchelor, G. K., 1967: An Introduction to Fluid Dynamics. *Cambridge University Press*, **615pp**.
- Bauer, M., 1997: Three-dimensional numerical simulations of the influence of the horizontal aspect ratio on flow over and around a meso-scale mountain. *Diss. Leopold-Franzens-University Innsbruck*, **334pp**
- Binder, P., H. C. Davies and J. Horn, 1989: Free atmosphere kinematics above the northern Alpine foreland during ALPEX SOP. *Contr. Atmos. Phys.*, **62**, 30-45
- Binder, P. and A. Rossa, 1995: Verifikation der vertikalen Struktur des SM. *DWD-SMA Rundbrief*, **Nr. 10, III**, 13pp [available from Swiss Meteorological Institute, CH-8044 Zürich]
- Binder, P. and C. Schär, 1995: The Mesoscale Alpine Programme: Design Proposal. **63pp** [available from MAP Programme Office, c/o Swiss Meteorological Institute, CH-8044 Zuerich]
- Bleck, R., and C. Mattocks, 1984: A preliminary analysis of the role of potential vorticity in Alpine lee cyclogenesis. *Contrib. Atmos. Phys.*, **57**, 357-368
- Bougeault, P., 1983: A non-reflective upper boundary condition for limited-height hydrostatic models. *Mon. Wea. Rev.*, **111**, 420-429
- Bretherton, F. P., 1969: Momentum transport by gravity waves. *Quart. J. Roy. Met. Soc.*, **95**, 213-243
- Broccoli, A. J. and S. Manabe, 1992: The effects of orography on midlatitude northern hemispheric dry climates. *J. Climatol.*, **5**, 1181-1201
- Buzzi, A. and A. Tibaldi, 1978: Cyclogenesis in the lee of the Alps: A case study. *Quart. J. Roy. Met. Soc.*, **104**, 271-287
- Carslaw, K. S., M. Wirth, A. Tsias, B. P. Luo, A. Dörnbrack, M. Leutbecher, H. Volkert, W. Renger, J. T. Bacmeister, E. Reimer and Th. Peter, 1998: Increased stratospheric ozone depletion due to mountain-induced atmospheric waves. *NATURE*, Vol. 391, 675-678
- Chen, W.-D. and R. B. Smith, 1987: Blocking and deflection of airflow by the Alps. *Mon. Wea. Rev.*, **115**, 2578-2597

- Clark, T. L. and W. R. Peltier, 1984: Critical level reflection and the resonant growth of nonlinear mountain waves. *J. Atmos. Sci.*, **41**, 3122-3134
- Clark, T. L., W. D. Hall and R. M. Banta, 1994: Two- and three-dimensional simulations of the 9 January 1989 severe Boulder windstorm: comparison with observations. *J. Atmos. Sci.*, **51**, 2317-2343
- Courvoisier, H. W. and T. Gutermann, 1971: Zur praktischen Anwendung des Föhnstests von Widmer. *Arbeitsber. d. Schweiz. Met. Zentralanst. Zürich*, No. **21**, 7 pp
- Davies, H. C., 1976: A lateral boundary formulation for multi-level prediction models. *Quart. J. Roy. Meteor. Soc.*, **102**, 405-418
- Davies, H. C., 1984: On the orographic retardation of a cold front. *Contrib. Atmos. Phys.*, **57**, 409-418
- Davies, H. C., 1986: Observational studies and interpretation of the mountain pressure drag during ALPEX. *Proc. ECMWF seminar, Reading 1986*, **113-136**
- Davies, H. C. and J. Horn, 1988: Semi-geostrophic flow of a stratified atmosphere over elongated isentropic valleys and ridges. *Tellus.*, **40A**, 61-79.
- Davies, H. C. and P. D. Phillips, 1985: Mountain Drag along the Gotthard Section during ALPEX. *J. Atmos. Sci.*, **42**, 2093-2109
- Durran, D. R., 1986: Another look at downslope windstorms. Part I: The development of analogs to supercritical flow in an infinitely deep, continuously stratified flow. *J. Atmos. Sci.*, **43**, 2527-2543
- Durran, D. R., 1990: Mountain waves and downslope winds. In: Blumen, W.(ed.), Atmospheric Processes over Complex Terrain. *Meteor. Monogr.*, No. **45**, Amer. Meteor. Soc., 59-81
- Egger, J. and K. P. Hoinka, 1992: Fronts and orography. *Meteorol. Atmos. Phys.*, **48**, 3-36
- Eliassen, A. and E. Palm, 1961: On the transfer of energy in stationary mountain waves. *Geof. Publ.*, **22**, (3), 1-23
- Fehlmann, R. and H. C. Davies, 1997: Misforecasts of Synoptic Systems: Diagnosis via PV-Retrodiction. *Mon. Wea. Rev.*, **125**, 2247-2264
- Fehlmann, R., C. Quadri and H. C. Davies, 1999: An Alpine rainstorm: sensitivity to the mesoscale upper-level structure. *Wea. Forecasting*, [submitted]
- Frei, C. and C. Schär, 1998: A precipitation climatology of the Alps from high-resolution rain-gauge observations. *Int. J. Climatol.*, **18**, 873-900
- Frei, C., C. Schär, D. Lüthi and H. C. Davies, 1998: Heavy precipitation processes in a warmer climate. *Geophys. Res. Letters*, **25**, 1431-1434
- Georgelin, M., E. Richard, M. Petitdidier and A. Druilhet, 1994: Impact of subgrid-scale orography parameterization on the simulation of orographic flows. *Mon. Wea. Rev.*, **122**, 1509-1522
- Georgelin, M. and E. Richard, 1994: Numerical simulation of flow diversion around the Pyrenees: A Tramontana Case Study. *Mon. Wea. Rev.*, **124**, 687-700
- Gerhard, P., 1994: ALPEX level-IIIB Analyses Produced at the DWD. *MAP Newsletter* **1**, November 1994, [available from Schweizerische Meteorologische Anstalt, Krähbühlstrasse 58, CH-8044 Zrich, Switzerland]
- Gill, A. E., 1982: Atmosphere-ocean dynamics. *Int. geophysics series, Academic Press, London*, **662pp**
- Gueller, A., 1979: Der aussergewöhnliche Föhnsturm vom 13. Februar 1976 in der Ostschweiz. *Arbeitsber. d. Schweiz. Met. Zentralanst. Zürich*, No. **69**, 16 pp
- Hannemann, K. and H. Oertel, 1989: Numerical simulation of the absolutely and convectively unstable wake. *J. Fluid Mech.*, **199**, 55-88



- Heimann, D. and H. Volkert, 1988: The "papal-front" of 3 May 1987 – mesoscale analyses of routine data. *Beitr. Phys. Atmos.*, **61**, 62-68
- Herzog, H. J., 1995: Testing a radiative upper boundary condition in a nonlinear model with hybrid vertical coordinate. *Meteor. Atmos. Phys.*, **55**, 185-204
- Hoinka, K. P., 1985: Observation of the airflow over the Alps during a Foehn event. *Quart. J. Roy. Met. Soc.*, **111**, 199-224
- Hoinka, K. P., 1990: Untersuchungen der alpinen Gebirgsüberströmung bei Südföhn. *Forschungsbericht, DLR, Institut für Physik der Atmosphäre*. **186pp**. [available from Wissenschaftliches Berichtswesen der DLR, Postfach 90 60 58, 5000 Köln 90.]
- Hoinka, K. P. and T. Clark, 1991: Pressure drag and momentum fluxes forced by the Alps. Part I: Comparison between numerical simulations and observations. *Quart. J. Roy. Met. Soc.*, **117**, 495-525
- Hoinka, K. P., M. Hagen, H. Volkert and D. Heimann, 1990: On the influence of the Alps on a cold front. *Tellus*, **42A**, 140-164
- Holton, J. R., 1992: An introduction to dynamic meteorology. 3d edition. *Int. geophysics series, Academic Press, London*, **511pp**
- Hoskins, B. J., M. E. McIntyre and A. W. Robertson, 1985: On the use and significance of isentropic potential vorticity maps. *Quart. J. Roy. Met. Soc.*, **111**, 877-946
- Houghton, D. D. and A. Kasahara, 1968: Nonlinear shallow fluid flow over an isolated ridge. *Comm. Pure Appl. Math.*, **21**, 1-23
- Hunt, J. C. R. and W. H. Snyder, 1980: Experiments on stably and neutrally stratified flow over a model three-dimensional hill. *J. Fluid Mech.*, **96**, 671-704
- IPCC (Intergovernmental Panel for Climate Change), 1990: Climate Change: The IPCC Scientific Assessment. *Cambridge University Press*
- Jackson, P. L. and D. G. Steyn, 1994a: Gap winds in a Fjord. Part I: Observations and Numerical Simulation. *Mon. Wea. Rev.*, **122**, 2645-2665
- Jackson, P. L. and D. G. Steyn, 1994b: Gap winds in a Fjord. Part II: Hydraulic Analog. *Mon. Wea. Rev.*, **122**, 2666-2676
- Kalthoff, N. and B. Vogel, 1992: Counter-Current and Channeling Effect Under Stable Stratification in the Area of Karlsruhe. *Theor. Appl. Climatol.*, **45**, 113-126
- Klemp, J. B. and D. K. Lilly, 1975: The dynamics of wave-induced downslope winds. *J. Atmos. Sci.*, **32**, 320-339
- Klemp, J. B. and D. K. Lilly, 1978: Numerical simulation of hydrostatic mountain waves. *J. Atmos. Sci.*, **35**, 78-107
- Klemp, J. B. and D. R. Durran, 1983: An upper boundary condition permitting internal gravity wave radiation in numerical mesoscale models. *Mon. Wea. Rev.*, **111**, 430-444
- Kljun, N., 1996: Starkföhnereignis November 1996. *Semesterarbeit am Institut für Atmosphärenphysik der ETH Zürich*, **41pp**
- Kljun, N., M. Sprenger and C. Schär, 1999: The modification of a front by the Alps: a case study using the ALPEX reanalysis data set. [to be submitted], *ETH Zürich*
- Kuettner, J., 1980: ALPEX 1980: The Alpine Experiment (ALPEX) Design Proposal. *Edited by J. Kuettner, WMO, Geneva*, **184pp**
- Kuhn, M., 1989: Föhnstudien. *Hrsg. von M. Kuhn. Darmstadt: Wiss. Buchges.* **504pp**
- Long, R. R., 1953: Some aspects of the flow of stratified fluids. I. A theoretical investigation. *Tellus*, **5**, 42-58

- Long, R. R., 1955: Some aspects of the flow of stratified fluids: III. Continuous density gradients. *Tellus*, **7**, 341-357
- Lönnberg, P. and D. Shaw, 1987: ECMWF Data Assimilation – Scientific Documentation. *ECMWF Research Manual 1, 10/87, 2nd Revised Edition*.
- Louis, J.-F., 1979: A parametric model of vertical eddy fluxes in the atmosphere. *Boundary-Layer Meteor.*, **17**, 187-202
- Lüthi, D., 1994: Mesoskalige diabatische und orographische Anregung atmosphärischer Strömungen: Theoretische Untersuchungen und numerische Simulationen. *Diss. ETH Zürich No. 10322*
- Lüthi, D., C. Schär and H. C. Davies, 1989: On the Atmospheric Response to Steady Mesoscale Low-Level Diabatic Heating. *Beitr. Phys. Atmosph.*, **Vol. 62, No. 2** 126-150
- Lüthi, D., A. Cress, H. C. Davies and C. Schär, 1996: Interannual Variability and Regional Climate Simulations. *Theor. Appl. Climatol.*, **53**, 185-209
- Majewski, D., 1991: The Europa-Modell of the Deutscher Wetterdienst. *ECMWF Seminar on numerical methods in atmospheric models*, **Vol. 2**, 147-191
- Majewski, D. and R. Schrodin, 1999: Short description of the Europa-Modell (EM) and Deutschland-Modell (DM) of the Deutscher Wetterdienst (DWD). Quarterly Bulletin. [Available from: Deutscher Wetterdienst, Zentralamt, 63004 Offenbach am Main]
- Mayr, G. J and T. B. McKee, 1995: Observations of the Evolution of Orographic Blocking. *Mon. Wea. Rev.*, **123**, 1447-1464
- Mellor, G. L. and T. Yamada, 1974: A hierarchy of turbulence closure models for planetary boundary layers. *J. Atmos. Sci.*, **31**, 1791-1806
- Miller, P. P. and D. R. Durran, 1991: On the sensitivity of downslope windstorms to the asymmetry of the mountain profile. *J. Atmos. Sci.*, **48**, 1457-1473
- Morgenstern, O., 1998: Alpine-Southside Precipitation Events: Model Studies and Physical Concepts. *Diss. ETH Zürich Nr. 12421*, **131pp**
- Müller, E., 1981: Turbulent flux parameterization in a regional-scale model. *Proc. ECMWF Workshop on planetary boundary layer parameterization*, 193-220
- Olafsson, H. and P. Bougeault, 1996: Nonlinear flow past an elliptic mountain ridge. *J. Atmos. Sci.*, **53**, 2465-2489
- Olafsson, H. and P. Bougeault, 1997: The effect of rotation and surface friction on orographic drag. *J. Atmos. Sci.*, **54**, 193-210
- Palmer, T. N., G. J. Shutts and R. Swinbank, 1986: Alleviation of a westerly bias in general circulation models through an orographic gravity wave drag parameterization. *Quart. J. Roy. Met. Soc.*, **112**, 1001-1039
- Pan, F. and R. B. Smith, 1998: Gap Winds and Wakes: SAR observations and numerical simulations. *J. Atmos. Sci.*, **56**, 905-923
- Pedlosky, J., 1987: Geophysical fluid dynamics. *Springer Verlag, New York*, **710pp**
- Peltier, W. R. and T. L. Clark, 1979: The evolution and stability of finite-amplitude mountain waves. Part II: Surface wave drag and severe downslope windstorms. *J. Atmos. Sci.*, **36**, 1498-1529
- Peltier, W. R. and T. L. Clark, 1983: Nonlinear mountain waves in two and three spatial dimensions. *Quart. J. Roy. Met. Soc.*, **109**, 527-548
- Peng, M. S., S.-W. Li, S. W. Chang and R. T. Williams, 1995: Flow over mountains: Coriolis force, transient troughs and three-dimensionality. *Quart. J. Roy. Met. Soc.*, **121**, 593-613
- Pettré, P., 1982: On the problem of violent winds. *J. Atmos. Sci.*, **39**, 542-554
- Pichler, H., 1997: Dynamik der Atmosphäre. *Spektrum Akademischer Verlag, 3. aktualisierte Auflage, Heidelberg · Berlin · Oxford*, **572pp**

- Pierrehumbert, R. T., 1984: Linear results on the barrier effects of mesoscale mountains. *J. Atmos. Sci.*, **41**, 1356-1367
- Pierrehumbert, R. T. and B. Wyman, 1985: Upstream effects of mesoscale mountains. *J. Atmos. Sci.*, **42**, 977-1003
- Ritter, B. and J. F. Geleyn, 1992: A comprehensive radiation scheme for numerical weather prediction with potential application in climate simulations. *Mon. Wea. Rev.*, **120**, 303-325
- Saito, K., 1993: A numerical study of the local downslope wind "Yama-ji-kaze" in Japan. Part 2: Non-linear aspect of the 3-D-flow over a mountain range with a col. *J. Meteor. Soc. Japan*, **71**, 247-271
- Saito, K., 1994: A numerical study of the local downslope wind "Yama-ji-kaze" in Japan. Part 3: Numerical simulation of the 27 September 1991 windstorm with a non-hydrostatic multi-nested model. *J. Meteor. Soc. Japan*, **72**, 301-329
- Schär, C., 1990: Quasi-geostrophic lee cyclogenesis. *J. Atmos. Sci.*, **47**, 3044-3066
- Schär, C., 1993: A Generalization of Bernoulli's Theorem. *J. Atmos. Sci.*, **49**, 1437-1443
- Schär, C., 1995: Gebirgsumströmungen und Gebirgsüberströmungen. *DWD-SMA Rundbrief*, Nr. **10**, **III**, 15pp. [available from Swiss Meteorological Institute, CH-8044 Zürich]
- Schär, C. and H. C. Davies, 1988: Quasi-geostrophic stratified flow over isolated finite amplitude topography. *Dynamics of Atmospheres and Oceans*, **11**, 287-306
- Schär, C. and R. B. Smith, 1993a: Shallow-water flow past isolated topography. Part I: Vorticity production and wake formation. *J. Atmos. Sci.*, **50**, 1373-1400
- Schär, C. and R. B. Smith, 1993b: Shallow-water flow past isolated topography. Part II: Transition to vortex shedding. *J. Atmos. Sci.*, **50**, 1401-1412
- Schär, C. and D. R. Durran, 1997: Vortex Formation and Vortex Shedding in Continuously Stratified Flows past Isolated Topography. *J. Atmos. Sci.*, **54**, 534-554
- Schär, C., T. D. Davies, C. Frei, H. Wanner, M. Widmann, M. Wild and H. C. Davies, 1998: Current Alpine Climate, in: Views from the Alps. Regional Perspectives on Climate Change. *Massachusetts Institute of Technology*, **514pp**
- Schneiderei, M. and C. Schär, 1999: Idealised numerical experiments of Alpine flow regimes and southside precipitation events. *Meteorol. Atmos. Phys.*, [submitted]
- Schrodin, R., 1995: Dokumentation des EM/DM-Systems. *Deutscher Wetterdienst, Zentralanstalt, Abteilung Forschung, Postfach 10 04 65. 63004 Offenbach a. Main.*
- Schweitzer, H., 1953: Versuch einer Erklärung des Föhns als Luftströmung mit überkritischer Geschwindigkeit. *Archiv für Meteorologie, Geophysik und Bioklimatologie Ser. A 5*, S. 350-371
- Scorer, R. S., 1952: Mountain-gap winds: a study of surface wind at Gibraltar. *Quart. J. Roy. Meteor. Soc.*, **78**, 53-61
- Seibert, P., 1985: Fallstudien und statistische Untersuchungen zum Südföhn im Raum Tirol. *Diss. Universität Innsbruck*, **369pp.**
- Sheppard, P. A., 1956: Airflow over mountains. *Quart. J. Roy. Met. Soc.*, **82**, 528-529
- SMA 1976: Wetterbericht der Schweizerischen Meteorologischen Zentralanstalt Zürich
- Smith, R. B., 1977: The steepening of hydrostatic mountain waves. *J. Atmos. Sci.*, **34**, 1634-1654
- Smith, R. B., 1979a: The influence of the earth's rotation on mountain wave drag. *J. Atmos. Sci.*, **36**, 177-180
- Smith, R. B., 1979b: The influence of mountains on the atmosphere. *Adv. Geophys.*, **21**, 87-230
- Smith, R. B., 1980: Linear theory of stratified hydrostatic flow past an isolated mountain. *Tellus*, **32**, 348-364

- Smith, R. B., 1982: Synoptic observations and theory of orographically disturbed wind and pressure. *J. Atmos. Sci.*, **39**, 60-70
- Smith, R. B., 1985a: On severe downslope winds. *J. Atmos. Sci.*, **42**, 2597-2603
- Smith, R. B., 1985b: Mesoscale mountain meteorology in the Alps. *Proceedings of the conference on the scientific results of the Alpine Experiment (ALPEX)*. World Meteorological Organization, **2**, 407-423
- Smith, R. B., 1987: Aerial observations of the Yugoslavian Bora. *J. Atmos. Sci.*, **44**, 269-297
- Smith, R. B., 1988: Linear theory of stratified flow past an isolated mountain in isosteric coordinates. *J. Atmos. Sci.*, **45**, 3889-3896
- Smith, R. B., 1989a: Hydrostatic airflow over mountains. *Adv. Geophys.*, **31**, 1-42
- Smith, R. B., 1989b: Comment on "Low Froude number flow past three-dimensional obstacles. Part I: Baroclinically generated lee vortices". *J. Atmos. Sci.*, **46**, 3611-3613
- Smith, R. B. and J. Sun, 1987: Generalized hydraulic solutions pertaining to severe downslope winds. *J. Atmos. Sci.*, **44**, 2934-2939
- Smith, R. B. and S. Gronas, 1993 Stagnation points and bifurcation in 3-D mountain airflow. *Tellus*, **45A**, 28-43
- Smith, R. B. and V. Grubisic, 1993: Aerial observation of Hawaii's wake. *J. Atmos. Sci.*, **50**, 3728-3750
- Smolarkiewicz, P. K. and R. Rotunno, 1989a: Low Froude number flow past three dimensional obstacles. Part I: Baroclinically generated lee vortices. *J. Atmos. Sci.*, **46**, 1154-1164
- Smolarkiewicz, P. K. and R. Rotunno, 1989b: Reply. *J. Atmos. Sci.*, **46**, 3614-3617
- Sprenger, M., and C. Schär, 1999: Rotational aspects of stratified gap flows and shallow foehn. *J. Atmos. Sci.*, [submitted]
- Sprenger, M., R. Fehlmann, H. C. Davies and C. Schär, 1999: Linearized flow over isolated orography: the influence of rotation. [to be submitted]
- Steinacker, R., 1984a: Airmass and frontal movement around the Alps. *Riv. Met. Aer.*, **43**, 85-93
- Steinacker, R., 1984b: The isentropic vorticity and the flow over and around the Alps. *Riv. Met. Aer.*, **43**, 79-83
- Sun, W.-Y. and J.-D. Chern, 1994: Numerical experiments of vortices in the wakes of large idealized mountains. *J. Atmos. Sci.*, **51**, 191-209
- Tafferner, A., 1990: Lee cyclogenesis resulting from the combined outbreak of cold air and potential vorticity against the Alps. *Meteorol. Atmos. Phys.*, **43**, 31-48
- Tiedtke, M., 1989: A comprehensive mass flux scheme for cumulus parameterization in large-scale models. *Mon. Wea. Rev.*, **117**, 1779-1800
- Trüb, J., 1993: Dynamical aspects of flow over Alpine-scale topography: A modeling perspective. *Diss. ETH Zürich No. 10339*, **140pp**
- Trüb, J. and H. C. Davies, 1994: Flow over a mesoscale ridge: Pathways to regime transition. *Tellus*, **47A**, 502-524
- Wernli, H., 1995: Lagrangian perspective of extratropical cyclogenesis. *Diss. ETH Zürich Nr. 11016*, **157pp.**
- Wernli, H. and H. C. Davies, 1996: A Lagrangian-based analysis of extratropical cyclones. Part I: The method and some applications. *Quart. J. Roy. Met. Soc.*, **122**, 467-489
- Widmer, R., 1966: Statistische Untersuchungen über den Föhn im Reusstal und Versuch einer objektiven Föhnprognose für die Station Altdorf. *Diss. UNI. Zürich.*, Vierteljahresschrift SNG Zürich 1966

- Wippermann, F., 1984: Air flow over and in broad valleys: channelling and counter-current. *Contr. Atmos. Phys.*, **57**, 92-105
- Zängl, G., 1999: Three-dimensional idealized simulations of the Foehn in the region of Innsbruck. *Contr. Atmos. Phys.*, [in press]



## Curriculum Vitae

Michael Sprenger

born on 16 April 1970 in Chur (GR), Switzerland  
citizen of Triesen, Principality of Liechtenstein

### EDUCATION AND PROFESSIONAL TRAINING

1982 – 90 Liechtensteinisches Gymnasium, Vaduz

*Matura Type B*

1990 – 96 University study in Physics at the Swiss Federal Institute of Technology (ETH) Zürich. Specialization in the fields *Theoretical Astrophysics* and *Atmospheric Science*. Diploma thesis “*Idealisierte Gebirgsüberströmungen: Untersuchungen über den Gültigkeitsbereich eines linearen Modells unter besonderer Berücksichtigung der Erdrotation* ” under the guidance of Prof. H. C. Davies

*Dipl. Phys. ETH*

1996 – 99 Ph.D. student at the Institute for Atmospheric Science and GI-ETH, ETH Zürich, in the group of Prof. Ch. Schär

1997 – 99 Postgraduate Course in Applied Statistics

*Dipl. NDK Angewandte Statistik ETH*

### INTERNATIONAL CONFERENCES AND WORKSHOPS

MAP Meeting Hall, Austria (1996). MAP Meeting Belgirate, Italy (1997). SANW Meeting Airolo, Switzerland (1998). MAP Meeting Appenzell, Switzerland (1999).

### SPECIAL TRAINING COURSE

Summer School in Geophysical and Environmental Fluid Dynamics, University of Cambridge 1997. Visiting scientist at Environmental Canada, Atmospheric modelling group, Montreal, Canada 1998.

### CURRENT ADDRESS

Michael Sprenger

Viktoriastrasse 14

8057 Zürich, Switzerland

e-mail: sprenger@geo.umnw.ethz.ch





## Acknowledgments / Dank

Drei Jahre Arbeit! Eine lange Zeit, während der ich viele Doktoranden, Professoren, Postdocs, Studenten, Mitarbeiter kennenlernen konnte. Es ist die fruchtbare Zusammenarbeit mit all diesen Leuten, die letztendlich zum Gelingen meiner Dissertation beigetragen hat.

Mein herzlichster Dank gehört Prof. Dr. Christoph Schär, der mich in seine Gruppe als Doktorand aufgenommen hat. Seine fachliche Unterstützung, aber auch die angenehme Arbeitsatmosphäre, die er in seiner Gruppe zu vermitteln vermochte, haben mir sehr geholfen, diese Arbeit zu durchzuführen.

Prof. Dr. Huw Davies was my first teacher in atmospheric dynamics! His motivating lectures, but also the interesting subject for my diploma thesis, which he supervised, encouraged me to “dare” a Ph. D. thesis. His talent for speeches will, certainly, always be unreachable to me!

Dr. Georg Mayr hat sich sofort bereit erklärt, als Korreferent einzutreten. Für sein Interesse an meiner Arbeit bin ich sehr dankbar.

Ein lineares Modell, eine idealisierte Version des EM und schliesslich ein “volles” EM/HM habe ich für diese Arbeit verwendet. Dass dies überhaupt möglich war, verdanke ich vor allem Daniel Lüthi. Seine Hilfsbereitschaft und auch die Schnelligkeit, mit der er jegliche Computerprobleme behoben hat, haben wesentlich zum Gelingen meiner Arbeit beigetragen.

Dem Deutschen Wetterdienst (DWD) und der Schweizerischen Meteorologischen Anstalt (SMA) danke ich für die Möglichkeit, mit dem EM/HM zu arbeiten, und für die Bereitstellung des ALPEX-IIIb Datensatzes.

Während meiner Diplomarbeit, die ich unter der Aufsicht von Prof. Dr. Huw Davies durchführte, hat mich René Fehlmann betreut. Seine anregende Betreuung hat mit dazu beigetragen, dass wir diese Arbeit in die Form eines Papers bringen konnten.

Ich selbst durfte während der drei Jahre, die ich am LAPETH verbrachte, mehrere Diplom- und Semesterarbeiten betreuen: Esther Häller, Stephan Schwere, Fortunat Kind, Natascha Kljun. Für Euren Einsatz und Euer Interesse Danke! Besonders an Natascha, deren Diplomarbeit zu dieser Diss beigetragen hat.

Heini Wernli, David Bresch, Conny Schwierz, Jürg Schmidli, André Walser. Eine lange Liste von Personen, mit denen ich gemeinsam in einem Büro arbeiten durfte, und die für eine “gute Atmosphäre” sorgten. Es gibt viele andere Doktoranden, Postdocs und Mitarbeiter, die ich an dieser Stelle erwähnen müsste. Pamela Heck, Michael Schneiderei, Sophie Fukutome, Olaf Morgenstern, Christoph Frei, Ruedi Lüthi... Danke Euch allen und auch all denen, die hier nicht namentlich erwähnt sind.

Nicht zu letzt gebührt natürlich auch meinen Eltern Ferdinand und Margot, sowie meinen Geschwistern Bettina und Marion Dank. Ihre Unterstützung und Liebe haben mich während all der Studien- und Diss-Jahre begleitet.

Eine Dissertation zu schreiben ist eine grosse Leistung, zu erkennen, dass es aber letztendlich doch nur eine Diss ist, eine noch viel grössere! All den Freunden und Kollegen, die mir das bewusst gemacht haben, möchte ich ebenfalls danken. Ganz besonders Fredy für all die gemeinsamen Jahre in Zürich, und Sabine, deren “Wärme” und Unterstützung mich während der Endphase meiner Arbeit begleitet haben. Wäre

das Leben ein Brunnen, so wäre die Diss ein Tropfen im Trog. So richtig aus dem Tiefen zu schöpfen, dazu habt ihr mir verholfen!